ELECTROSPUN NANOFIBER MESHES FOR THE FUNCTIONAL REPAIR OF BONE DEFECTS

A Dissertation
Presented to
The Academic Faculty

by

Yash M. Kolambkar

In Partial Fulfillment
of the Requirements for the Degree
Doctor of Philosophy in the
Wallace H. Coulter Department of Biomedical Engineering

Georgia Institute of Technology
December 2009

ELECTROSPUN NANOFIBER MESHES FOR THE FUNCTIONAL REPAIR OF BONE DEFECTS

Approved by:

Dr. Robert E. Guldberg, Advisor
School of Mechanical Engineering
Georgia Institute of Technology

Dr. Dietmar W. Hutmacher
Institute of Health and Biomedical Innovation
Queensland University of Technology

Dr. Ravi V. Bellamkonda
Department of Biomedical Engineering
Georgia Institute of Technology

Dr. Johnna S. Temenoff
Department of Biomedical Engineering
Georgia Institute of Technology

Dr. Andrés J. García
School of Mechanical Engineering
Georgia Institute of Technology

Date Approved: October 23, 2009

To Ayona, for being there with me every step of the way

ACKNOWLEDGEMENTS

I have to admit that when I joined the Bioengineering Ph.D. program at Georgia Tech in 2004, I had no idea of what I was getting into, at least not a good one. My background in Mechanical Engineering, that too computational solid mechanics, did not prepare me much for the mostly experimental bioscience research that I was to perform. The last time I had seen a cell or a microscope was……..I don't even remember. So needless to say, the initial years of my Ph.D. were challenging. However, .along the way, many people trained, guided and supported me, and I have them to thank for helping me reach this milestone today.

First and foremost, I would like to thank my advisor, Dr. Robert E. Guldberg. Bob took a chance in taking a pure mechanical engineer into the lab, and I will always be grateful to him for that. It took me a while to get used to Bob's hands-off style of managing, but eventually I came to appreciate that his reason for doing so was to enable the personal development of the student. Despite his busy schedule, Bob always made himself available to talk about research, and his sharp analytical and critical reasoning skills contributed immensely to the success of my thesis. I am thankful for his ability to stay calm and composed and objectively look at data. On numerous occasions, it aided me to trouble shoot after a not-so-successful experiment. In addition, I thank Bob for allowing me to pursue my research interests, as well as extracurricular activities like the TI:GER program and BBUGS.

I am also grateful to my thesis committee members for their guidance and support in the completion of my Ph.D. thesis. Dr. Hutmacher started the collaboration with

nanofiber meshes, and has been very closely involved in my project. He hosted me at the National University of Singapore, where I was exposed to the various nanofiber mesh protocols developed in his lab. I would like to thank Dr. Garcia for his guidance in the *in vitro* studies and his constructive criticism, which has helped me maintain high standards in my research. I was always amazed by the insightful questions that Dr. Bellamkonda came up with, and I thank him for opening up new avenues of thinking for me. Finally, I would like to thank Dr. Temenoff for her support and valuable feedback.

This thesis would not have been possible without the former and current members of the Guldberg lab. I am especially indebted to Ken Dupont and Joel Boerckel for their assistance with the *in vivo* studies. Ken and I joined around the same time, and his exemplary work ethic and selfless attitude serves as a model to everybody in our lab. Ken was instrumental in developing the technique for nanofiber mesh implantation, and I especially thank him for the brilliant idea of the L-shim. Joel's enthusiasm for research is admirable, and I tremendously enjoyed our intellectually stimulating discussions about bone regeneration. I would like to acknowledge Mehmet Bajin, an Undergraduate Research Scholar, who worked with me for almost a year and a half. He worked diligently and put up with my OCD with protocols, and at the same time maintained a lighthearted approach that made mentoring him very enjoyable. Mehmet has a gift of keeping a straight face while pulling a prank on me – "Yash, I dropped the gas tank!", and till the end I could not figure out if he was serious or joking. I thank Mela Johnson, who was my office mate for most of my time at GT, for her warm and kindhearted demeanor and her advice on protein delivery techniques. Angela Lin and Hazel Stevens are great assets to the Guldberg lab, and are instrumental in keeping the lab running.

They assisted me with μCT imaging, mechanical testing and microscopy, techniques that were central to my thesis. I thank Chris Dosier, Dr. Liqin Xie, Dr. Tamim Diab, Brent Uhrig, Eric Deutsch, Jessical O'Neal and Jason Wang for their support over the years and help in reviewing my thesis. I have to mention the robust electrospinning setup that Brent has built, which makes the one I put together look so ghetto. A special thanks to former lab members, Dr. Chris Gemmiti and Dr. Alex Peister, for training me in cell culture techniques, which became a significant part of my thesis. I know I must have tested their patience on more than one occasion, but they were always very kind and generous with their time. I must also mention Dr. Megan Oest, Dr. Rhima Coleman, Dr. Blaise Porter and Dr. Craig Duvall. Their excellent Ph.D. work laid the foundation for my studies, and it is because I have "stood on the shoulders of giants" that I have been able to achieve what I have. Finally, I sincerely acknowledge all the people who selflessly donated their time during my surgeries – it was definitely a team effort!

I must also mention the members of Wing 2-D, who has served both as my colleagues and friends. I would like to especially acknowledge David Dumbauld, Sean Coyer, Abbey Wajtowicz and Asha Shekaran from the Garcia lab. We have shared our ups and downs of the Ph.D. process, and that provided a much needed outlet for venting frustrations. Dave was co-chair with me on the Industry Committee, and I have enjoyed our many conversations in the lab and lair, including those of Industry vs. Academia. Dave, I will never forget the two goals you scored against MBA in 2006 – that is still my best intramural soccer moment! Sean is one of the easiest persons to talk to, and he has a special ability to make you feel very comfortable in a conversation. I have relished talking about professional careers and ambitions with him. Due to her involvement with

the segmental defect model, Abbey is considered an honorary member of the Guldberg lab. I thank her for her discussions on the vagaries of *in vivo* studies and her help with the GFOGER studies. I would be remiss if I did not acknowledge the supportive and affectionate staff of the IBB and BME, who have created a fantastic work environment at GT. I especially thank Vivian Johnson for her assistance over the years with paperwork and orders, and Sally Gerrish for her enthusiastic support to the volunteer activities I was involved with.

Next, I thank my close friends in Atlanta, Srinidhi Nagaraja, Kartik Sundereswaran, Kartik Balachandran, Smitha Kartik, Murali Padala, and Rahul Sathe. They made my stay in Atlanta a real pleasure and ensured that I had a fun time outside work. Srin is a former member of the Guldberg lab, and openly admits to feeling insecure when another Indian guy showed up in the lab. However, he was central in making me home in the lab and in Atlanta. I have immensely enjoyed his company, his humorous style and his kindness. Both of us have had unfulfilled dreams of becoming professional sportsmen, and we like to blame our Indian genes! Thanks to members of the Dr. Y lab, the Kartiks, KS and KB, and Murali, for the many potluck dinners (leading to numerous instances of food coma), Diwali celebrations and intramural soccer.

I would certainly not be where I am, if it were not for the unconditional love and support of my family. I thank my parents, Manohar and Sujata Kolambkar, for their total commitment to my personal and academic success. They have sacrificed many things in life so that my brother and I can have a good education. I am also grateful to my brother Navin and my sister-in-law Deepti for their support and encouragement over the years. I also thank my wife's parents, Amitava and Ruchira Chatterjee. They are exemplary role

models for me, and if I achieve even half their accomplishments, I will consider myself successful. Special thanks to Mum for being with us during the last few months of my thesis writing and helping us to care for Avika.

Finally, to say that I owe my Ph.D. to my wife, companion and friend, Ayona, would not be an exaggeration. Ayona has contributed so much to my life and this thesis that I am lost trying to think where to start. She has been tremendously generous with her time, and has been incredibly patient and understanding of my long work hours. Her multitasking skills and ability to get things done in short periods of time still continue to amaze me. The emotional support, constant encouragement and positivity that I received from her after failed experiments have sustained me during my Ph.D. Ayona even helped me prepare for surgeries by coming into the lab over weekends and working with me. In addition, her being a statistician has proven to be a big plus (hurrah for the Box-Cox transformation!). I vote for her to get an honorary degree in Bioengineering! Of course, I cannot forget our little baby girl, Avika, whose birth has brought a new meaning to my life. It was challenging (to say the least) to take care of a newborn and write the thesis at the same time. But Avika has given me so much joy, from her first chuckle to the first time she rolled on her tummy, that it more than makes up for the sleep deprived days and nights. I look forward to making up for lost time together with both Ayona and Avika.

TABLE OF CONTENTS

ACKNOWLEDGEMENTS iv

LIST OF TABLES xv

LIST OF FIGURES xvi

LIST OF ABBREVIATIONS xviii

SUMMARY xx

CHAPTERS

1. SPECIFIC AIMS 1

    Introduction 1

    Specific Aim I 2

    Specific Aim II 3

    Specific Aim III 3

    Significance 4

2. LITERATURE REVIEW 6

    Bone Structure and Function 6

        Introduction 6

        Short, flat and long bones 6

        Cortical and trabecular bone 7

        Bone matrix 8

        Woven and lamellar bone 9

        Bone cells and functions 9

        Periosteum and endosteum 11

    Bone Morphogenesis and Repair 11

        Bone formation and remodeling 11

        Fracture healing 13

        BMPs in skeletal development and fracture healing 14

Bone Regeneration and Clinical Therapies 16
Clinical need for bone regeneration 16
Clinical techniques for bone repair 17
BMPs in clinical practice 18
Research Strategies for Bone Repair 19
Tissue engineering/regenerative medicine (TE/RM) 19
Scaffolds 20
Growth factors and peptides 21
Cell sourcing and delivery 23
Growth factor delivery systems for tissue regeneration 25
Guided bone regeneration 28
Electrospun Nanofiber Meshes 29
Nanofiber mesh: an ECM-mimetic scaffold 29
Electrospinning setup 31
Nanofiber mesh: a 2-D or a 3-D scaffold? 31
3. COLONIZATION AND OSTEOGENIC DIFFERENTIATION OF DIFFERENT STEM CELL SOURCES ON ELECTROSPUN NANOFIBER MESHES 33
Introduction 33
Materials and Methods 35
Fabrication of nanofiber meshes 35
Nanofiber mesh morphology 36
Culture of AFS cells and MSCs 36
Cell culture on nanofiber fiber meshes 37
Cell viability 38
DNA content 38
Alkaline Phosphatase (ALP) activity 39
Calcium content 39

Calcein staining and quantification 40
Fourier Transform Infrared (FTIR) Spectroscopy 40
Cell delivery by nanofiber mesh *in vitro* 40
Data analysis 41
Results 42
Morphology of nanofiber meshes 42
Viability and colonization of hMSCs and hAFS cells over time 42
Osteogenic differentiation of hMSCs and hAFS cells: ALP activity 47
Osteogenic differentiation of hMSCs and hAFS cells: matrix mineralization 47
Nanofiber mesh as a cell delivery vehicle 52
Discussion 54
4. NANOFIBER ORIENTATION AND SURFACE FUNCTIONALIZATION MODULATE HUMAN MSC INFILTRATION AND OSTEOGENIC DIFFERENTIATION 58
Introduction 58
Materials and Methods 61
Electrospinning and nanofiber mesh characterization 61
GFOGER peptide preparation and nanofiber surface coating 62
Analysis of GFOGER surface coating 62
Human mesenchymal stem cell (hMSC) culture 63
Investigating cell infiltration on nanofiber meshes in an in vitro model 64
Role of cell proliferation in the cell infiltration model 66
Osteogenic differentiation and total DNA content on nanofiber meshes 67
Assessment of GFOGER coated nanofiber meshes *in vivo* 67
Data analysis 68
Results 68
Nanofiber mesh morphology and alignment 68

GFOGER coating of nanofiber meshes 69
Cellular infiltration on nanofiber meshes 73
Effect of cell proliferation on the infiltration of cells on nanofiber meshes 74
Influence of nanofiber coating and alignment on total DNA content and osteogenic differentiation 80
Assessment of GFOGER coated nanofiber meshes *in vivo* 83
Discussion 87
5. A NOVEL HYBRID SYSTEM FOR GROWTH FACTOR DELIVERY PROMOTES FUNCTIONAL REPAIR OF LARGE BONE DEFECTS 93
Introduction 93
Materials and Methods 95
Fabrication of nanofiber mesh tubes 95
Preparation of alginate hydrogel with and without growth factors 97
rhBMP-2 release kinetics 98
Surgical procedure and analysis 98
2-D radiographs and 3-D *in vivo* μCT imaging 99
Torsional testing 100
Histological analysis 101
Analysis of vascularity during bone regeneration 101
Statistical analysis 102
Results 102
Nanofiber mesh tube characterization and placement 102
Alginate release kinetics 103
Radiographs 105
In vivo μCT imaging 105
Biomechanical properties 106
Histological analysis 110

μCT–based angiography 112
Discussion 114
6. DELIVERY OF BONE MORPHOGENETIC PROTEIN WITHIN NANOFIBER MESH/ALGINATE ENHANCES SEGMENTAL BONE DEFECT REPAIR 119
Introduction 119
Materials and Methods 121
Nanofiber mesh tube fabrication and alginate preparation 121
Animal model and bone regeneration analysis 121
Data analysis 123
Results 123
Radiographs 123
μCT analysis 125
Biomechanical properties 126
Discussion 131
7. SUMMARY AND FUTURE DIRECTIONS 137
Overall Summary 137
Aim I: Nanofiber Meshes for Cell Culture and Delivery 138
Nanofiber mesh as a model cell culture surface 138
Nanofiber Mesh as a Cell Delivery Vehicle 139
Aim II: Modulation of Nanofiber Mesh Design 139
Mechanism of GFOGER action 140
Effect of fiber diameter, surface area and porosity 140
GFOGER immobilization on nanofiber surfaces 141
Promoting *in vivo* bone regeneration with nanofiber mesh tubes 141
Aim III: Nanofiber Mesh/Alginate Growth Factor Delivery System 142
The role of perforations in defect healing 142
Mechanical stimuli and tissue remodeling 143

Growth factor dosage 144
Growth factor delivery considerations 148
Delayed growth factor delivery 149
Conclusions 150
APPENDIX A: NANOFIBER MESH PROTOCOLS 151
APPENDIX B: CELL FUNCTION ANALYSIS PROTOCOLS 158
APPENDIX C: CAD DRAWINGS OF FIXATION PLATES 168
REFERENCES 170
VITA 195

LIST OF TABLES

Page

Table 2.1: The frequency and success rate of bone augmentation procedures at the Cleveland Clinic 17

Table 5.1: The four groups utilized in the *in vivo* study, with the implant conditions in each group 99

Table 6.1: Experimental groups 123

LIST OF FIGURES

Page

Figure 2.1. Histologic cross section of a cell-seeded electrospun nanofiber mesh. 32

Figure 3.1. Nanofiber mesh morphology. 44

Figure 3.2. Live/dead staining. 45

Figure 3.3. DNA content. 46

Figure 3.4. ALP activity. 49

Figure 3.5. Calcium quantification and FTIR analysis. 50

Figure 3.6. Calcein staining. 51

Figure 3.7. Cell-seeded nanofiber meshes for in vitro delivery. 53

Figure 4.1. Schematic of cell infiltration model. 65

Figure 4.2. Nanofiber mesh morphology. 70

Figure 4.3. Fiber and cell alignment on nanofiber meshes. 71

Figure 4.4. GFOGER coating of nanofiber meshes. 72

Figure 4.5. Kinetics of cell infiltration on uncoated random nanofiber meshes. 76

Figure 4.6. Effect of coating and fiber alignment on cell infiltration at 48 hours after strip removal. 77

Figure 4.7. Effect of mitomycin C on hMSCs proliferation on tissue culture plastic. 78

Figure 4.8. Role of cell proliferation in the cell infiltration model. 79

Figure 4.9. Early effect of GFOGER coating on hMSC number. 81

Figure 4.10. Effect of coating and fiber alignment on cell number and osteogenic differentiation of hMSCs in osteogenic media. 82

Figure 4.11. Radiographs of femurs implanted with nanofiber mesh tubes at 4 and 12 weeks. 84

Figure 4.12. μCT analysis and mechanical testing of extracted femurs at 12 weeks. 85

Figure 4.13. Histological analysis with H&E staining at 12 weeks. 86

Figure 5.1. Nanofiber mesh tubes and alginate hydrogel for surgery. 104

Figure 5.2. Representative radiographs at 4 and 12 weeks. 107

Figure 5.3. μCT analysis of bone regeneration at 4 and 12 weeks. 108

Figure 5.4. Mechanical properties of femora at 12 weeks. 109

Figure 5.5. Histological analysis at 12 weeks. 111

Figure 5.6. Vascular ingrowth at defect site at 3 weeks. 113

Figure 6.1. Representative radiographs at 2, 4 and 12 weeks. 124

Figure 6.2. Three-dimensional *in vivo* μCT images at 4 and 12 weeks. 127

Figure 6.3. Quantitative μCT analysis of new bone volume. 128

Figure 6.4. Mean density and connectivity density of the newly formed bone, obtained from μCT analysis. 129

Figure 6.5. Biomechanical properties of regenerated femurs at 12 weeks. 130

Figure 7.1. Long-term observation of a regenerated femur. 146

Figure 7.2. Dependence of rhBMP-2 dose on segmental bone defect repair. 147

LIST OF ABBREVIATIONS

BMP	Bone Morphogenetic Protein
rhMBP-2	Recombinant Human Bone Morphogenetic Protein-2
rhMBP-7	Recombinant Human Bone Morphogenetic Protein-7
OP-1	Osteogenic Protein-1
TE/RM	Tissue Engineering/Regenerative Medicine
ECM	Extracellular Matrix
hMSCs	Human Mesenchymal Stem Cells
hAFS cells	Human Amniotic Fluid Stem Cells
hESCs	Human Embryonic Stem Cells
GFOGER	Glycine-Phenylalanine-Hydroxyproline-Glycine-Glutamate-Arginine
TGF-β	Transforming Growth Factor-β
PCL	Poly(ε-caprolactone)
PLDL	Poly(L,DL, lactide)
GBR	Guided Bone Regeneration
VEGF	Vascular Endothelial Growth Factor
PDGF	Platelet Derived Growth Factor
IGF	Insulin-Like Growth Factor
FGF	Fibroblast Growth Factor
PLA	Polylactic Acid
PGA	Polyglycolic Acid
PLGA	Poly(lactic-*co*-glycolic acid)
PEG	Polyethylene Glycol
PPF	Poly(propylene) Fumarate

DBM	Demineralized Bone Matrix
3-D	Three-Dimensional
w/v	Weight/Volume
DCM	Dichloromethane
DMF	Dimethylformamide
HFP	Hexafluoro-2-Propanol
SEM	Scanning Electron Microscope
αMEM	Minimum Essential Medium Alpha
FBS	Fetal Bovine Serum
PBS	Phosphate-Buffered Saline
ALP	Alkaline Phosphatase
FTIR	Fourier Transform Infrared
TFA	Trifluoroacetic Acid
DAPI	4',6-Diamidino-2-Phenylindole
BrdU	5-Bromo-2'-Deoxyuridine
GMA	Glycol Methacrylate
MMA	Methyl Methacrylate
H&E	Hematoxylin and Eosin
RSA	Rat Serum Albumin
ELISA	Enzyme-Linked Immunosorbent Assay
CT	Computed Tomography
VOI	Volume of Interest
ANOVA	Analysis of Variance
ACS	Absorbable Collagen Sponge

SUMMARY

Bone defects caused by trauma, tumor resection or disease present a significant clinical problem. Failures in 'high risk' fractures and large bone defects have been reported to be as high as 30-50%. The drawbacks associated with current bone grafting procedures have stimulated the search for improved techniques for bone repair. Tissue engineering/regenerative medicine approaches promote tissue repair by providing a combination of physical and biological cues through structural scaffolds and bioactive agents. Though they have demonstrated significant promise for bone regeneration, very little has been translated to clinical practice.

The goal of this thesis was to investigate the potential of electrospun nanofiber mesh scaffolds for bone regeneration. Nanofiber meshes were utilized in a three-pronged approach. First, we validated their ability to robustly support osteogenic cell functions, including proliferation and matrix mineralization. We also demonstrated their efficacy as a cell delivery vehicle. Second, we investigated the effects of modulating nanofiber bioactivity and orientation on stem cell programming. Our results indicate that functionalization of nanofiber meshes with a collagen-mimetic peptide enhanced the migration, proliferation and osteogenic differentiation of cells. Fiber alignment improved cell migration along the direction of fiber orientation. Finally, a nanofiber mesh based hybrid system for growth factor delivery was developed for bone repair and tested in a challenging animal model. The delivery of bone morphogenetic protein (BMP) via this system resulted in the functional restoration of limb function, and in fact proved more efficacious than the current clinical standard for BMP delivery.

The studies performed in this thesis have suggested novel techniques for improving the repair of clinically challenging bone defects. They indicate that delivery of BMP via the hybrid system may reduce the dose and side effects of BMP, thereby

broadening the use of BMP based bone augmentation procedures. Therefore, this nanofiber mesh based system has the potential to become the standard of care for clinically challenging bone defects, including large bone defects, open tibial fractures, and nonunions.

CHAPTER 1

SPECIFIC AIMS

Introduction

The treatment of bone defects remains a challenging problem. The well known limitations of autografts and allografts have driven efforts to develop alternative therapeutic strategies for bone repair. Tissue engineering/regenerative medicine (TE/RM) research has focused on developing therapeutic strategies involving the delivery of biological agents along with biodegradable scaffolds. Both two- and three-dimensional scaffolds have been designed to provide a template for bone regeneration. The focus of bone regeneration strategies has been to create three-dimensional scaffolds having adequate strength to support *in vivo* loading. However, such scaffolds usually do not provide an optimal environment for cellular function and take a long time to degrade. Moreover, exogenous cells delivered *in vivo* at the center of these scaffolds may not survive due to the initial lack of vascularity at the defect. Thin, two-dimensional membranes have also been used for bone repair by placing them along the periosteal surface on the defect boundary. Though this technique (called guided bone/tissue regeneration) has been highly successful in the dental field for bone regeneration, it has not been quantitatively evaluated for the case of long bone defects. Over the last decade, recombinant human bone morphogenetic protein-2 (rhBMP-2) and rhBMP-7 have been approved by the U.S. Food and Drug Administration for spinal fusion, oral-maxillofacial applications and the treatment of certain fractures. However, challenges remain due to the suboptimal delivery systems, which have resulted in the use of supraphysiologic concentrations for generating a substantial healing response.

Electrospun nanofiber meshes have recently emerged as a new generation of scaffold membranes, possessing a number of features suitable for tissue regeneration.

They have fibers in the same size-scale of extracellular matrix (ECM) components and a large surface area, which improves cellular attachment, morphology and function. Nanofiber meshes can also be modified to add further design elements to enhance cellular interaction and elicit specific cellular responses. Due to these unique properties, they may therefore prove efficacious as a membrane for bone regeneration by guiding cell migration into bone defects and facilitating mineral deposition. In addition, nanofiber meshes may be useful for the delivery of osteogenic growth factors. **The *overall objective* of this project is to employ electrospun nanofiber meshes for the functional repair of large diaphyseal bone defects. Our *central hypothesis* is that nanofiber meshes are effective in directing stem cell proliferation, migration and differentiation *in vitro,* and thereby improve bone regeneration *in vivo*.** To this end, we propose the following specific aims:

Specific Aim I

Establish techniques for nanofiber mesh fabrication, and characterize stem cell colonization and osteogenic differentiation on nanofiber meshes.

The objectives of this aim were to develop protocols for nanofiber mesh fabrication, and to investigate the ability of nanofiber meshes to support osteogenic cell function and delivery. Our *working hypothesis* was that nanofiber meshes would support robust cell colonization and osteogenic differentiation *in vitro*. To accomplish this aim, we first developed techniques for electrospinning nanofiber meshes and nanofiber characterization. Next, we investigated the attachment, colonization and osteogenic differentiation of human mesenchymal stem cells (hMSCs) and human amniotic fluid stem (hAFS) cells on nanofiber meshes. We also compared the behavior of the stem cells on nanofiber meshes to that on tissue culture plastic. Finally, the ability of cell-seeded nanofiber meshes to serve as a cell delivery vehicle was investigated by studying its

effectiveness in colonizing three-dimensional scaffolds *in vitro*. The outcomes of this Aim are discussed in Chapter 3.

Specific Aim II

Analyze effects of nanofiber orientation and surface functionalization on stem cell infiltration and differentiation and on bone regeneration.

The objectives of this aim were to identify conditions that best support progenitor cells bridging bone defects and test the optimal design *in vivo*. Our *working hypothesis* was that presentation of a collagen-mimetic peptide on the nanofiber mesh surface and aligning nanofiber orientation will modulate cellular behavior *in vitro*, and enhance bone regeneration *in vivo*. Nanofiber meshes were coated with a triple-helical, type I collagen-mimetic peptide, containing the glycine-phenylalanine-hydroxyproline-glycine-glutamate-arginine (GFOGER) motif, to improve cell adhesion and osteogenic differentiation. An oriented topography was obtained by electrospinning aligned nanofibers in order to enhance cellular migration. We developed an *in vitro* model to examine hMSC infiltration on nanofiber meshes, and isolated the contribution of cell proliferation versus migration. The individual and combined effects of nanofiber functionalization and orientation on hMSC function were investigated. In addition, we assessed the efficacy of GFOGER coating to improve nanofiber mesh based repair of critically-sized segmental bone defects *in vivo*. The results of this Aim are discussed in Chapter 4.

Specific Aim III

Evaluate the potential of a nanofiber mesh based protein delivery system to functionally repair challenging bone defects.

The objectives of this aim were to develop and test a nanofiber mesh based system for the delivery of growth factors *in vivo*. Our *working hypothesis* was that

delivery of an osteoinductive growth factor within a nanofiber mesh/hydrogel system would enhance the functional repair of challenging bone defects, compared to hydrogel delivery and collagen matrix delivery. We first developed a hybrid protein delivery system that utilizes an electrospun nanofiber mesh tube and injectable alginate hydrogel. We tested the ability of this system to functionally heal segmental bone defects by the delivery of rhBMP-2. The effect of a perforated nanofiber mesh design on bone repair was also investigated. The nanofiber mesh/alginate BMP delivery technique was compared with the clinical standard of BMP delivery on collagen matrix. Finally, the role of the nanofiber mesh tube as a spatial constraint was investigated. The outcomes of this Aim are discussed in Chapters 5 and 6.

Significance

Musculoskeletal injuries remain a significant challenge for orthopaedic surgeons. Of the approximately 10 million fractures that are reported annually in the US, 5-10% do not heal spontaneously and require clinical intervention. Challenging injuries such as open tibial fractures and large bone defects have an even higher failure rate, estimated to be around 50%. These injuries result in severe pain, limited mobility and psychological distress, and therefore significantly impact the patient's quality of life. Current bone grafting procedures are moderately successful in repairing damaged bone, but lead to numerous secondary complications. Even BMP based bone augmentation procedures have experienced limited acceptance due to the large doses required. Thus, due to the limitations of the current procedures, more effective bone repair techniques are urgently needed. This work is *significant* because it has suggested novel approaches to improve the repair of clinically challenging bone defects by the employment of electrospun nanofiber meshes. We have developed innovative strategies for promoting bone regeneration by the delivery of biomolecular stimuli on biodegradable nanofiber meshes. In addition to thorough *in vitro* characterization of cell behavior on nanofiber meshes, we

tested their efficacy *in vivo* in a challenging animal model. Using quantitative tools for analyzing bone regeneration, we have demonstrated that a nanofiber mesh based system for rhBMP-2 delivery results in the functional repair of critically-sized segmental bone defects. In fact, our system proved superior to the current clinical standard of rhBMP-2 delivery on collagen sponge. This study suggests that nanofiber mesh based techniques for bone repair have the potential to advance the clinical treatment of bone defects. As the delivery of bioactive factors on biodegradable scaffolds is a central concept in the regeneration of injured or diseased tissues, the strategies developed in this study may contribute to the treatment of other musculoskeletal defects, such as those in cartilage, tendons and ligaments.

CHAPTER 2

LITERATURE REVIEW

Bone Structure and Function

Introduction

Knowledge of the complex, dynamic structure of bone and an understanding of its physiological functions are essential for the treatment of injuries of the musculoskeletal system. Bone performs several functions in the human body [1, 2]. Bone serves as a reservoir of several essential ions, such as calcium and phosphate. The exchange of these ions with the extracellular fluids maintains a tight control of their fluid concentrations, which is necessary for critical physiological functions. In addition, trabecular bone and marrow cavities are host to the haematopoietic marrow, which supplies the body with nutrient-carrying red blood cells, infection-fighting white blood cells, and tissue-forming progenitor and stem cells. Finally, as the main constituent of the adult skeletal system, bone supports and provides structure to tissues, protects vital organs and provides attachment sites for muscles that are essential for body movements. Unlike other functions, this mechanical function of bone occurs at a local level, and if lost due to injury to the tissue, has to be regained to maintain skeletal continuity. This restoration of bone function drives the development of clinical strategies for bone repair.

Short, flat and long bones

Bone can be described in a number of ways, depending on the structural level of interest. On the basis of general shape, bones can be classified as short, flat and long [3]. Short bones, such as vertebral bodies and tarsals, are approximately the same size in all dimensions. On the other hand, cranial bones are examples of flat bones, which are shorter along one direction. Long bones, such as the femur and tibia, are cylindrical in

shape with wider ends, and are the larger bones in the body. They are described by three regions: diaphysis, metaphysis and epiphysis, based on the location with respect to the 'physis' or growth plate [1]. The growth plate is the region near the end of long bones from which bone grows during development. The diaphysis ('between the physis') is the central tubular region of a long bone. The metaphysis ('next to the physis') refers to the transitional region between the diaphysis and the flared ends. The epiphysis ('upon the physis') is the portion of long bones beyond the growth plate, towards the ends.

Cortical and trabecular bone

The next hierarchical level of structure, which can be observed from gross examinations of bone cross section, divides the bone into cortical (compact) and trabecular (cancellous) bone [2]. Cortical bone correspond to dense areas without cavities (approximately 10% porosity), while trabecular bone corresponds to spongy areas with numerous interconnecting cavities (50-90% porosity) [3]. This difference in structure results in cortical bone possessing a much higher compressive strength than trabecular bone. In contrast, the high surface area of the trabecular network permits greater deformation and energy absorption. The cortical bone is responsible for the supportive and protective functions of the skeleton, whereas the trabecular bone represents the primary site of bone's metabolic functions. It should, however, be noted that both cortical and trabecular bone have the same microstructure and matrix composition; the differences arise due to the distinct arrangement of the microstructure. Mature cortical bone consists of a repeating set of concentric layers (lamellae) of tissue called a haversian system or osteon (described below). The much less dense trabecular bone is comprised of an array of plates and rods connected to form a porous structure. In long bones, the epiphysis is composed of trabecular bone in the interior surrounded by a thin layer of cortical bone on the outside. On the other hand, the diaphysis is almost exclusively composed of compact bone.

Bone matrix

As mentioned previously, at the ultrastructural level, bone tissue is composed of the same bone matrix. The extracellular matrix (ECM) of bone is a composite material consisting of an inorganic and an organic component. The inorganic and organic matters contribute approximately 65% and 20%, respectively, to the wet weight of bone. The remaining weight is accounted by water [3]. The inorganic component of bone is comprised of mineral crystals containing mainly calcium and phosphorus. In addition, the crystals include sodium and magnesium to a lesser extent. Significant quantities of amorphous calcium phosphate are also present in the organic matrix. It was thought that the mineral crystals were composed purely of calcium and phosphorus based hydroxyapatite ($Ca_{10}[PO_4]_6[OH]_2$). However, recent studies have shown that they contain both carbonate and acid phosphate groups [4, 5]. The organic component consists of predominantly of type I collagen, making up approximately 90% of this component. The other 10% consists of non-collageneous glycoproteins and bone-specific proteoglycans, which includes osteocalcin, osteopontin and bone sialoprotein. These non-collageneous proteins are thought to influence the organization and mineralization of the bone matrix. Bone matrix also contains growth factors that regulate bone cell function, such as bone morphogenetic proteins (BMPs), insulin-like growth factor-1 (IGF-1) and members of the transforming growth factor-β (TGF-β) family. The organic matter gives bone its form and tensile strength, while the inorganic component provides the compressive strength. However, it is the association of the mineral phase with the collagen fibers that is responsible for the unique combination of hardness and toughness that the bone tissue possesses. The inorganic matrix, in addition, acts as the ion reservoir in maintaining homeostasis.

Woven and lamellar bone

Another classification of bone tissue is based on the organization of the bone matrix. According to this classification, there are two types of bone tissue: woven (immature; primary) and lamellar (mature; secondary) bone [2]. In woven bone, the collagen bundles are randomly placed, whereas those in lamellar bone are positioned in tightly organized parallel sheets, forming distinct lamellae having a thickness of 4-12-μm [3, 6]. Woven bone is the first bony tissue that is deposited during embryogenesis and repair. It is replaced by lamellar bone after the remodeling process, and found only in small amounts in adults. Woven bone also has a much higher concentration of cells than lamellar bone. The collagen lamellae in lamellar bone are parallel to each other or organized concentrically around a vascular canal. The entire complex of concentric lamellae surrounding a canal containing blood vessels, nerves and loose connective tissue is called a haversian system or osteon [2]. Due to the variation in matrix organization between the two bone tissue types, woven bone is weaker but more flexible than lamellar bone.

Bone cells and functions

The unique self-healing capacity of bone can be partly attributed to the presence of diverse cell types. The three main cell types in bone tissue are osteoblasts, osteocytes and osteoclasts [2, 3]. The osteoblasts are located on the surfaces of bone tissue, and pack tightly against adjacent osteoblasts. They are responsible for the synthesis and secretion of the organic matrix of bone. In addition, they influence mineralization and remodeling of bone matrix. When osteoblasts are active in matrix synthesis, they have a cuboidal to columnar shape and demonstrate high alkaline phosphatase activity. In this phase, they also contain abundant endoplasmic reticulum, Golgi membranes and mitochondria. As the osteoblasts secrete matrix in their surrounding region, they become embedded in the tissue and turn into osteocytes. Some osteoblasts remain on the surface of bone with

reduced activity, and some are removed from the region by an as yet unknown mechanism [3].

The osteocytes are involved in the maintenance of the bone matrix. They are surrounded by bone matrix, and therefore appear to lie in cavities called lacunae. In lamellar bone, osteocytes are found in lacunae that are located between and occasionally within lamellae. The osteocytes extend long, branching cytoplasmic processes through canaliculi that make contact with adjacent cells via gap junctions. It is through these connections that flow of small molecules and ions occur. These connections are essential not only for nutrient and metabolite transport, but also for intercellular signaling, which is required for bone maintenance and adaptation.

The osteoclasts are large, extensively branched, multinucleated cells that are involved in the resorption and remodeling of bone tissue. Unlike other bone cells, they are derived from the hematopoietic lineage and share similarities with monocytes. When activated for the resorption of bone, the osteoclasts bind to the surface of bone, creating a sealed space. The osteoclast membrane facing bone matrix is extensively folded to trap small particles and increase resorptive area. Transmembranous proton pumps transport protons into the sealed space, creating an acidic environment that solubilizes the bone mineral [7]. The osteocytes secrete acid proteases to degrade the remaining organic matrix.

In addition to the three main cell types, bone-lining cells that lie directly against the bone matrix have been identified [3]. They appear to have a role in attracting osteoclasts and stimulating them to form bone. Also, undifferentiated mesenchymal cells with the potential to differentiate into osteoblasts reside in the bone marrow, blood vessels, periosteum, endosteum and surrounding tissues [3, 8].

Periosteum and endosteum

The external and internal surfaces of bone are called periosteum and endosteum, respectively. These surfaces are covered with thin tissue bilayers, comprising of cells and connective tissue. The periosteum, especially, has been demonstrated to possess considerable mechanical and biological importance. It consists of two layers: an outer dense layer of collagen fibers and fibroblasts, and an inner layer that contains progenitor cells and blood vessels. The periosteum provides an important part of the blood supply to the bone, and therefore is essential for its viability. The progenitor cells of the inner layer have been demonstrated to play an important role in bone growth and repair [9, 10]. In fact, they are thought to drive the callus formation and subsequent remodeling during fracture healing [11]. The periosteal cells have also been isolated and utilized for bone tissue engineering [12].

Bone Morphogenesis and Repair

Bone formation and remodeling

Developmentally, there are two paths of forming bone: intramembranous ossification and endochondral ossification, though both share the same mechanism of matrix development [13]. The common mechanism of bone matrix formation involves the differentiation of progenitor mesenchymal cells into osteoblasts, which then secrete the specialized bone matrix. As this matrix mineralizes, the osteoblasts are encapsulated in the matrix, and become osteocytes. The initial bone that is deposited is an immature woven bone, which is then remodeled into mature lamellar bone. Bone remodeling results from osteoclast resorption and osteoblast deposition of bone, through a sequence of tightly coordinated events [13].

In intramembranous ossification, the matrix formation is initiated by the aggregation of the progenitor mesenchymal cells into layers or membranes at discrete

locations. Several such locations arise simultaneously and then fuse to impart a trabecular-like structure to the developing bone. Numerous such ossification centers occur within the bone tissue, which grow radially and merge together to form the whole bone. Most flat bones of the human body, like the frontal and parietal bones of the skull, are formed by intramembranous ossification.

Unlike intramembranous ossification, endochondral ossification occurs within a cartilaginous tissue that is first formed from mesenchymal tissue. This type of ossification is primarily responsible for the formation of long bones like the femur and tibia. It begins with the aggregation of undifferentiated mesenchymal cells that differentiate into chondrocytes and secrete a cartilaginous matrix. This hyaline cartilage tissue takes the shape of the bone that is to be formed. Next, part of the cartilage matrix is calcified, and the chondrocytes die after undergoing hypertrophy. An osteogenic bud, consisting of osteoprogenitor cells and blood capillaries invades the cartilage. The osteoprogenitor cells differentiate into osteoblasts, and bone formation progresses on the remnants of the calcified cartilage matrix.

In addition to the deposition of bone matrix with the necessary composition, normal mechanical function of the musculoskeletal system requires the formation of bones of appropriate shape and size. Long bones develop from cartilaginous models through the endochondral ossification process. However the process is preceded by the formation of a bone collar in the perichondrium by means of intramembranous ossification [2]. As the endochondral ossification progresses, the calcified cartilage matrix is resorbed by chondroclasts. This process first occurs in the diaphysis, in what is known as the primary ossification center. Bone grows longitudinally from the primary ossification center, with resorption of the bone at the center, creating the hollow tubular structure, characteristic of long bones. Secondary ossification centers arise at the center of each epiphysis, and grow radially. The diaphysis and epiphysis are separated by the epiphyseal cartilage, also called the growth plate. Long bones grow longitudinally by the

replacement of the epiphyseal cartilage by bone tissue on the diaphyseal side. The enlargement of the width of long bones occurs by appositional growth of the bone collar, in which osteoblasts synthesize new bone matrix on an existing bone surface.

Fracture healing

Bone is one of the few adult tissues with the capacity for true self-healing. Unlike soft tissue injuries, which generally result in the formation of scar tissue, bone healing concludes with the actual reconstitution of the injured tissue, including the biochemical and biomechanical properties. Bone fracture healing involves both intramembranous and endochondral ossification pathways, in a process that recapitulates embryonic bone formation to a large degree [14].

When bone fractures, the following events occur sequentially: hematoma formation, acute inflammation, cartilaginous callus formation and calcification, neovascularization, callus mineralization, and remodeling [15, 16]. The cascade starts with the leakage of blood from the damaged blood vessels and a hematoma is formed. Platelets in the hematoma release vasoactive mediators and growth factors [1]. Acute inflammation follows, and the damaged cells and tissue are removed by macrophages. The ends of the bone do not participate in the healing response, and are in fact dead [17]. Progenitor and stem cells, first from the periosteum and later from adjacent sites, are mobilized and ultimately form a callus tissue, which surrounds the fracture and occupies the space between the fracture ends. In addition to a mainly cartilaginous matrix, the fracture callus consists of osteoblasts and woven bone deposited by intramembranous ossification. The callus bridges the fracture and achieves stabilization of the fracture fragments. Once cartilage is calcified, it is invaded by blood vessels, bringing osteoprogenitor cells with them. The cartilage is resorbed by chondroclasts, and immature woven bone is deposited by differentiated osteoblasts, much like what occurs in embryonic long bone development. Once the callus is mainly composed of woven

bone and unites the fracture ends with bony tissue, the woven bone undergoes chronic remodeling into lamellar bone and the native bone structure is restored.

Fracture healing is influenced by numerous internal and external factors. For example, growth factors from the BMP family have been investigated extensively for the induction of osteogenesis at fracture sites, and are used clinically for the treatment of challenging fractures [18]. The BMPs have been shown to induce a cascade of chemotaxis, mitosis and osteogenic differentiation of undifferentiated mesenchymal cells [19]. In addition, they have been characterized for their ability to couple angiogenesis and bone formation [20, 21]. The fixation technique used for fracture stabilization also has a profound effect on the healing response [22, 23]. In less stabilized fractures, the endochondral route of ossification dominates, and results in the classical fracture healing cascade, as outlined above [23]. In fact, the periosteal response to fracture is enhanced by moderate motion and inhibited by rigid fixation [17]. Conversely, fractures are healed predominantly by intramembranous ossification only when the bone ends are rigidly fixated with respect to each other. It should, however, be noted that excessive motion at the fracture site inhibits vascularization and prolongs the cartilaginous callus phase [22, 24].

BMPs in skeletal development and fracture healing

In 1965, Marshal R. Urist made the key discovery that when dimineralized bone matrix from rabbits was implanted in an intramuscular pouch in rats, it lead to the formation of new bone [25]. He later identified a protein responsible for this effect, which was termed bone morphogenetic protein. In 1988, Wozney et al. identified the genetic sequence of the protein, which made the production of BMPs possible by recombinant DNA technology [26].

BMPs, which are part of the TGF-β superfamily, are one of the most potent agents known for bone induction. More than 15 members of the BMP family have been

currently identified, which are essential during the embryogenesis of bones, brain, eyes, heart, kidneys and teeth [19, 27, 28]. Mice deficient in BMP-2, -4, and -7 die either during embryonic development or soon after birth [29]. The deficiency of BMP-2 in mice has been associated with developmental abnormalities of skull, hindlimb, and kidney [30]. In addition, BMP-2, 4 and 7 are known to play a critical role in bone healing in adults [29, 31]. Currently, recombinant BMP-2 and -7 have been approved by the Food and Drug Administration (Rockville, MD) for certain clinical bone repair therapies.

BMPs are pleiotropic regulators of cell function, and have been demonstrated to play a pivotal role in the growth and differentiation of numerous cell types [30, 32]. Bone marrow derived mesenchymal stem cells (MSCs) and osteoprogenitor cells undergo osteogenic differentiation to a mineralizing phenotype in response to BMPs [33-36]. For example, Lecanda et al. reported that incubation of human MSCs and osteoblasts with BMP-2 inhibited proliferation, and induced matrix mineralization and upregulation of osteopontin, bone sialoprotein and osteocalcin [36]. In addition, BMPs stimulate cell chemotaxis of MSCs, which is especially important in recruiting endogenous cells for tissue repair [37-39]. BMPs are dimeric molecules, and trigger intracellular effects by binding to serine/threonine kinase receptors. The binding of BMPs to their receptors triggers the activation of intracellular signaling proteins called SMADs, which then enter the nucleus and modulate the expression of transcription factors [32].

BMPs are also known to be essential for the inherent fracture healing response [32]. In fact, fractures in BMP-2 deficient mice do not resolve spontaneously [31]. The individual BMPs play important yet distinct roles during fracture repair [40]. Studies have shown that the expression of BMP-2 and -4 is upregulated in MSCs that migrate to a fracture site, while BMP-2, -4 and -7 are present in the newly formed woven bone [41, 42]. For instance, Bostrom et al. characterized the temporal and spatial distribution of BMP-2 and -4 in fracture healing using a monoclonal antibody specific to these BMPs [41]. They reported that the BMP levels were high in the inner layer of the periosteum

immediately after fracture, in the chondroprogenitor cells and in the osteoblasts that lined the calcified cartilage matrix. Conversely, BMP expression went down as the lamellar bone replaced the woven bone.

Bone Regeneration and Clinical Therapies

Clinical need for bone regeneration

The need for bone regeneration occurs in cases of bone loss due to trauma, tumor resection or disease. In addition, bony tissue formation is needed for joint arthrodesis such as spinal fusion. The frequency and success rate of bone augmentation procedures obtained at one clinical center is listed in Table 2.1. Joint arthrodesis is the most common procedure performed at this center, followed by fracture repair. On the other hand, fracture nonunions and large bone defects have been reported less commonly. Overall, most of the conditions have been treated with high success rates at this center, other than the notable exception of large bone defects. However, it should be kept in mind that successful treatments include bone grafting procedures, which are associated with numerous secondary disadvantages. Moreover, it should be noted that in addition to large bone defects, the treatment of nonunions and certain cases of fractures has proved to be challenging. Failures in 'high risk' fractures have been reported to be as high as 30% [18]. For example, open tibial fractures remain a persistent problem. A recent clinical trial on open tibial fracture treatment showed that one year after injury, more than half of the patients managed with the standard of care had treatment failure [43]. Another study demonstrated that seven years after surgery, half of the patients still reported appreciable disability [44].

Impaired fracture and bone defect healing are associated with pain and stiffness of surrounding joints, leading frequently to patient disability [45]. In addition, high rates of psychological distress have been reported after trauma [46]. This places a considerable

economic burden on the patient and society. The cost of bone grafting procedures alone is estimated to be currently $2.5 billion per year [47]. Long-term rehabilitation and the indirect cost of lost wages add to the economic burden to the healthcare system. There is therefore a significant clinical need for improving bone regeneration, especially in the cases where the current techniques are not adequate.

Table 2.1. The frequency and success rate of bone augmentation procedures at the Cleveland Clinic (Cleveland, OH). Data courtesy Dr. George Muschler

	% Frequency	% Success
Arthrodesis	60%	80-90%
Fracture	20%	95%
Cavity	10%	~100%
Allograft Host Junctions	<1%	95%
Nonunion	5%	80-90%
Defects (>2 cm)	3%	<50%

Clinical techniques for bone repair

Traditional orthopaedic practice relies on the ability of the surgeon to drill, cut ream and realign bone [3]. The success of these procedures requires technical skill and well-designed hardware. In a majority of cases, this is sufficient for healing, thanks to the remarkable capacity of bone for self-regeneration. However, certain fractures and bone defects require additional bone augmentation, as noted above. The current procedures for bone augmentation include autologous and allogeneic bone grafting, and more recently ceramic and composite substitutes for bone grafts [45, 48, 49]. Approximately 500,000 bone grafting procedures are performed in the U.S. and 2.2 million worldwide [50, 51].

The clinical gold standard for bone regeneration has been autologous bone grafting as it provides osteogenic cells and osteoinductive factors for bone healing [49]. Though it has been successful in many cases, it has significant disadvantages including limited graft material and morbidity of the donor site [52, 53]. These limitations have led to increased use of allograft bone as a substitute for autologous bone. However, allograft bone is inferior to autologous bone due to reduced biological activity after processing, and is associated with a high rate of complications and late fractures as well as a risk of disease transmission. The high failure rate of allografts is associated with their lack of ability to revascularize and remodel [54-56]. Ceramic and polymer based bone graft substitutes have recently been introduced, and are being used frequently. But ceramics tend to be brittle, whereas polymers suffer from limited bioactivity and strength, and may need to be supplemented with osteogenic cells and growth factors [51]. These limitations of the grafting procedures have stimulated the search for improved techniques for bone repair.

BMPs in clinical practice

In the last decade, recombinant human BMP-2 (rhBMP-2) and -7 (rhBMP-7) have been approved for clinical use. In addition to spinal applications, rhBMP-2 delivered on a type I collagen sponge is approved for open tibial fractures [43, 57]. The use of rhBMP-7 (also known as osteogenic protein-1 (OP-1)) on a type I collagen carrier is allowed for the treatment of tibial nonunions and in limited cases of spinal fusion [58, 59]. A prospective, controlled, randomized clinical trial was performed to investigate the efficacy of rhBMP-2 for treatment of open tibial fractures along with intramedullary nail fixation [43]. It was reported that rhMBP-2 treatment resulted in a 29% reduction in nonunion and a 41% reduction in secondary intervention, compared to intramedullary nail alone.

Although BMPs have been quite successful in fracture healing, high doses (3.5-12 mg) are required. In the 2002 BMP-2 clinical trial, only a 1.5 mg/mL dose, and not a 0.75

mg/mL dose was found to be superior to the standard of care. The need for such large doses is probably related to the inefficient delivery of the growth factor on collagen sponge. The high doses have resulted in complications due to the diffusion of the BMP away from the application site [60, 61]. BMP usage is also considered expensive due to the high doses required, and surgeons typically avoid using it until other treatment options have been exhausted [62]. Garrison and coworkers have performed a cost effectiveness study of BMPs in orthopaedic practice in the U.K [63]. They reported that the incremental cost of BMP for open tibial fractures was about £3.5 million per year. The cost effectiveness ratio was found to be sensitive to the price of BMP and severity of the fracture. They concluded that the cost effectiveness of BMP may be improved if its price is reduced or if it is mainly used in severe cases. Therefore, delivery systems that can reduce BMP dose by enhancing delivery efficiency are urgently needed to improve the cost effectiveness of BMP therapy.

Research Strategies for Bone Repair

Tissue engineering/regenerative medicine (TE/RM)

Though bone grafting remains the standard for clinical bone regeneration, there is a clear need for effective bone repair techniques. The basic elements required for successful bone repair include an extracellular matrix, cells, osteoinductive factors and a vascular supply. TE/RM approaches attempt to provide one or more of the above to mimic the natural process of bone regeneration [64, 65]. Historically, tissue engineering was defined as the development of biological *substitutes* for damaged tissues and organs [66]. Tissue substitutes are created *in vitro* by the culture of cells on scaffolds in an appropriate environment, with the goal of using for transplantation *in vivo*. As the tissue is primarily created *in vitro* in this approach, this can be termed as *in vitro* tissue engineering [67]. The pioneering tissue-engineered products were skin substitutes

produced using this method [68]. This approach has been found to be suitable for thin tissues with low vascularity and low regenerative potential, such as cartilage [69, 70]. On the other hand, the creation and post-implant viability of large vascularized tissues, such as bone, remain a significant challenge because of mass transport limitations in the absence of a vascular supply [71]. Fortunately, for bone and other tissues with high healing potential, strategies that promote the activation of endogenous repair mechanisms with minimal *in vitro* processing have been successful [72-74]. This could involve, for example, delivery of growth factors that stimulate the endogenous cells to migrate to the injury site and initiate repair. This approach, termed *in vivo* tissue engineering, has the significant advantages of requiring less processing and culture time, and therefore presents a more viable method for regulatory approval and commercialization.

The current definition of tissue engineering encompasses both the *in vitro* and *in vivo* approaches, and has come to mean the replacement, repair and/or regeneration of tissues and organs [75]. In addition, regenerative medicine, which has been synonymous with stem cell technology, has been added to the definition due to its complementary relationship with tissue engineering, and the entire field is now called TE/RM [76]. TE/RM strategies for bone repair encompass a broad set of approaches typically involving a scaffold and a biological component [64, 65, 77]. The biological factor includes cells, proteins, peptides or genes, or a combination of these [77-83].

Scaffolds

Scaffolds are the central concept in TE/RM as they provide the template for tissue regeneration. In addition to their structural role, advances in the field of biomaterials have resulted in bioactive scaffolds capable of influencing cell behavior [84, 85]. Scaffolds for tissue regeneration have been manufactured from techniques such as rapid prototyping, salt leaching, self-assembly, phase separation, gas foaming and electrospinning [65, 86-90]. The most frequently used scaffolds in bone TE/RM research are three-dimensional

structural scaffolds having large pore sizes [74, 87, 91]. They are typically made from synthetic polymers like poly(ε-caprolactone) (PCL) and poly(L,DL, lactide) (PLDL), or ceramics like hydroxyapatite and calcium phosphate. Though successful for promoting bone formation, structural scaffolds usually do not provide an optimal environment for cellular function and typically suffer from slow resorption kinetics, thereby impeding functional restoration of the damaged tissue. Oest et al. reported that PLDL scaffolds infused with rhBMP-2 promoted bone ingrowth but failed to fully restore the mechanical properties of long bone defects [74]. They hypothesized that minimal degradation of the material at 16 weeks resulted in confining the bone formation to the pores and the periphery of the scaffold [74]. In contrast to the three-dimensional structural scaffolds, two-dimensional membranes have been used to promote bone repair by placing them along the periosteal surface in a process termed guided bone regeneration (GBR) [92-95]. Due to their placement on the edge of the defect, the space inside the defect is available for tissue deposition, which may lead to the complete restoration of the bone. Nanofiber meshes, made by electrospinning, are scaffold membranes with the potential of being efficacious in GBR. Their nanometer range fibers mimic the structural characteristic of ECM and improve cell attachment and function [96-98]. Nanofiber meshes will be discussed in detail in a later section. Another class of scaffolds of interest is the hydrogel, which has gel-like consistency [99, 100]. Though their mechanical properties are much lower than bone tissue, they can be injected using minimally invasive procedures, and permit cell migration and remodeling. In addition to functioning as scaffolds, they can be used for delivering biologics to the defect site. Hydrogels will be discussed further below.

Growth factors and peptides

Growth factors are signaling proteins secreted by cells that act on target cells to modulate cell functions like migration, proliferation and differentiation [29]. After binding to receptors on the target cells, they induce an intracellular signal transduction

cascade that produces a biological response. The growth factors most frequently utilized for bone formation are from the BMP family, which have been successfully translated to the clinical setting [30, 101]. In addition to the BMPs, other members of the TGF-β superfamily have also been investigated for their potential to enhance bone repair. Critchlow et al. evaluated the effect of exogenous TGF-β2 on the healing of rabbit tibial fractures [102]. They reported that a higher dose of TGF-β2 (600-ng), in the presence of stable mechanical fixation, resulted in abundant callus formation but no increase in bone content in the callus. The angiogenic growth factor, vascular endothelial growth factor (VEGF), has been demonstrated to enhance mineralization and callus maturation in murine fractures [103]. Finally, platelet derived growth factor (PDGF), insulin-like growth factors (IGF) and fibroblast growth factors (FGF) have also been investigated for bone repair, with mixed results [29, 104]. As bone repair is regulated by a complex set of growth factors, combination of the above growth factors have also been attempted. A synergistic effect of TGF-β3 and BMP-2 delivery on bone formation was seen by Simmons et al. in an ectopic murine model [105]. Co-delivery of angiogenic and osteogenic factors have also been demonstrated to promote bone repair subcutaneously [106]; however, this effect was not seen in an orthotopic model [107].

An alternative to full-length proteins, including growth factors, are peptides that mimic specific regions of these proteins. Whole proteins suffer from purification and processing issues, and can result in a host immunogenic response [108-111]. On the other hand, short-length peptides can be made synthetically to avoid these issues, and furthermore would cost much less. Saito and coworkers have developed a novel peptide corresponding to residues 73-92 of BMP-2 [112]. They demonstrated that this peptide promotes osteogenic differentiation of progenitor cells and induces mineralization *in vivo* [113, 114]. As opposed to being presented in soluble form, peptides can also be coated onto biomaterial surfaces. These ECM-mimetic material surfaces present adhesion motifs to engage the signal transduction machinery of cells for directing cellular response and

tissue repair [115, 116]. A further advantage of using peptides over a full-length ECM protein in such a scenario is that they can be designed to mimic individual domains of proteins, resulting in the engagement of specific cellular receptors, and therefore generating a concerted cellular response. One such peptide that has been identified from the type I collagen molecule is a triple-helical peptide that contains the glycine-phenylalanine-hydroxyproline-glycine-glutamate-arginine (GFOGER) motif. The GFOGER motif has been identified as the major site of interaction between the type I collagen molecule with the $\alpha_2\beta_1$ integrin receptor. This interaction has been found to be the key signal for the osteogenic differentiation of cells [117-119]. Recently, Reyes and coworkers demonstrated that coating surfaces with GFOGER enhanced the osteogenic differentiation of osteoblasts and MSCs, and improved osseointegration of titanium implants [120, 121].

Cell sourcing and delivery

Although acellular approaches to bone reconstruction using scaffolds and BMPs have shown moderate clinical success, the delivery of osteogenic cells may be required for patients with a reduced local supply of responsive osteoprogenitor cells. This includes older patients, smokers, patients receiving chemotherapy or radiation, and patients with severely damaged wounds or metabolic diseases [122]. For a cell based therapy to be successful in regenerating bone it is necessary to identify an appropriate cell source that is easily accessible, can be expanded to large numbers, and has osteogenic potential [123, 124]. Of the numerous cells types studied for bone tissue engineering, mesenchymal stem cells (MSCs) derived from the bone marrow have been extensively investigated, and have been shown to promote repair of critically-sized defects in pre-clinical animal studies [125-127]. However bone marrow MSCs have limitations to the extent of their self renewal capacity [128, 129], and have also shown loss of differentiation abilities with age of the donor [130, 131]. Recently pluripotent cells have been isolated from the human

and rodent amniotic fluid [132] that express c-Kit , which is the receptor for stem cell factor. These cells, termed amniotic fluid-derived stem (AFS) cells, have shown remarkable ability to differentiate into cells of all three embryonic germ layers. In addition AFS cells proliferate rapidly without feeder cells and have not shown tumorigenicity, thus making them an exciting new source of regenerative cells. Our lab has recently developed protocols to differentiate them along the osteogenic and chondrogenic lineages [133, 134].

It is well known that static *in vitro* culture of three-dimensional tissue-engineered constructs greater than 1 mm usually results in a thin shell of viable cells and tissue on the periphery [135-138]. It is thought that this effect is due to the limited mass transport of vital nutrients to the center of the construct. Similarly in the case of segmental bone defects, the lack of initial vascularity limits the transport of nutrients to and waste products from the center of the defect. Typically, when cellular constructs are used *in vivo*, the cells are seeded throughout a 3-D scaffold and placed at the injury site. However, due to the reasons mentioned above, cells located at the center of the scaffold may not survive [139, 140]. An alternative method may be to deliver cells within a tissue-engineered periosteum, on the periphery of the defect, where the presence of a neighboring vasculature may enhance cell survival. With time, as a continuous vasculature is established at the center, the cells may migrate towards the center due to the improved transport environment. Recently Zhang reported that engraftment of BMP-2 producing BMSCs using gelfoam wrapped around nonvital allografts improved allograft incorporation and repair [141]. Due to their unique structural properties, electrospun nanofiber meshes promote cellular attachment and proliferation, and therefore may be used for such a cell delivery system.

Growth factor delivery systems for tissue regeneration

Due to their important role in regulating tissue formation and maintenance, growth factors have the potential to be clinically successful in repairing injured tissues [142]. The direct injection of growth factors in a bolus dose is generally not effective due to the short protein half-life *in vivo* and the rapid protein diffusion through vascular networks [143]. Multiple injections to the injury site are not feasible due to the high cost of growth factors and repeated hospital visits. In addition, protein diffusion of osteogenic growth factors like BMPs into non-bony tissues may result in an unwanted and uncontrolled ectopic bone formation [60, 144]. For instance, when rhBMP-2 solution is soaked on a collagen sponge, the retention at defect site is prolonged compared to bolus delivery [145]. In one study, an extremely high dose of 80-μg rhBMP-2 was required in a rat femoral fracture model with a percutaneous injection [146]. For these reasons, protein delivery systems that can provide controlled release and local retention are required for the efficacy of growth factor based therapies [143, 147].

There are several considerations in designing delivery systems for tissue regeneration [143]. A unique aspect of drug delivery for tissue repair is the need of a structural template for guiding the repair process. Therefore, drug delivery vehicles should have the ability to be configured as scaffolds, or at least be able to be loaded onto scaffolds. The scaffolds should have the structural and biological properties to support robust cell and tissue infiltration. The delivery vehicle must be biodegradable, biotolerant, and protect against protein degradation and denaturation *in vivo*. The delivery system should achieve spatiotemporal release of the protein, including an appropriate protein release rate and retention of the growth factor within the injury site. The proteins are typically released from the delivery vehicle due to a combination of protein diffusion and matrix degradation. Finally, in order to minimize protein denaturation, the methods of fabrication should not involve harsh solvents or high temperatures.

A variety of growth factor delivery systems have been developed with the above design criteria in mind (for a review see [148]). Based on composition, the major categories of growth factor delivery systems being currently investigated for bone repair are [149, 150]: (1) Natural materials, (2) Inorganic materials, (3) Synthetic materials, and composites of the above. Natural materials include collagen, hyaluronans, chitosan, fibrin, agarose and alginate [151-153]. These typically exhibit good biotolerance and biodegradation profiles, and can be manufactured in numerous formulations. Inorganic systems, made from bioglass or ceramics such as hydroxyapatite, calcium phosphate and calcium sulfate, are being investigated for protein delivery [91, 154]. These materials have demonstrated osteoconductivity in numerous animal models, and are used clinically as bone graft substitutes. Synthetic materials include the homo- and copolymers of lactide and glycolide (PLA, PGA, PLGA), polyethylene glycol (PEG), polyketals and poly(propylene) fumarate (PPF), and are attractive because of their well-controlled and reproducible chemical, physical and structural properties [155-158]. Protein delivery systems can also be classified according to the structure and the formulation of the delivery system as three dimensional scaffolds, electrospun nanofiber meshes, micro/nano-particles, hydrogels or composites [148].

Collagen scaffolds with a spongy structure are clinically used for rhBMP-2 delivery. Winn et al. reported that collagen sponges loaded with rhBMP-2 exhibited a continuous release for 2 weeks *in vivo*, with a half life of 3-5 days in a rat ectopic model [159]. However, the long term release was not investigated, and it is likely that the protein is not retained at later time points. This system also results in significant initial burst release, in the range of 40-90% [160]. It is perhaps due to these reasons that large rhBMP-2 doses (3.5 – 12 mg) are required for efficacy in humans. In addition, the risk of an immunogenic reaction to collagen or pathogen transmission to the host cannot be eliminated, and concerns also persist regarding the heterogeneity of the product [161, 162]. Despite these drawbacks, collagen still remains the standard for rhBMP-2 delivery

due to its acceptable delivery performance, its long history of clinical use, and because the risk of adverse reactions is generally considered low.

Ceramic materials are commonly for bone regeneration. Chu and coworkers delivered rhBMP-2 to a rat segmental defect in dicalcium phosphate dehydrate within a composite ceramic/polymer scaffold, and reported that this system was able to restore the mechanical properties of the rat femurs [91]. However, the scaffold density was reduced by less than 10% in 15 weeks of implantation. The typical problems with ceramics are their brittle nature, uncontrolled degradation and lack of macroporosity. Porous ceramic blocks have been fabricated to mimic the structure of trabecular bone [163]. The disadvantage of this system is that due to the high-temperature sintering process, BMPs can only be surface coated after fabrication, thus limiting the protein dose that can be delivered.

Hydrogels are a class of highly hydrated materials that are composed of hydrophilic polymer chains [164]. Though their low mechanical stiffness necessitates the use of fixation devices for fracture stabilization, they can be deployed using minimally invasive procedures, conform to the shape of the defect and be manipulated by cells during tissue regeneration [165]. In addition, they are require mild processing conditions and can be designed for sustained delivery. For these reasons, hydrogels are attractive for the delivery of growth factors for tissue regeneration. Eckardt et al. used a hyaluronic acid-based hydrogel to deliver rhBMP-2 to rabbit tibial osteotomies, and reported substantial bone formation [166]. Tabata and coworkers have demonstrated that the co-delivery of TGF-β and MSCs within gelatin microspheres achieved the closure of rabbit cranial defects [167, 168]. The importance of protein release from hydrogels and their degradation rate was highlighted in a study by Rizzi et al [169]. They reported that the physical linkage of rhBMP-2 to a recombinant protein-poly(ethylene glycol) hydrogel prevented optimal bone healing of murine cranial defects, due to lack of chemotactic signaling and insufficient degradation of the hydrogel matrix.

Alginates are well-characterized polysaccharides isolated from brown algae found in coastal waters. Hydrogels made from alginate have been established as a scaffolding material [105] and a spatiotemporal delivery vehicle for a wide range of proteins [170-172]. This is due to their biocompatibility, low toxicity, relatively low cost, and simple gelation with divalent cations like Ca^{2+} and Mg^{2+} [99]. Alginates can be covalently coupled with adhesion peptides to promote cellular attachment, and their degradation rate can be increased by Gamma-irradiation [173]. These modified alginates have been demonstrated to be better suited for tissue regeneration by allowing faster ingrowth of cells and tissue [105, 174].

In summary, the current clinical delivery systems may require further optimization, and there is a tremendous need for improving protein delivery for tissue regeneration applications [148]. It is also unlikely that one of the above delivery systems will be ideal for all clinical therapies. The optimal design of the delivery system will depend on the protein to be delivered, the tissue and injury to be repaired, and the vasculature and weight bearing requirements.

Guided bone regeneration

Guided bone regeneration refers to the use of membranes to repair bone defects by placing them along the periosteal surface to demarcate the osseous from the non-osseous region. This technique has been used successfully in the dental field to regenerate lost alveolar bone following chronic periodontitis [175-178]. A few groups have investigated the efficacy of this technique for healing diaphyseal bone defects in animal models [92, 179, 180]. Gogolewski and co-workers used polylactide membranes formed into tubes to conform to a 10 mm diaphyseal defect in the radius of rabbits. The membranes were 0.12-0.25 mm thick and had pore sizes that varied from less than 5 μm in microporous membranes to 200 μm in large pore membranes. Based on histologic and radiographic evidence, they concluded that by 8 weeks, the defects had been bridged by

bony tissue when membranes were used, and that microporous membranes had the most intensive bone formation [181, 182]. When they used the technique with larger defects in the sheep model, they observed similar bridging, but required an additional bone graft or vascularized osteoperiosteal flap for effective bone healing. They also made perforations in the membrane to enhance the vascular supply to the defect [183]. Giardino et al. reported that the average thickness of regenerated bone was significantly increased when they used a poly-DL-lactide tubular chamber with MSCs and demineralized bone matrix (DBM) compared to just MSCs and DBM [94]. It is hypothesized that the mechanism by which the membranes heal defects is by protecting the defect from infiltration by soft tissue cells, guiding the osteogenic cells and containing the osteogenic factors within the defect site [182]. Woven bone formation, supported by migration of osteoprogenitor cells from the periosteum and bone marrow, is thought to start at the periphery and proceed inwards within the defect site [92]. Despite the numerous studies on guided bone regeneration, the quantification of bone formation in diaphyseal defects and the evaluation of restoration of limb function remains to be performed [179, 181, 184].

Electrospun Nanofiber Meshes

Nanofiber mesh: an ECM-mimetic scaffold

Numerous biodegradable scaffolds have been designed to function as a temporary matrix for cellular attachment, proliferation and extracellular matrix deposition. By providing a template for tissue regeneration, scaffolds are an essential component of the TE/RM strategy. Scaffolds are typically designed to possess a set of properties that enhances cell survival, signaling, growth and phenotype expression [185]. A major focus of researchers has been to create scaffolds that mimic the ECM. An important component of this strategy is to design structural features on the scaffold that are similar to the ECM. Electrospinning, though a process known for decades, has recently emerged as a

technique to produce scaffolds with fiber diameters ranging from tens of nanometers to as large as 10 μm, thus closely resembling the size scale of ECM components [186-188]. Electrospinning can generate nanofiber meshes with high porosities and large surface area-to-volume ratios, and therefore is an attractive technique for the production of scaffolds. The nanofiber mesh structure allows for greater cellular attachment and enhanced cell spreading. Numerous *in vitro* studies have shown that nanofiber meshes are able to support the attachment, proliferation and metabolism of numerous cells types including osteoblasts, MSCs, endothelial cells, and fibroblasts [189-192]. Xin and coworkers seeded hMSCs on PLGA nanofiber meshes, and separately induced their chondrogenic and osteogenic differentiation [191]. They reported that the cells remained viable on the meshes, and after 2 weeks, the deposited matrix stained for markers of cartilage and bone. However, quantitative analysis of the matrix was missing. In contrast to the numerous *in vitro* publications, there is limited *in vivo* data available on nanofiber meshes. A few studies have explored their use in calvarial defect models *in vivo* [96, 193]. However, their efficacy in guiding long bone regeneration remains to be investigated.

Electrospun meshes are frequently fabricated from synthetic polymers due to their relative ease of processing and ready availability. However, synthetic meshes lack the necessary biofunctionality that is important in the scaffold's interactions with cells. In an attempt to further mimic the ECM, researchers have used natural materials to electrospin nanofiber meshes. These natural materials including collagen (types I-IV), gelatin, fibrinogen, silk, and chitosan [187, 194-198]. Despite the improved bioactivity, nanofiber meshes composed entirely of natural materials have limited strength and may be impractical for many applications. The structural integrity of collagen meshes may be improved by cross linking the collagen [199], but still falls short of synthetic meshes. For this reason, composite meshes containing both synthetic and natural materials may possess an optimum combination of strength and bioactivity. A few studies have

observed enhanced cellular responses on collagen-containing composite meshes [189, 200, 201], but further work needs to be done to understand their efficacy in promoting osteogenic differentiation.

Electrospinning setup

Electrospinning is a relatively simple process, and has been employed for over four decades to produce various industrial products [202-205]. The electrospinning apparatus consists of (a) high voltage power supply, (b) syringe pump, (c) syringe, (d) stainless steel needle, and (e) metal collector plate. The whole setup is enclosed in a plastic chamber to provide electrical shielding. A polymer solution is loaded into a syringe attached with a metallic needle, which is then placed on the syringe pump set to infuse the solution. The positive electrode of the high voltage power supply is connected to the needle. This creates a strong electrostatic field between the polymer solution and the grounded collector plate. When the electrostatic forces exceed the surface tension holding the polymer solution at the needle tip, the polymer solution is ejected as a jet. As the jet moves towards the collector plate, the solvent evaporates and the jet is split into ultra-fine fibers due to charge repulsion. Ultimately, the fibers are collected on the metal plate, with fiber diameters typically in the nanometers to a few micrometers range.

Nanofiber mesh: a 2-D or a 3-D scaffold?

Though electrospun nanofiber meshes have high porosity (usually 70-90%), the pore size is much less than 10 μm [196, 206]. Since this is lower than the size of a typical mammalian cell, cells seeded on a nanofiber mesh remain primarily on the surface of the mesh with minimal penetration into the interior (Figure 2.1). This is distinctly different than what occurs in a typical TE/RM scaffold. Traditional TE/RM scaffolds are 3-D in structure, designed with a pore size of 200-900 μm to encourage cell penetration [65]. The pore size in nanofiber meshes is directly related to and controlled by the fiber

diameter, and therefore cell infiltration can be improved to a certain extent by increasing the fiber diameter [186, 207]. However, some studies have found that larger micrometer-scale fibers hinder cell attachment and spreading [186, 190, 192]. In addition to the limited cell penetration, electrospun nanofiber meshes are also relatively thin. Meshes can be manufactured with a maximum thickness of around a few millimeters, even after many hours of electrospinning [208]. This is much less than the dimensions of large bone defects (2-6 cm). Thus, impaired cellular infiltration and limited thickness are major drawbacks in the use of nanofiber meshes as a 3-D scaffold for regenerating thick tissues like bone. However, the ability to control cellular penetration may be advantageous for regenerating bone via GBR by preventing fibrous tissue infiltration into bone defects [183].

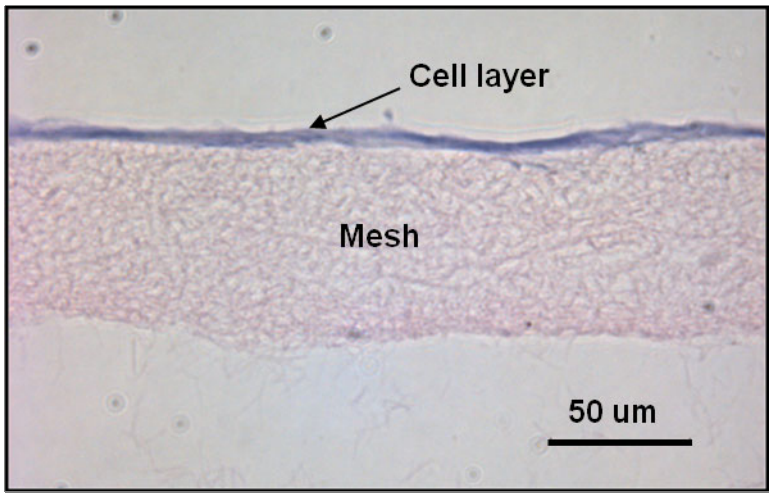

Figure 2.1. Histologic cross section of a cell-seeded electrospun nanofiber mesh. Due to the small pore size, cells seeded on a nanofiber mesh form a cell layer on the mesh surface after 2 weeks. There is no evidence of cell infiltration into the center.

CHAPTER 3

COLONIZATION AND OSTEOGENIC DIFFERENTIATION OF DIFFERENT STEM CELL SOURCES ON ELECTROSPUN NANOFIBER MESHES

Introduction

Bone is one of the few adult tissues with the capacity to regenerate. However, large, unstable, or infected bone defects remain a challenging clinical problem [50]. Tissue engineering strategies that deliver cells, growth factors and genetic material on scaffolds have demonstrated considerable potential in developing bone graft substitutes [64, 65]. Delivery of exogenous cells capable of forming bony tissue may be especially important to repair bone defects in patients with a limited endogenous progenitor cell supply, such as older patients, smokers, or patients with certain diseases [122]. The success of cell-based therapies for bone regeneration has been limited, in part, by the inadequate availability of large quantities of osteogenic cells and an effective cell delivery system.

The identification of a cell source that may be easily harvested, expanded to large numbers, and controllably differentiated may be tremendously beneficial clinically for the reconstruction of damaged tissues. Bone marrow derived mesenchymal stem cells (MSCs) have demonstrated a strong potential for differentiation into bone forming cells, and have been shown to promote repair of critically-sized bone defects in pre-clinical animal studies [125-127]. These cells are well suited for autologous transplantation, making them a feasible cell source for clinical deployment due to the lack of immunogenic issues associated with this transplantation modality. However, MSCs are associated with reduced mineralization capacity in older donors and following expansion to achieve therapeutic cell numbers [128, 130].

Amniotic fluid-derived stem (AFS) cells are c-Kit expressing cells isolated from amniotic fluid that have demonstrated a high self-renewal capacity and the ability to differentiate into a diverse range of cell types, including those from the adipose, muscle, neuronal, cartilage and bone lineages [132, 134, 209, 210]. Recently, our lab has demonstrated that these cells can produce robust mineralization in 3-D constructs *in vitro* and *in vivo* [211, 212]. Importantly, AFS cells have also shown a lack of senescence through 250 population doublings and display an absence of tumorigenicity *in vivo* [132]. However, not much is known of their osteogenic potential compared to MSCs. A critical step towards clinical translation is the quantitative comparison of the proliferation and bone-forming capacity of different cell sources.

The delivery of stem cells to the site of injury, either through systemic introduction or local delivery, is another critical consideration for the success of cell-based therapies. Site-specific delivery has the advantage of being able to deliver large numbers of cells directly to the required area. In tissue-engineering strategies, this typically involves placing cells on a three-dimensional (3-D) scaffold, followed by implantation at the injury site. However, the lack of initial vascularity at the center of a 3-D scaffold limits the transport of nutrients to, and waste products from, the cells. This presents a very harsh environment that makes cell survival extremely difficult [139, 140]. An alternative is to deliver cells to the periphery of the defect via a thin membrane or scaffold. This delivery strategy may enhance cell survival by positioning the cells in close proximity to the surrounding highly vascularized tissues, and thereby providing for nourishment and clearance of waste products.

Electrospinning has recently emerged as a technique to produce polymeric scaffolds for tissue engineering, with fiber diameters ranging from tens of nanometers to as large as 10 μm [186-188]. The nanofiber mesh obtained by this process is a unique scaffold membrane that possesses structural features with a size scale similar to extracellular matrix (ECM) components, high porosity and large surface area to volume

ratios. These properties allow for enhanced cellular attachment and spreading [90, 98]. and therefore nanofiber meshes may serve as an effective delivery vehicle for cells to a defect site *in vivo*. However, it is important to first evaluate their efficacy in supporting cell function and as a cell delivery vehicle *in vitro*. Though a few studies have investigated the osteogenic differentiation of progenitor cells on nanofiber meshes, more thorough analyses are needed to characterize the differentiation and mineralization process, and to quantify mineral deposition [191, 213, 214]. In addition, nanofiber meshes may be utilized as an ECM-mimetic surface for evaluating cell behavior, and therefore serve as an improved *in vitro* cell culture system, compared to flat tissue culture plates [215].

The purpose of this study was to investigate the attachment, colonization and osteogenic differentiation of human MSCs (hMSCs) and human AFS (hAFS) cells on electrospun nanofiber meshes. We demonstrate that electrospun meshes are able to robustly support these functions for both cell types. Compared to tissue culture plastic, there is delayed initial attachment and proliferation, but enhanced mineralization at a later time point. Differences in the kinetics of osteogenic differentiation were observed between hMSCs and hAFS cells. Cell-seeded nanofiber meshes were also effective in colonizing three dimensional scaffolds in an *in vitro* model. These results provide support for the use of the nanofiber mesh as a cell delivery vehicle for the repair of bone defects *in vivo*.

Materials and Methods

Fabrication of nanofiber meshes

A polymer solution was made by dissolving 13% (w/v) poly (ε-caprolactone) (PCL) (Sigma-Aldrich, St. Louis, MO) in a 40:60 volume ratio of dichloromethane (DCM):dimethylformamide (DMF) (Sigma-Aldrich). PCL pellets were added to the

solvent mixture, and gently stirred for 16-24 hours. The polymer solution was loaded in a 3 mL syringe (Becton-Dickinson, Franklin Lakes, NJ), and a 22 gauge blunt stainless steel needle (Jensen Global Inc., Santa Barbara, CA) was attached to the syringe end. The syringe was mounted on a syringe pump (Harvard Apparatus, Holliston, MA), and the pump was set to infuse at a rate of 0.75 mL/hr. A flat, 6×6 inch copper plate (McMaster-Carr, Atlanta, GA) covered with aluminum foil was used to collect the fibers, and placed at a distance of 20 cm from the needle end. Fibers were electrospun for 50 minutes at a voltage of 14 kV, supplied by a high voltage power supply (Gamma High Voltage Research, Ormond Beach, FL), to obtain a thin sheet of nanofiber mesh. To remove any residual solvent, the meshes were placed in a dessicator for at least one day before further use.

Nanofiber mesh morphology

The morphology of the nanofiber meshes was examined using a Scanning Electron Microscope (SEM). A small piece of the dry nanofiber mesh was cut and mounted on a metal stub using double-sided adhesive tape. A thin layer of gold was then deposited on the mesh sample for 80 seconds using a sputter coater (Quorum Technologies, East Granby, CT). The gold-coated sample was then viewed under a Hitachi S-800 Field Emission SEM (Hitachi HTA, Pleasanton, CA) with 10kV accelerating voltage. The diameters of the fibers were quantified by analyzing the SEM images (at 7000× magnification) using a custom MATLAB® (MATLAB® 7.0 R14, The MathWorks Inc., Natick, MA) program. A total of at least 75 distinct fibers were measured from four randomly chosen locations.

Culture of AFS cells and MSCs

Human AFS cells were kindly provided by Dr. Anthony Atala and Dr. Shay Soker at the Wake Forest Institute for Regenerative Medicine (Winston-Salem, NC). The

isolation method and culture protocols have been described previously [132, 134]. Briefly, back-up human amniocentesis cultures were harvested by trypsinization, and subjected to c-kit immunoselection. hAFS cells were subcultured routinely at a dilution of 1:4 to 1:8, and not permitted to expand beyond 70% confluence. The hAFS cells were passaged in αMEM (Minimum Essential Medium Alpha) supplemented with 16% fetal bovine serum (ES Cell-qualified FBS), 100 U/ml penicillin, 100 μg/ml streptomycin, 2 mM L-glutamine (Invitrogen, Carlsbad, CA), 18% Chang B and 2% Chang C (Irvine Scientific, Santa Ana, CA). In all experiments, cells were used at passages 16-17.

Human MSCs derived from the bone marrow were obtained from the Tulane University Center for Gene Therapy (New Orleans, LA) at passage 1. Cells were isolated using bone marrow aspirates from the iliac crest of normal adult donors as previously described [216]. For expansion, these cells were plated at a density of 50 cells/cm^2, and cultured in hMSC growth media. The hMSC growth media consisted of αMEM (Invitrogen) supplemented with 16% FBS (Atlanta Biologicals, Atlanta, GA), 100 U/ml penicillin, 100 μg/ml streptomycin, and 2 mM L-glutamine (Invitrogen). The cells were subcultured once they reached a confluency of ~70%. Passage 2-3 hMSCs were then used for all experiments.

Cell culture on nanofiber fiber meshes

Square 15 mm samples were cut from nanofiber mesh sheets using scissors. Samples were placed in 24-well culture plates, submerged in 200 proof ethanol (Sigma-Aldrich), and sterilized by allowing the ethanol to evaporate overnight. After the samples had dried completely, they were pre-wetted with sterile 70% ethanol for 30 minutes. The 70% ethanol was then aspirated, and sterile dead weights were placed around the samples to prevent them from floating. The mesh samples were next rinsed three times with excess sterile PBS (Mediatech Inc., Manassas, VA). An 800 μL volume of media was placed in each well containing the samples. The control groups received hMSC growth

media, whereas the osteogenic groups were further supplemented with 10 nM dexamethasone, 6 mM β-glycerol phosphate, 50 μg/ml ascorbic acid 2-phosphate and 50 ng/ml L-thyroxine (Sigma-Aldrich). hMSCs and hAFS cells were then seeded onto nanofiber meshes in approximately 200 μL of hMSC media such that the density of cells was 20,000 cells/cm^2. Cells were also cultured in tissue culture treated 24-well plates at the same density for comparison. Media was changed every 3-4 days, and the constructs were cultured for up to 4 weeks.

Cell viability

On days 1, 7, 14 and 28, the viability of the cells in the constructs was assessed using the Live/Dead® staining kit (Molecular Probes, Invitrogen). Harvested constructs were rinsed in PBS and incubated in 4 μM calcein-AM and 4 μM ethidium homodimer-1 for 45 minutes at room temperature. The samples were again rinsed in PBS, and images were obtained on a Zeiss LSM 510 confocal microscope (Carl Zeiss, Thornwood, NY). Green fluorescence of calcein-AM was detected by using a 488-nm Argon ion laser and a band pass 505-550 filter. Red fluorescence of ethidium homodimer-1 was detected by using a 543-nm Helium-Neon laser and a long pass 560 filter.

DNA content

Samples were harvested after 1, 7, 14 and 28 days to evaluate the construct cellularity, which was assessed by determining the DNA content. The cells were first lysed by freeze-thawing the constructs three times in 0.05% Triton X-100 (Sigma-Aldrich) with vigorous vortexing. To freeze the samples, they were placed in dry ice cooled methanol (Sigma-Aldrich) for 5 minutes. Samples were then thawed in a room temperature water bath. The DNA amount in the lysate was quantified using the PicoGreen® dsDNA Quantitation Kit (Molecular Probes, Eugene, OR), and standardized using Lambda DNA solutions of known concentrations. A working solution of the

PicoGreen® reagent was made following the manufacturer's protocol, and incubated with experimental samples in the dark for 5 minutes at room temperature. The fluorescence was measured on a plate reader (HTS 7000, Perkins-Elmer, Waltham, MA) at an excitation of 485-nm and emission of 535-nm. All samples were run in triplicate, and the DNA content was normalized to the culture surface area of the samples.

Alkaline Phosphatase (ALP) activity

To determine the osteogenic differentiation of the cells on nanofiber meshes, the ALP activity assay was performed. In this assay, the release of *p*-nitrophenol from *p*-nitrophenyl phosphate by the ALP enzyme is measured [217]. The same lysate solution that was used to determine DNA content was used for this purpose. The ALP substrate working solution was made by mixing equal parts of 20 mM p-nitrophenyl phosphate, 1.5 M 2-Amino-2-Methyl-1-Propanol (pH 10.25) and 10 mM $MgCl_2$. The experimental samples were mixed with the freshly made substrate working solution, and incubated for 1 hour at 37° C. The reaction was stopped by adding 1N NaOH, and the absorbance was measured at 405 nm on a plate reader (PowerWave XS, Biotek, VT). All samples were run in triplicate and compared to p-nitrophenol standards. The ALP activity was normalized by the incubation time and the amount of DNA obtained from the PicoGreen® assay.

Calcium content

To quantify matrix mineralization, the calcium deposited by cells on nanofiber meshes after 28 days was determined using the Arsenazo III dye [218]. Samples were vortexed with 1 N acetic acid overnight to extract the calcium into solution. The extract was mixed with the Arsenazo III reagent (Diagnostic Chemicals Limited, Oxford, CT), incubated for 30 seconds at room temperature, and the absorbance read at 650 nm on a

plate reader (PowerWave XS, Biotek). The samples were assayed in triplicate and compared to Calcium Chloride ($CaCl_2$) standards.

Calcein staining and quantification

For visualization of the mineral deposited by the cells, the samples were stained using calcein on day 28 [219, 220]. Briefly, a stock solution of 100 μg/ml calcein (Sigma-Aldrich) in PBS (pH 7.4) was added to the media on top of the samples, such that the final concentration of calcein was 10 μg/ml. The samples were incubated in the calcein solution for 4 hours in the incubator. After rinsing twice with PBS and fixing with 10% neutral buffered formalin (EMD Chemicals, Gibbstown, NJ), samples were rinsed with excess of DI water. The fluorescence of the samples was read on a fluorescence plate reader (HTS 7000, Perkins-Elmer) at an excitation of 485-nm and emission of 535-nm. Following this, the same samples were imaged using an inverted microscope (Axio Observer.Z1, Carl Zeiss) and a FITC filter.

Fourier Transform Infrared (FTIR) Spectroscopy

On day 28, constructs were also harvested for analyzing the chemical composition of the mineral deposited on the nanofiber meshes. Samples were dehydrated in 100% ethanol and dried at 50° C overnight. Acellular PCL nanofiber mesh was used as a negative control. After dehydration, the samples were cut into small pieces, mixed with potassium bromide (Sigma-Aldrich), and pressed into pellets using a custom built apparatus. Samples were analyzed with a Nicolet Nexus 470 FTIR spectrometer (Thermo-Nicolet, Madison, MI). Sixty four scans were acquired at 4 cm^{-1} resolution under nitrogen purge.

Cell delivery by nanofiber mesh *in vitro*

The ability of a cell seeded nanofiber mesh to serve as a cell delivery vehicle was studied using an *in vitro* model. AFS cells were seeded on to nanofiber mesh samples

(15×10 mm) at a density of 200,000 cells/cm^2. The cells were allowed to attach to the mesh overnight. On the following day, each cell seeded mesh was wrapped around a cylindrical collagen scaffold (dry dimensions: 4 mm diameter and 9 mm length) aseptically, such that the cells were facing the scaffold (Figure 3.7A). The scaffolds were punched from a fibrous collagen sheet (average pore size 61.7 μm, 93.7% pore volume, Kensey Nash, Exton, PA). The mesh was held in position by placing two interrupted silk sutures through the mesh and scaffold at the two ends of the scaffold. For comparison, we also seeded 300,000 cells throughout collagen scaffolds by pipetting the cell suspension directly in the scaffolds. There was no nanofiber mesh in this control group. The constructs were statically cultured in hAFS cell growth media. After two weeks, the mesh was taken off, following which the mesh and scaffold were stained with the Live/Dead® staining kit (Molecular Probes, Invitrogen) to visualize the cell migration into the scaffold. A confocal microscope (Zeiss LSM 510, Carl Zeiss) was used to take serial images to create three dimensional images.

Data analysis

Results are presented as mean $\pm$ standard error of the mean (SEM). Analysis of variance (ANOVA) was performed on data, with pairwise comparisons done using the Tukey multiple comparison procedure. A p-value < 0.05 was considered significant. Residuals were used for diagnosing the appropriateness of the model by analyzing the constancy of error variance and normality of error terms [221]. Wherever required, remedial measures were taken by transforming the data according to the Box-Cox procedure [222], or by using weighted least squares to make the error variance constant and the error distribution normal [221, 223]. Minitab® 15 (Minitab Inc., State College, PA) was used to perform the statistical analysis.

Results

Morphology of nanofiber meshes

PCL nanofiber meshes were electrospun on a flat collector plate. The mesh formed a circular area of approximately 8 cm diameter. The thickness of the mesh was found to vary with location, with the central areas thicker than the edges. The thin mesh samples from the edges were discarded and not used for cell culture. Fibers appeared to be smooth and uniform, with minimal bead formation (Figure 3.1 A and B). The quantification of the fiber diameter using a custom MATLAB® program demonstrated that the mean fiber diameter was 591 nm with a standard deviation of 199 nm. The fiber diameter histogram revealed that most of the fibers were between 300-900 nm, with the highest frequency occurring in the 500-600 nm range (Figure 3.1 C).

Viability and colonization of hMSCs and hAFS cells over time

hMSCs and hAFS cells were seeded on electrospun nanofiber meshes and tissue culture plates, and cultured in osteogenic media for up to 28 days. The viability of the cells on the meshes was assessed on days 1, 7, 14 and 28 by the Live/Dead® staining kit. The live cells are stained green, whereas the dead cells appear red. At the same time points, DNA from the samples was extracted and quantified to estimate the number of cells on the meshes, as well as in the culture wells. The Live/Dead images (Figure 3.2) illustrate that both cell types attached to the nanofiber meshes by day 1 and were able to spread out by day 7. During days 7-14 the number of cells increased considerably, and by day 28, the cells were confluent on the meshes. The viability of both cell types on the meshes was found to be high, as seen by the extensive green stain, though a few dead cells were detected. No differences were observed in the viability and colonization between the two cell types.

The DNA quantification over the four week culture period was used to compare the colonization kinetics of the two cell types on tissue culture plates and nanofiber meshes, respectively (Figure 3.3). There was significant increase in DNA with time for both cell types, on plates as well as meshes, indicating cellular proliferation. On plates, the number of hAFS cells increased between days 1-7 but did not change significantly after that, suggesting rapid initial proliferation and confluency around day 7 (Figure 3.3 A). On the other hand, hMSCs increased in numbers between both days 1-7 and days 14-28. However, this result is an artifact of hMSC culture on the plates, as the hMSCs were found to lift off the plate after confluence around day 7 to form a pellet, and then repopulate the plate. This pelleting behavior was not seen with the hAFS cells for up to 28 days, though the hAFS cells do ultimately lift off the plate. The hMSC repopulation explains the increase in hMSC cell number between days 14-28 and the differences seen between hMSCs and hAFS cells on days 14 and 28. There were also significantly more hAFS cells than hMSCs on day 1, suggesting a higher initial attachment and/or proliferation rate.

The pelleting phenomenon does not occur on the nanofiber meshes, even at a later time points. There was a significant increase in DNA for both cell types between days 1-7, and an even higher increase between days 7-14, corresponding to the Live/Dead images (Figure 3.3 B). The number of cells did not change significantly after that, suggesting confluency of the cells on the nanofiber meshes. There were no significant differences in the DNA between hMSCs and hAFS cells at any time point.

We also compared the colonization kinetics of hAFS cells on the nanofiber meshes with that on the tissue culture plates (Figure 3.3 C and D). On days 1, there was significantly less DNA on the mesh compared to plates, suggesting that not all cells attach to the nanofibers within the first 24 hours. The same trend was seen on day 7. However, by day 14, there was no significant difference between meshes and plates. On day 28, there was again no significant difference, though the lines crossed over. Although

the hMSCs pellet in the plates and repopulate the culture surface by day 28, the amount of DNA was not significantly different than that on the mesh.

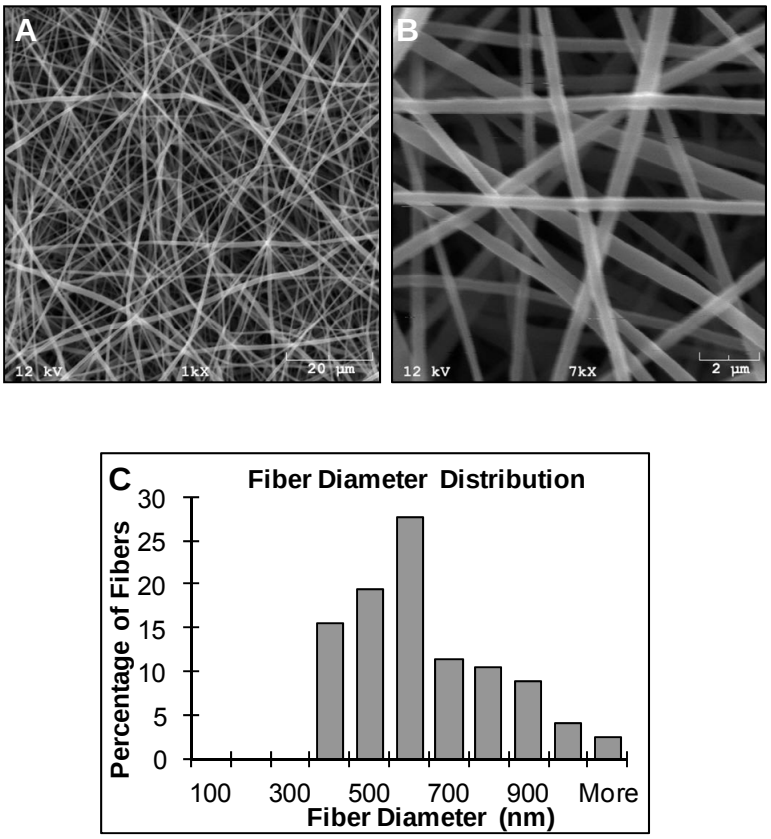

Figure 3.1. Nanofiber mesh morphology. Nanofiber meshes were electrospun from a 13% (w/v) poly (ε-caprolactone) (PCL) solution made in 40:60 dichloromethane (DCM):dimethylformamide (DMF). A Scanning Electron Microscope (SEM) was used to examine the morphology of the nanofibers. (A) SEM image at low (1000X) magnification. (B) SEM image at high (7000X) magnification. (C) The diameter of the fibers was quantified using a custom MATLAB® program and the diameter distribution plotted on a histogram. The mean diameter of the fibers was found to be 591±199 nm.

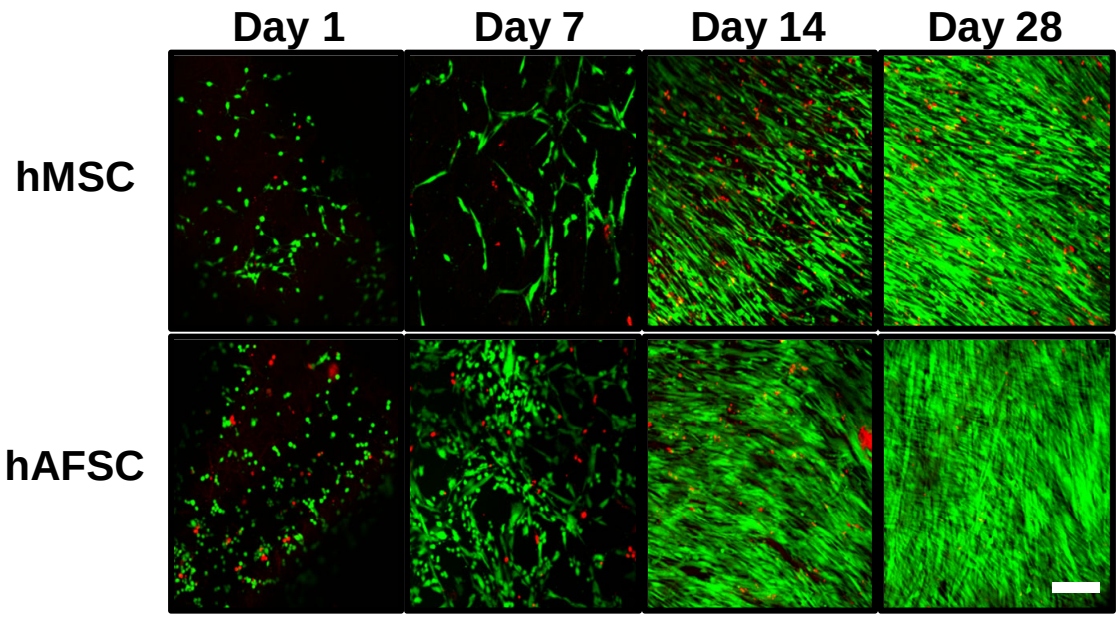

Figure 3.2. Live/dead staining. Human mesenchymal stem cells (hMSCs) and human amniotic fluid stem (hAFS) cells were seeded on nanofiber meshes and cultured in osteogenic media. On days 1, 7, 14 and 28 , the viability of the cells on the meshes was assessed by imaging the constructs with a confocal microscope after staining with the Live/Dead® stain. Live cells: green; dead cells: red. Images were taken at 10X magnification. Scale bar indicates 200 μm and applies to all images. Both cell types were able to attach, proliferate and become confluent on the mesh.

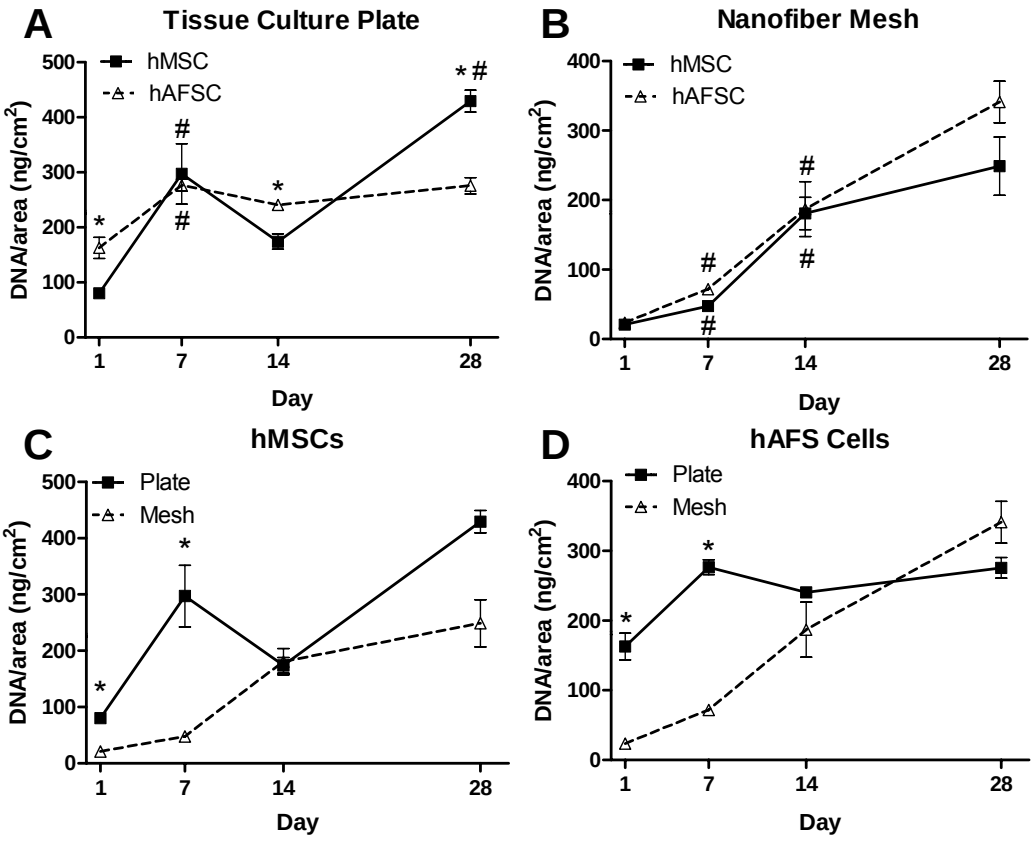

Figure 3.3. DNA content. In order to evaluate sample cellularity, the DNA content was determined after cell lysis using the PicoGreen® reagent. Cells were cultured on (A) tissue culture plates and (B) nanofiber meshes. To compare the cellularity on nanofiber meshes with that on tissue culture plates, the data was plotted again for (C) hMSCs and (D) hAFS cells. DNA increased with time indicating cellular proliferation. Data is presented as mean ± standard error of mean. $p < 0.05$ is considered significantly different. (* - significantly different than the other cell type at same time point; # - significantly different than the previous time point for same cell type).

Osteogenic differentiation of hMSCs and hAFS cells: ALP activity

The osteogenic differentiation of the cells was first investigated by analyzing the ALP activity of the cells (Figure 3.4). ALP is a membrane-bound enzyme that hydrolyzes phosphate esters, which results in inorganic phosphate being available for incorporation into mineral deposits [224]. There was significant increase in the ALP activity of both cell types with time, on plates as well on nanofiber meshes, suggesting osteogenic differentiation. On tissue culture plates, ALP activity peaked at day 7 for MSCs, whereas for AFS cells it increased slowly but continuously up to day 28 (Figure 3.4 A). Interestingly, the maximum ALP activity of the hAFS cells was greater than the hMSC peak. On the nanofiber meshes, hMSCs demonstrated a similar earlier rise in ALP activity, on day 14, compared to day 28 for hAFS cells (Figure 3.4 B). The ALP activity of the hMSCs was significantly greater than that of hAFS cells on all time points other than day 1. The ALP response on meshes is delayed compared to that on the plate, as seen by the later increase in ALP activity. Interestingly, the ALP activity of hMSCs on meshes was sustained longer than plates, with the maximum value on meshes at day 28 greater than that observed on plates at day 7 ($p<0.05$).

Osteogenic differentiation of hMSCs and hAFS cells: matrix mineralization

The osteogenic differentiation of the cells was further investigated by quantifying and staining the calcium deposits and by analyzing the chemical nature of the deposited mineral by FTIR spectroscopy. An ANOVA on the calcium deposited by the cells revealed that both cell type and the culture surface had a significant effect on the calcium levels (Figure 3.5 A). Under osteogenic stimulation, all groups demonstrated increased calcium deposition, compared to growth media, indicating that cells are able to differentiate to an osteoblastic phenotype on the surfaces. Calcium levels in the hMSC growth media groups were negligible. hAFS cells deposited a higher amount of calcium

than hMSCs on both plates and meshes. Also, both cell types deposited more calcium on meshes compared to plates.

FTIR spectroscopy was used to characterize the composition of the mineral that was deposited by the cells on the nanofiber meshes under osteogenic stimulation (Figure 3.5 B). To distinguish the peaks associated with the mineral from the peaks associated with the PCL mesh, an acellular piece of PCL mesh was also scanned [225]. The cellular samples displayed amide I/II peaks at 1655 and 1550 cm^{-1}, a carbonate peak at 870 cm^{-1}, and a doublet split phosphate peak at 560 and 605 cm^{-1}, which were not seen in the acellular mesh. There was also a peak at 1050 cm^{-1} in the cellular samples, but it overlapped with a PCL mesh peak. These peaks are the signature of a carbonate-containing, poorly crystalline hydroxyapatite, the form of mineral that is found in native bone. This suggests that both hMSCs and hAFS cells deposited mineral that possessed the characteristic bands of physiological mineral.

Samples were stained with calcein to visualize the presence of calcium on the nanofiber meshes. The calcein staining demonstrated the presence of extensive calcium-containing mineral nodules, which were uniformly distributed on the meshes, as seen by the green fluorescence (Figure 3.6 A). This was the case in both the hMSC and hAFS cell osteogenic groups, whereas the growth media groups stained minimally. Quantification of the fluorescence revealed that more mineral was deposited by the hAFS cells compared to the hMSCs (Figure 3.6 B), thus supporting the calcium data.

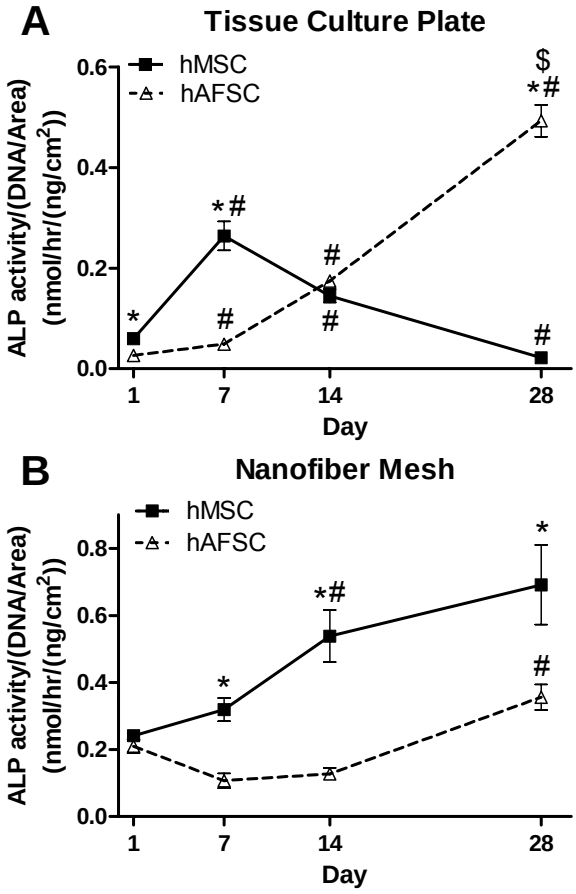

Figure 3.4. ALP activity. The osteogenic differentiation of the cells was evaluated by measuring the alkaline phosphatase (ALP) activity of cell lysates on (A) tissues culture plates and (B) nanofiber meshes. ALP activity increased for both cell types with time, suggesting osteogenic differentiation. $p < 0.05$ is considered significantly different. (* - significantly different than the other cell type at same time point; # - significantly different than a previous time point for same cell type; $ - significantly different than hMSC peak on plate at day 7).

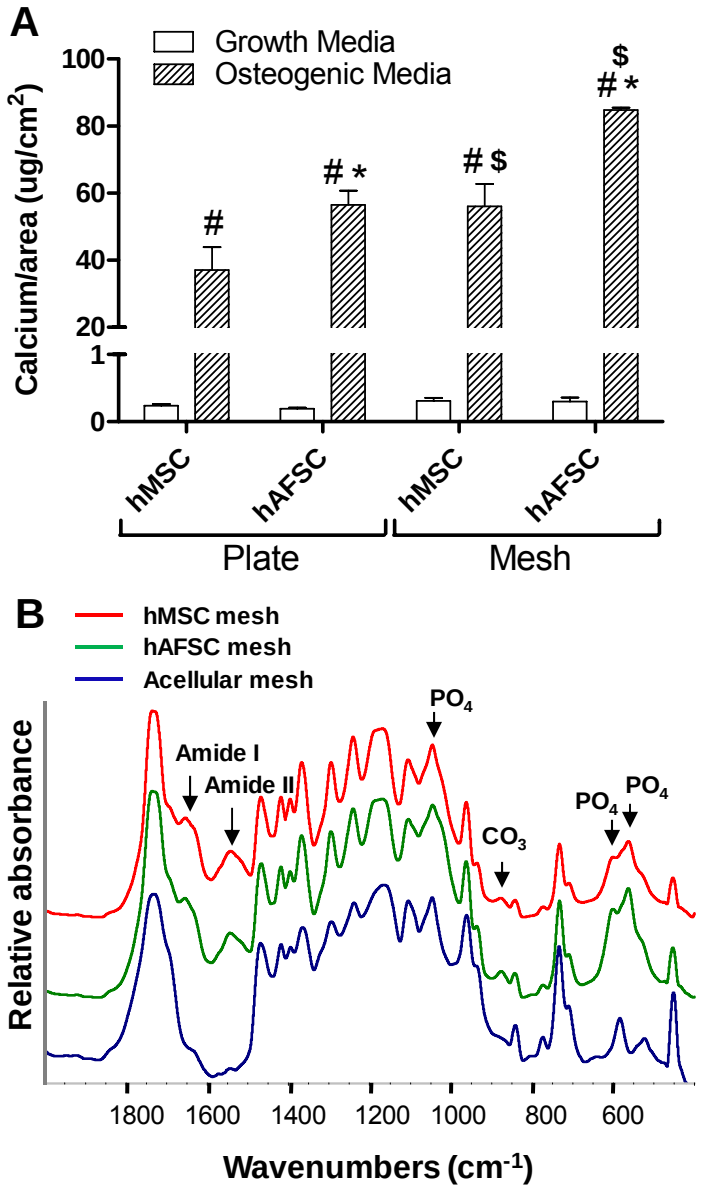

Figure 3.5. Calcium quantification and FTIR analysis. (A) The mineralization of the constructs was assessed by measuring the calcium deposited by cells. Both cell types deposited calcium in osteogenic media, indicating an osteoblast phenotype. $p < 0.05$ is considered significantly different. (# - significantly different than growth media; * - significantly different than other cell type on same surface; $ - significantly different than plate with same cell type). (B) The chemical composition of the mineral was analyzed by Fourier transform infrared (FTIR) spectroscopy. The annotated peaks are the signature of a carbonate-containing, poorly crystalline hydroxyapatite, indicative of physiologic mineral. The remaining peaks are due to the PCL nanofiber mesh, as seen in the acellular mesh.

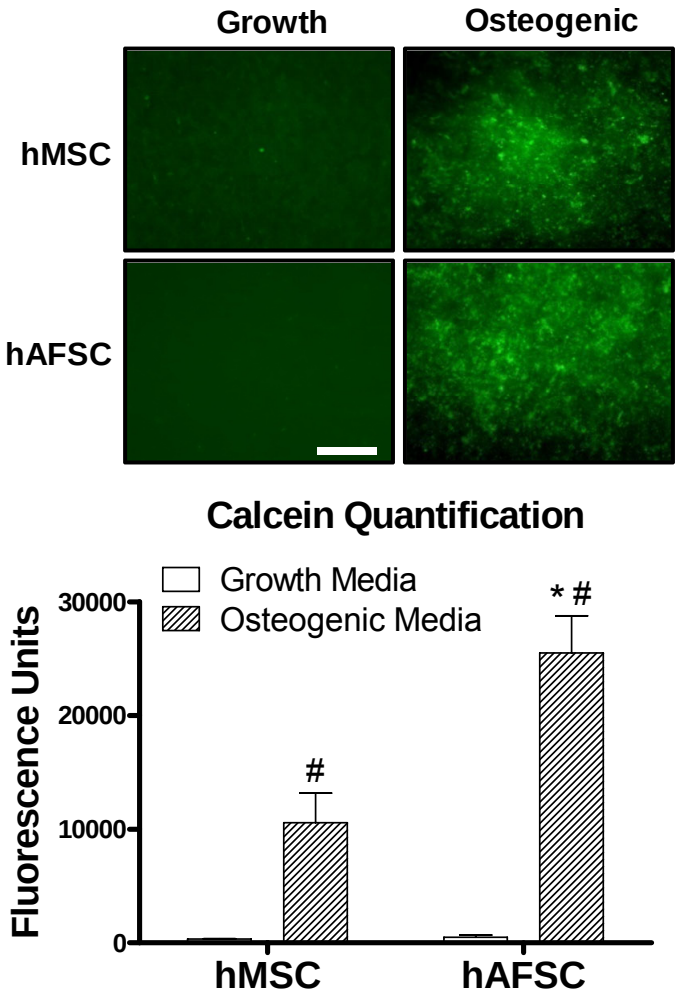

Figure 3.6. Calcein staining. Constructs were stained with calcein to visualize the presence of the mineral deposits. (A) The osteogenic samples stained with calcein, illustrating that cells had deposited mineral uniformly on the nanofiber meshes. Images were taken at 10X magnification. Scale bar indicates 200 μm and applies to all images. (B) The calcein staining was quantified by measuring the fluorescence using a plate reader. The data revealed greater mineralization by AFS cells. $p < 0.05$ is considered significantly different. (* - significantly greater than MSC osteogenic media; # - significantly greater than growth media with same cell type).

Nanofiber mesh as a cell delivery vehicle

As a preliminary evaluation of the nanofiber mesh for cell delivery, AFS cells were seeded on nanofiber meshes and wrapped around cylindrical collagen scaffolds in vitro. The constructs were cultured for two weeks and then stained with the Live/Dead® staining kit. In the cell-seeded scaffold, we observed that more cells were present at the periphery of the scaffold, even though cells were seeded throughout (Figure 3.7 A). We also detected a large number of dead cells in the interior of the scaffold. When the cell-seeded mesh was wrapped around a collagen scaffold, we found that numerous cells had migrated off the mesh onto the collagen scaffold and had high viability (Figure 3.7 C and D). The majority of cells were located close to the peripheral surface. Interestingly, we noted that the top surface was completely covered with cells (Figure 3.7 D). This implies that the cells were able to migrate at least 2 mm from the edge, where the mesh was present, to the center of the top surface. A few cells were also seen in the interior of the scaffold, more than 500 μm away from the peripheral surface (Figure 3.7 D). The mesh was completely confluent with cells indicating that only a subset of cells migrates from the mesh onto the scaffold (Figure 3.7 E).

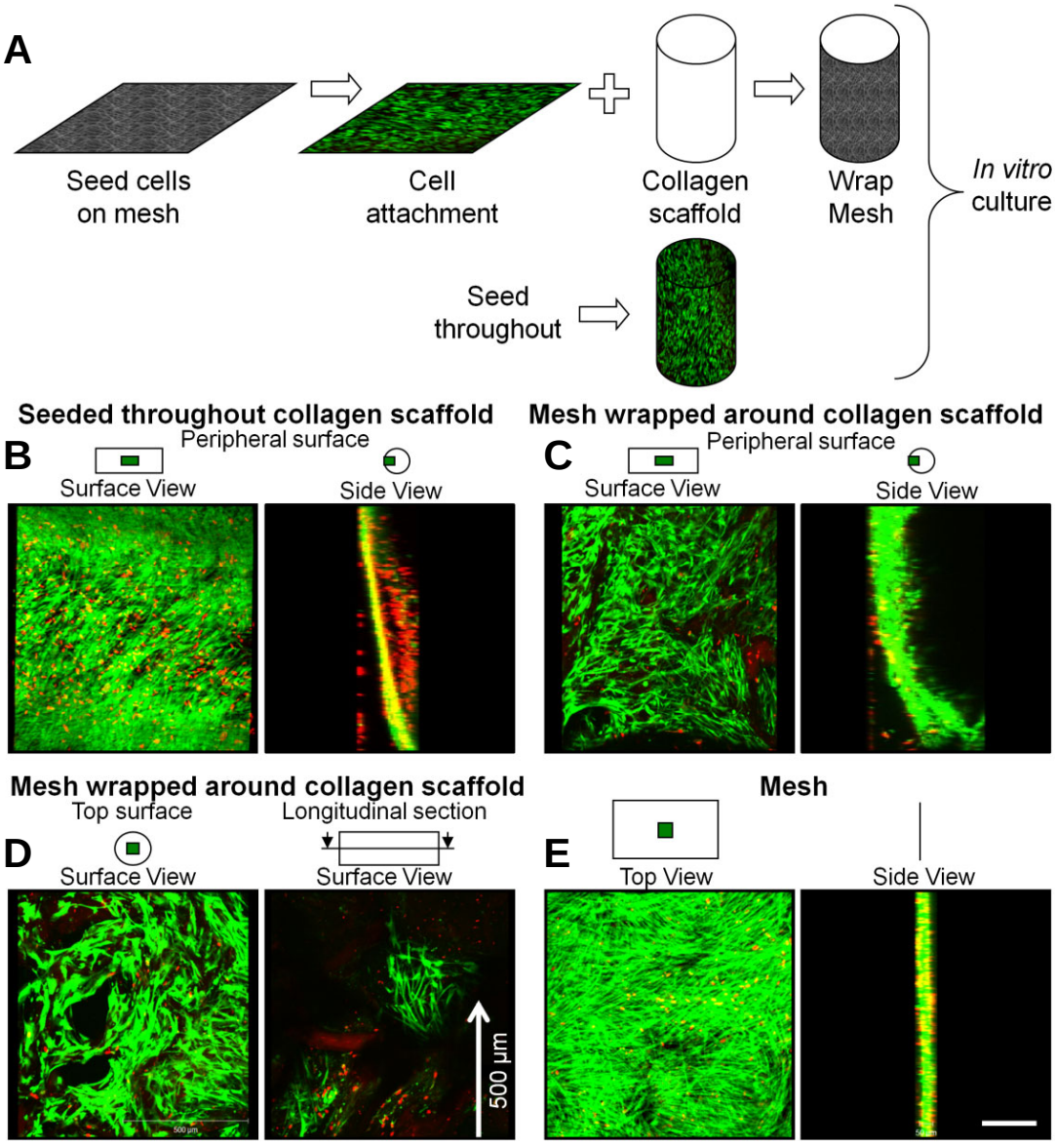

Figure 3.7. Cell-seeded nanofiber meshes for in vitro delivery. (A) To investigate the use of nanofiber meshes for cell delivery, AFS cells were seeded on nanofiber meshes and wrapped around a 3-D collagen scaffold for 2 weeks in vitro. For comparison cells were seeded throughout the scaffold. (B) - (E) Three-dimensional confocal images of the live/dead stained scaffold and mesh. The projections of the 3-D images are shown. The surface and top views are views of the 3-D image looking from the top. The side view is the view of the 3-D image looking from the side. The green box indicates the area and view being analyzed. (B) The collagen scaffold with cells seeded throughout had more cells on the exterior with numerous dead cells in the interior. (C) When a cell-seeded mesh was wrapped around the scaffold, cells migrated on to the peripheral surface of the scaffold and displayed high viability. (D) Top and cross-sectional surfaces of scaffold wrapped with cell-seeded mesh. Cells also colonized the top surface of the scaffold and migrated more than 500 µm into the scaffold from the mesh. (E) The seeded mesh was confluent with cells. Images were taken at 10X magnification. Scale bar indicates 200 µm and applies to all images.

Discussion

In this study, we investigated the function of two kinds of stem cells, hMSCs and hAFS cells, on electrospun nanofiber meshes. Both cell types were able to attach, colonize and undergo robust osteogenic differentiation on the meshes. This indicates that the nanofiber mesh is a scaffold membrane capable of supporting vital osteoprogenitor and osteoblast functions. Other groups have also reported the ability of nanofiber meshes to promote differentiation of osteoblasts [192, 226] and MSCs [213, 227]; however a quantitative and more thorough analysis of the matrix mineralization has been missing. We utilized a sensitive calcium assay based on the Arsenazo III dye to quantify the extent of matrix mineralization [218, 228]. The mineral deposited on the nanofiber meshes was confirmed to be biological in nature by FTIR spectroscopy, indicating that the process was cell-mediated. Finally, we used calcein staining to visualize and semi-quantify the mineral deposits on the mesh. Another advantage of the calcein stain is that it can be used for continuous monitoring of the *in vitro* matrix mineralization process [219, 220].

Although acellular approaches to bone reconstruction using scaffolds and osteogenic growth factors have shown moderate clinical success, the delivery of osteogenic cells may be required for patients with a reduced local supply of responsive osteoprogenitor cells. For successful clinical translation of cell based bone defect repair, a cell source needs to be identified that is readily available, propagated easily, has high osteogenic potential, and will be accepted by the recipient immune system. Both hMSCs and hAFS cells possess a number of these characteristics. MSCs have been studied extensively, especially for bone regeneration, and preclinical studies have shown their ability to repair bone defects *in vivo* [125, 126]. A number of human clinical trials have shown variable, but encouraging results of hMSC therapy, including the treatment of graft-versus-host disease, myocardial infarction, osteogenesis imperfecta and large bone defects [229, 230]. However, hMSCs are known to progressively lose their stem cell properties during expansion, limiting the total number of cells available for therapy, and

limited viability following transplantation remains a significant challenge [231]. One of the objectives of this study was to compare the osteogenic capacity of this widely-used adult stem cell with a more novel fetal stem cell source, the hAFS cells. AFS cells have been demonstrated to be capable of extensive self-renewal, and therefore can be expanded to large numbers and still maintain their multipotency [132, 134, 209, 210].

The colonization kinetics of hMSCs and hAFS cells on nanofiber meshes was found to be similar, suggesting comparable proliferation rates when seeded at a high density of 20,000 cells/cm^2. On tissue culture plates there were more hMSCs than hAFS cells on day 28, but this was due to the pelleting and recolonization by the hMSCs. hAFS cells demonstrated a later rise in ALP activity than the hMSCs on both plates and meshes, perhaps due to their primitive nature. ALP is a membrane-bound enzyme that plays an important role in matrix mineralization [224]. ALP activity is one of the earliest markers of osteogenic differentiation and rises as the osteoprogenitors commit to the osteoblast lineage. It peaks in the matrix maturation phase and decreases as mineralization progresses [232, 233]. However, ALP is expressed by other differentiated cells as well [234, 235], and therefore it is important to simultaneously analyze other osteogenic measures, such as matrix mineralization. At four weeks, hAFS cells deposited significantly more mineral than hMSCs on both plates and meshes, as demonstrated by calcium quantification and calcein staining. Thus we observed that, while the rise in ALP activity of the hAFS cells occurs later than in hMSCs, the hAFS cells mineralize more robustly after 4 weeks. This indicates that the kinetics of ALP activity and matrix mineralization are differentially regulated for these two different cell types. Our results demonstrate that hAFS cells have high osteogenic potential, even at the late passage numbers we have used. In addition, unlike human embryonic stem cells (hESCs), hAFS cells have shown an absence of tumor formation *in vivo* [132]. This suggests that the hAFS cells may be a feasible cell source for the repair of bone defects. They may be especially useful in the case of patients whose cells are not amenable for autologous

transplantation due to disease or advanced age. Another advantage of the AFS cells is that they are suitable for convenient off-the-shelf allogeneic cell delivery, as long as the major histocompatibility complex of donor and recipient are matched. This would reduce the time and cost of delivering the cell therapy and may result in improved clinical acceptance.

Woo and coworkers have recently reported that a nanofibrous scaffold made by a modified solvent casting method resulted in improved expression of osteoblast phenotype versus a solid-walled scaffold [236]. We compared cell function on the nanofiber meshes with that on tissue culture plastic. Compared to tissue culture plastic, there is delayed initial attachment and proliferation on the meshes. However by two weeks, the cells on the meshes catch up with those on the plates and there is no significant difference between the groups. The cells, especially the hMSCs, did not lift off the nanofiber mesh surface, as was seen on plates. This difference in cell attachment could to due to changes in cell adherence, material and topographic properties or ECM deposited on the nanofiber mesh surface. Despite the initial lag in colonization on meshes compared to that on plates, we observed enhanced mineralization on meshes by both the cell types at four weeks. This suggests that the ECM-mimetic morphology of the nanofibers provides an environment conducive for matrix maturation. In a recent paper, Smith et al. demonstrated that the use of nanofibers resulted in a greater degree of embryonic stem cell differentiation, compared to films and tissue culture plates [237]. This study also provides support for the use of nanofiber meshes as an improved *in vitro* cell culture model surface that better recapitulates the *in vivo* environment of cells.

Cell survival following delivery is a critical issue in the development of cell-based strategies, especially for thick tissues such as bone. The lack of initial vascularity in bone defects limits the transport of nutrients to and waste products from the center of the defect. Therefore, if cells are seeded throughout a three dimensional scaffold and placed at the defect site, cells located at the center of the scaffold may not survive [137-140].

Delivery of cells on the periphery of bone defects via a tissue engineered periosteum may be an effective approach to enhance cell survival by the presence of a neighboring vasculature. With time, as a continuous vasculature is established at the center, the cells may migrate towards the center due to an improved transport environment. Recently Zhang reported that engraftment of bone morphogenetic protein-2 (BMP-2) producing BMSCs using gelfoam wrapped around nonvital allografts improved allograft incorporation and repair [141]. Our results indicate the electrospun nanofiber mesh possesses characteristics suitable for supporting cell function. In addition its thickness can be controlled to obtain a membrane suitable for creating a tissue engineered periosteum. To begin preliminary investigations into cell delivery, we asked the question: will cells migrate off the mesh and populate a three dimensional scaffold *in vitro*? We observed that the cells migrated off the mesh and colonized the scaffold within two weeks, traveling as far as 2 mm. In addition to the migration, part of the colonization is probably due to cell proliferation. Interestingly, we noticed better viability of the cells in the scaffold when they were delivered on the mesh compared to when they were seeded uniformly in the scaffolds. These results suggest that a cell-seeded nanofiber mesh may be an effective method to deliver cells to bone defects and maintain high viability. Future work will determine whether these effects are also observed *in vivo*.

In conclusion, we demonstrated that two types of stem cells, hMSCs and hAFS cells, are able to attach, colonize and undergo robust osteogenic differentiation on electrospun nanofiber meshes. hAFS cells displayed a delayed ALP increase, but deposited significantly more mineral compared to hMSCs. Cell-seeded nanofiber meshes were effective in colonizing three dimensional scaffolds in an *in vitro* model. These results indicate that the electrospun nanofiber mesh supports osteoprogenitor cell function and may be useful as a medium for cell delivery for the repair of bone defects *in vivo*. In addition, this study provides support for the use of nanofiber meshes as a model surface for cell culture experiments.

CHAPTER 4

NANOFIBER ORIENTATION AND SURFACE FUNCTIONALIZATION MODULATE HUMAN MSC INFILTRATION AND OSTEOGENIC DIFFERENTIATION

Introduction

Biomaterial-based implants offer a robust therapeutic strategy to improve tissue regeneration and construct integration [238]. Acellular approaches for tissue regeneration, in which the implanted biomaterial recruits endogenous cells for repair, are more feasible than cell-based therapies for deployment in clinical practice [239-242]. This is due to the technical challenges of cell delivery and survival, and the commercial difficulties associated with the manufacturing and storage of cells and obtaining regulatory approval. For purely biomaterial-based therapies to be effective, the biomaterial is usually required to function as both a scaffold and a biologically active agent to provide specific molecular signals for regulating cellular response [115, 165]. The rational design of the material structure and composition is therefore essential for implant success.

Electrospun nanofiber meshes are a unique type of scaffold with structural features that, at least by scale, resemble the extracellular matrix (ECM). In addition, they exhibit large surface area and high porosity, making them suitable as a scaffold for guiding tissue regeneration by host cells [98, 191, 214, 243]. For example, in the case of a large diaphyseal bone defect, the nanofiber mesh may be able to provide cues for progenitor cells from the periosteum and marrow space to migrate into the defect region and deposit mineralized matrix. In a previous study, we demonstrated that nanofiber meshes made from a synthetic polymer are able to support the attachment, colonization and osteogenic differentiation of progenitor cells (Chapter 3). Synthetic polymers,

however, lack biological ligands, and are not capable of directing intracellular signaling and response. Nanofiber meshes have also been fabricated from natural materials like collagen and fibrinogen [187, 195, 197], but these are limited by poor mechanical strength and handling characteristics for *in vivo* applications [199]. Approaches that incorporate bioactive molecules within a synthetic polymer backbone may provide an optimal combination of biological activity and mechanical integrity.

Tremendous advances have been made in imparting biofunctionality to synthetic materials by coating them with ECM components. These biomimetic material surfaces present adhesion motifs to engage the cell signal transduction machinery for directing cellular response and tissue repair [115, 116]. Though adhesive proteins such as type I collagen, fibronectin and laminin have been immobilized on material surfaces, these approaches are limited by protein purification and processing issues, and a potential host immunogenic response [108-111]. In addition, the multiple adhesion domains in a full-length protein may trigger conflicting intracellular signals, leading to suboptimal tissue repair. Therefore, there is a great need to develop peptides that mimic specific domains of natural proteins. These ECM-mimetic peptides can be synthesized and purified with relative ease, and furthermore, can be designed to trigger a specific cellular response [244-248]. One such peptide that has been recently investigated is a triple-helical, collagen-mimetic oligopeptide containing the glycine-phenylalanine-hydroxyproline-glycine-glutamate-arginine (GFOGER) domain from residues 502-507 of the α_1(I) chain of type I collagen [249, 250]. It has been shown that the interaction of this adhesion motif with $\alpha_2\beta_1$ integrin mediates osteoblast adhesion, differentiation and matrix mineralization [117, 118]. This has been exploited to enhance the adhesion and osteogenic differentiation of progenitor cells and improve implant integration, by coating surfaces with the GFOGER peptide [120, 121, 251]. This technique utilizes simple adsorption of the GFOGER peptide on implant surfaces in physiologic conditions, which may be advantageous for clinical translation.

Another set of guidance strategies consists of topographical cues to influence cellular responses. It is now accepted that surface morphology, including roughness and texture, modulates cellular response. For instance, titanium implants with rough microtopographies reduced cell number, increased differentiation and enhanced implant integration [252-255]. The electrospinning process can be easily adapted to obtain fibrous matrices with varying structure. Fiber alignment, especially, has generated significant interest due to the fact that a number of native and regenerating tissues display an ordered architecture. Studies have shown that alignment of fibers along a particular direction affects cellular attachment and morphology as well as matrix deposition [208, 256, 257]. Neurites grown on aligned nanofibers display contact guidance and improved migration [258, 259]. However, the effect of fiber alignment on human MSCs (hMSCs) function needs to be investigated. In addition, the combined effect of nanofiber mesh orientation and surface composition has not been studied extensively.

The purpose of this study was to investigate the effect of nanofiber functionalization and orientation on hMSC function, in order to identify conditions that best support bridging of bone defects by osteoprogenitor cells. Nanofiber meshes were functionalized with the GFOGER peptide to improve cell adhesion and osteogenic differentiation. An oriented topography was obtained by electrospinning aligned nanofibers in order to enhance cellular migration. We developed an *in vitro* model to examine hMSC infiltration on top of nanofiber meshes, and isolated the contribution of cell proliferation versus migration. The individual and combined effects of nanofiber functionalization and orientation on hMSC function were investigated. We hypothesized that functionalizing nanofiber surfaces with the GFOGER peptide and aligning nanofiber orientation will modulate cellular behavior *in vitro*. In addition, we assessed the efficacy of GFOGER coating to improve nanofiber mesh based repair of segmental bone defects *in vivo*.

Materials and Methods

Electrospinning and nanofiber mesh characterization

Nanofiber meshes were made by electrospinning, and characterized as described elsewhere (Chapters 3 and 5). Briefly, a 12% (w/v) solution of poly (ε-caprolactone) (PCL) was made in a 90:10 volume ratio of hexafluoro-2-propanol (HFP):dimethylformamide (DMF) (Sigma-Aldrich, St. Louis, MO). A 3 mL syringe (Becton-Dickinson, Franklin Lakes, NJ) was filled with the PCL solution and fitted with a 22 gauge blunt-end needle (Jensen Global Inc., Santa Barbara, CA). The syringe was placed on a syringe pump (Harvard Apparatus, Holliston, MA), which was adjusted for a flow rate of 0.75 mL/hr. To create a nanofiber mesh with random fiber alignment (random nanofiber mesh), a flat copper plate was placed at a distance of 20-23 cm from the needle tip. To obtain meshes with fibers aligned along the same direction (aligned nanofiber mesh), they were collected on a mandrel rotating at ~2500 rpm and placed 8-10 cm from the need tip. The syringe needle was attached to the positive end of a high voltage power supply (Gamma High Voltage Research, Ormond Beach, FL), and the collector was grounded to create the electrostatic field required for electrospinning. After applying a voltage of 13-20 kV, the polymer solution was ejected from the needle towards the collector and deposited as nano-scaled fibers. The fibers were collected for 45-60 minutes to obtain meshes with sufficient thickness for cell culture experiments.

The nanofiber meshes were sputter coated with gold (Quorum Technologies, East Granby, CT) and their morphology visualized by Scanning Electron Microscopy (SEM; Hitachi HTA, Pleasanton, CA). A custom MATLAB® (The MathWorks Inc., Natick, MA) program was used to calculate the individual fiber diameter from the SEM images. The alignment of the fibers in aligned nanofiber meshes was quantified by measuring fiber angle relative to the direction of rotation, using the Image-Pro software (Media

Cybernetics, Inc., Bethesda, MD). In the case of random nanofiber meshes, the angles were measured with respect to an arbitrarily set line.

GFOGER peptide preparation and nanofiber surface coating

The peptide, GGYGGGPC$(GPP)_5$GFOGER$(GPP)_5$GPC, was synthesized by the Emory University Microchemical Facility (Atlanta, GA) as described previously [251]. This peptide contains the GFOGER motif, where O refers to hydroxyproline. The purified peptide was lyophilized as a trifluoroacetic acid (TFA) salt. The peptide was reconstituted at a concentration of 10 mg/mL in a 0.1% TFA solution containing 0.01% sodium azide (NaN_3). The stock solution was diluted to 50 μg/mL in phosphate-buffered saline (PBS, Mediatech Inc., Manassas, VA). Nanofiber mesh samples were sterilized by ethanol evaporation, wetted with 70% ethanol and rinsed with excess PBS. The samples were then passively adsorbed with GFOGER by submerging them in the dilute GFOGER solution for 2 hours at room temperature or overnight at 4°C. For comparison, samples were also coated with a 50 μg/mL purified rat type I collagen (Trevigen Inc., Gaithersburg, MD) solution or left uncoated in PBS. After rinsing again with PBS to remove any unbound peptide, the samples were ready for analysis or cell seeding.

Analysis of GFOGER surface coating

The GFOGER adsorbed on the surface of the nanofibers was visualized and quantified using a biotinylated version of the GFOGER peptide. Biotin was conjugated to the carboxyl end of the peptide using the EZ-Link® Amine-PEG_3-Biotin kit (Pierce Biotechnology), and the unreacted biotin was removed by dialysis. To visualize the presence of the peptide on the nanofiber surface, the GFOGER coated nanofiber mesh samples were incubated with 10 μg/mL fluorescein conjugated NeutrAvidin® (Molecular Probes, Eugene, OR) for 30 minutes at room temperature in the dark. After rinsing with excess PBS, images were taken on an inverted fluorescence microscope (Axio

Observer.Z1, Carl Zeiss, Thornwood, NY) using a FITC filter. The saturation of the surface by GFOGER was investigated by incubating meshes with varying GFOGER concentrations of 0-50 μg/mL. To quantify the amount of the biotinylated GFOGER peptide adsorbed on the nanofiber surface, an ELISA was performed using an anti-biotin antibody. Non-specific adsorption of the antibody was first blocked by immersing the nanofiber meshes in 0.25% heat denatured serum albumin with 0.0005% Tween-20, 1 mM EDTA, and 0.025% NaN_3 in PBS for 1 hour at 37°C. The meshes were then incubated with an anti-biotin antibody (diluted 1:2000) conjugated to alkaline phosphatase (clone BN-34, Sigma-Aldrich) for 1 hour at 37°C. An alkaline phosphatase substrate, 4-methylumbelliferyl phosphate, was used at a concentration of 60 μg/mL in diethanolamine buffer (pH 9.5) to measure the amount of bound antibody. After incubating the meshes with the substrate solution for 1 hour at 37°C, the fluorescence was read on a plate reader (HTS 7000, Perkins-Elmer, Waltham, MA) at an excitation of 360 nm and emission of 465 nm.

Human mesenchymal stem cell (hMSC) culture

The Center of Gene Therapy at Tulane University kindly provided the hMSCs. The isolation of the cells has been described previously by Sekiya and co-workers [216]. Briefly, bone marrow aspirates were taken from the iliac crest of normal adult donors, the nucleated cells were isolated with a density gradient and only the cells that adhered to the plate after 24 hours were cultured further. Passage 1 cells frozen in 1 mL aliquots were shipped us. To expand a culture, the cells were thawed and plated at a density of 50 cells/cm^2 in αMEM (Invitrogen), supplemented with 16% FBS (Atlanta Biologicals, Atlanta, GA), 100 U/ml penicillin, 100 μg/ml streptomycin, and 2 mM L-glutamine (Invitrogen). This is termed the hMSC growth media. After the cells reached a confluency of ~70%, they were harvested with 0.25% trypsin–EDTA (Invitrogen),

counted, and either expanded again or seeded on nanofiber meshes. Passage 2-3 hMSCs were used in all experiments.

Investigating cell infiltration on nanofiber meshes in an in vitro model

Rectangular samples (8 mm × 12 mm) were cut from random and aligned nanofiber mesh sheets, sterilized and coated with GFOGER or collagen, or left uncoated in 24-well tissue culture plates, as mentioned above. A 0.9 mm wide sterile stainless steel strip was then placed on the nanofiber mesh to create a region without cells (Figure 4.1). For aligned nanofiber meshes, the strip was placed perpendicular to the fiber orientation. Samples were submerged in 800 μL of hMSC growth media, after placement of a dead weight on the edges to prevent them from floating. hMSCs were then seeded on the nanofiber mesh samples at a density of 40,000 cells/cm^2 in 200 μL of hMSC growth media. After 24 hours, the strip was removed, and the cell infiltration into the gap was observed at various time points.

Cell infiltration was analyzed by staining the nuclei with 4',6-diamidino-2-phenylindole (DAPI, Molecular Probes). Some samples were, in addition, stained with rhodamine phalloidin (Molecular Probes) to visualize the cell alignment. After samples were taken down, they were rinsed with PBS and fixed with 4% formaldehyde for 10 minutes. The samples were then incubated in 0.05% Triton-X (Sigma-Aldrich) for 5 minutes, rinsed in PBS and incubated in 5 units/mL rhodamine phalloidin for 20 minutes. After a PBS rinse step, the samples were incubated in 5 μg/mL DAPI for 5 minutes. Samples were finally washed in excess PBS to remove any unbound dye, and images were taken on an inverted fluorescence microscope (Carl Zeiss). The DAPI images were further processed using ImageJ (U. S. National Institutes of Health, Bethesda, MD) to count the cell nuclei, and thereby quantify cell number. Three fields of view along the gap were analyzed for each sample, and the mean cell number per field is presented,

along with the standard error of the mean. To investigate the number of cells attached on day 0, four locations outside the gap were analyzed.

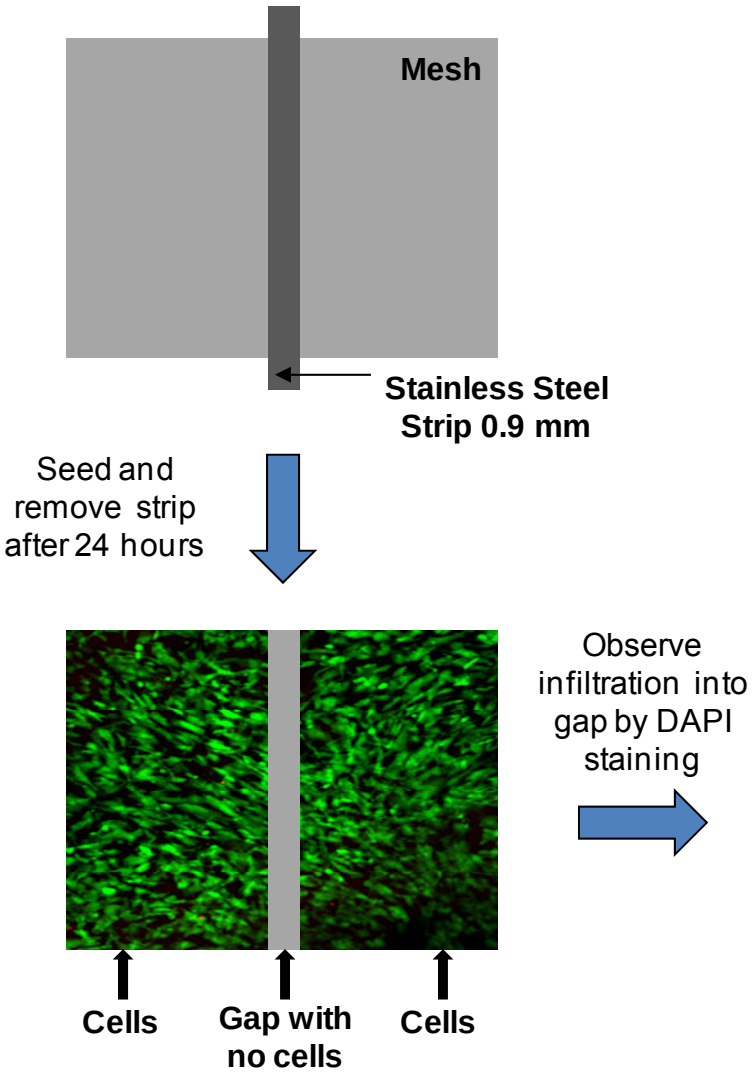

Figure 4.1. Schematic of cell infiltration model. A stainless steel strip is placed on the nanofiber mesh sample before seeding to create a cell-free region. After 24 hours, the strip is removed and cell infiltration into the gap is observed by fluorescence microscopy.

Role of cell proliferation in the cell infiltration model

To investigate whether cell proliferation influences the infiltration of cells on nanofiber meshes, mitomycin C was used to block proliferation. Mitomycin C, which is a known inhibitor of cell proliferation, cross links the strands of DNA, thereby inhibiting DNA replication [260, 261]. The effect of mitomycin C on hMSC proliferation was first studied on tissue culture plates (Figure 4.7 A). hMSCs were plated at a density of 20,000 cells/cm^2, and after 24 hours, they were incubated with 10 μg/mL mitomycin C for 60 minutes. Control samples remained in culture media. Cell proliferation was assessed using 5-bromo-2'-deoxyuridine (BrdU) labeling, according to the manufacturer's instructions (FLUOS, Roche Diagnostics, Mannheim, Germany). Forty eight hours after cell seeding, the cells were incubated in hMSC growth media containing 10 μM BrdU for 24 hours in the incubator. Cells were fixed with an ethanol based fixative for 45 minutes, and denatured with 4 M HCl for 20 minutes to allow for antibody access. After neutralizing the pH with PBS, the cells were incubated with a monoclonal anti-BrdU-antibody conjugated with fluorescein for 45 minutes at 37°C. The cells were finally stained with DAPI for the total number of cells and analyzed using fluorescence microscopy, as mentioned above. Nine fields were examined in a 3×3 grid pattern, and the number of BrdU positive cells along with the DAPI stained cells were counted. Data are presented as the BrdU and DAPI cell counts, as well as the proportion of BrdU positive cells.

The effect of mitomycin C was next studied in the cell infiltration model on nanofiber meshes (Figure 4.8 A). Cells were seeded on rectangular nanofiber mesh samples at a density of 40,000 cells/cm^2, as above. Twenty four hours post seeding, mitomycin C was added to the media at a final concentration of 10 μg/mL, and incubated for 60 minutes. The media was slowly aspirated, fresh media was added and the stainless strip was removed. After a further 48 hours, the samples were taken down, stained with DAPI and analyzed for cell infiltration into the gap.

Osteogenic differentiation and total DNA content on nanofiber meshes

Random and aligned nanofiber mesh samples were coated with GFOGER, collagen, or left uncoated. hMSCs were seeded on circular mesh samples (diameter: 12 mm), cut using biopsy punches (Acuderm, Ft. Lauderdale, FL), at a density of 20,000 cells/cm^2. Four days after seeding, the hMSC growth media was replaced with osteogenic media, which consists of the hMSC growth media supplemented with 10 nM dexamethasone, 6 mM β-glycerol phosphate, 50 μg/ml ascorbic acid 2-phosphate and 50 ng/ml L-thyroxine (Sigma-Aldrich). Media was changed every 3-4 days and the samples were cultured for 3 weeks. The samples were analyzed for DNA content, alkaline phosphatase (ALP) activity and calcium deposition, as described previously (Chapter 3). Briefly, cells were lysed by freeze-thawing three times. The cell extract was used to measure DNA amount by the PicoGreen® dsDNA Quantitation Kit (Molecular Probes) and ALP activity by the use of *p*-nitrophenyl phosphate. The calcium content of a separate set of mesh samples was determined by using the dye Arsenazo III, after overnight incubation in 1 N acetic acid.

Assessment of GFOGER coated nanofiber meshes *in vivo*

The effect of GFOGER coating *in vivo* was investigated using a segmental bone defect model described previously [74]. Nanofiber meshes were used to create tubular implants, having a diameter of approximately 5 mm and a length of 13 mm, without any perforations (Chapter 5). The mesh tubes were coated with 50 μg/mL GFOGER overnight at 4°C, while control samples were left in PBS. Female Sprague-Dawley rats aged 13 weeks were used for this study. Both femurs were stabilized by fixation plates, and 8 mm segmental defects were created in the mid-diaphyses. Nanofiber mesh tubes were rinsed with PBS, and implanted in the defect, such that the periphery of the defect was covered with nanofiber mesh with the center empty.

Radiographs were obtained at 4 and 12 weeks, and *ex vivo* μCT analysis was performed at 12 weeks to detect bone formation. Torsional testing was performed on extracted femurs at 12 weeks to test their biomechanical properties. Histological analysis consisted of embedding in glycol methacrylate (GMA), obtaining 5 μm sections, and staining with H&E.

Data analysis

Data were analyzed using ANOVA and Tukey's tests for pairwise comparisons. Whenever required, the raw data was transformed using a natural logarithmic transformation to make the data normal and the variance independent of the mean [221]. Student's t-test was used for 2-sample comparisons, where it was appropriate. Other statistical tests that were performed for specific comparisons are mentioned in the results section. The significance level for the above analyses was set at $p<0.05$. Minitab® 15 (Minitab Inc., State College, PA) was used for all statistical analysis.

Results

Nanofiber mesh morphology and alignment

PCL nanofiber meshes were produced by electrospinning and characterized by analyzing SEM images. Interconnected, non-woven fibers that were mostly bead-free were obtained (Figure 4.2). The resulting nanofiber mesh is a porous structure, but due to the multiple fiber layers, the effective pore size appeared to be less than 2 μm, much less than hMSC dimensions. A flat stationary collector was used to obtain random nanofiber meshes with no dominant fiber orientation. The mean and median fiber diameters for random meshes were found to be 168.0 nm and 122.8 nm respectively. The distribution of fiber diameters indicated that the highest frequency occurred for fibers between 75 nm to 125 nm, with 90% of the fibers between 50-300 nm. To obtain aligned nanofiber meshes, a rotating mandrel was used to orient the fibers along the direction of rotation of

the mandrel surface (Figure 4.3 A). In this case, the mean and median fiber diameters were observed to be 256.4 nm and 227.4 nm. The fibers of the aligned meshes were found to be significantly larger in diameter than those in the random meshes (Mann-Whitney test; $p<0.001$). The angle of the fibers with respect to an arbitrary line was measured to quantify fiber alignment (Figure 4.3 B). Though there is a moderate spread in the orientation of the fibers, a preferred fiber direction was observed, with 89% of the fibers between -45 to 45°. For random meshes, this metric was calculated to be only 52%. Using a Z test for proportions, the alignment was found to be significantly higher in the case of aligned meshes ($p<0.0001$). hMSCs seeded on aligned nanofiber meshes exhibited a polarized morphology along the preferred fiber direction, while in the case of random nanofiber meshes, the cells did not display any regular orientation (Figure 4.3 C).

GFOGER coating of nanofiber meshes

The collagen-mimetic peptide: $GGYGGGPC(GPP)_5GFOGER(GPP)_5GPC$, containing the GFOGER motif, was synthesized by stepwise solid-phase procedures. The amino acid sequences adjacent to GFOGER enable formation of a stable right-handed triple helical configuration (Figure 4.4 A), which is required for cell adhesion [249, 262, 263]. The GFOGER peptide was passively adsorbed on the surface of nanofiber meshes at a concentration of 50 μg/mL. The adsorbed peptide was visualized by coating the meshes with a biotinylated GFOGER peptide and incubating in a fluorescein conjugated NeutrAvidin®. The images revealed that the peptide coated the individual fibers uniformly over the entire mesh area (Figure 4.4 B). An ELISA was performed to quantify the amount of the GFOGER peptide adsorbed on the nanofibers with varying peptide concentration. The saturation curve indicated that the relative surface density increased with increasing peptide concentration, with the surface being saturated at a concentration of approximately 20 μg/mL (Figure 4.4 C). The peptide concentration at which the surface is 50% saturated, was calculated to be 3.45 μg/mL. For all further experiments, a

peptide concentration of 50 µg/mL was used to ensure saturation of the surface for maximal biologic response.

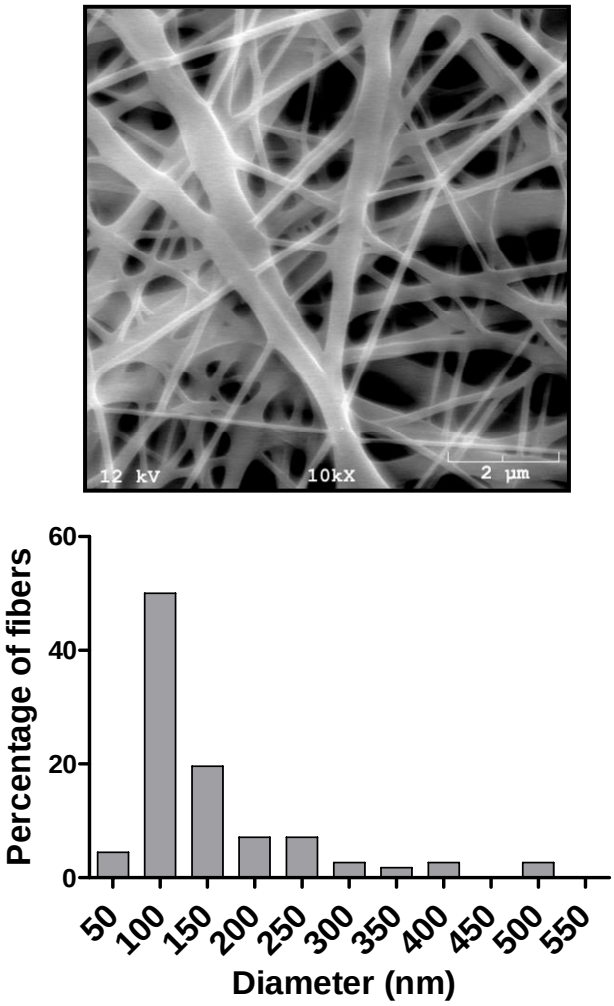

Figure 4.2. Nanofiber mesh morphology. (Top) A representative SEM image of a nanofiber mesh at 10,000X magnification illustrates smooth bead-free fibers. (Bottom) The fiber diameter histogram reveals that the fibers were in the nanometer range. The mean fiber diameter was found to be 168-nm.

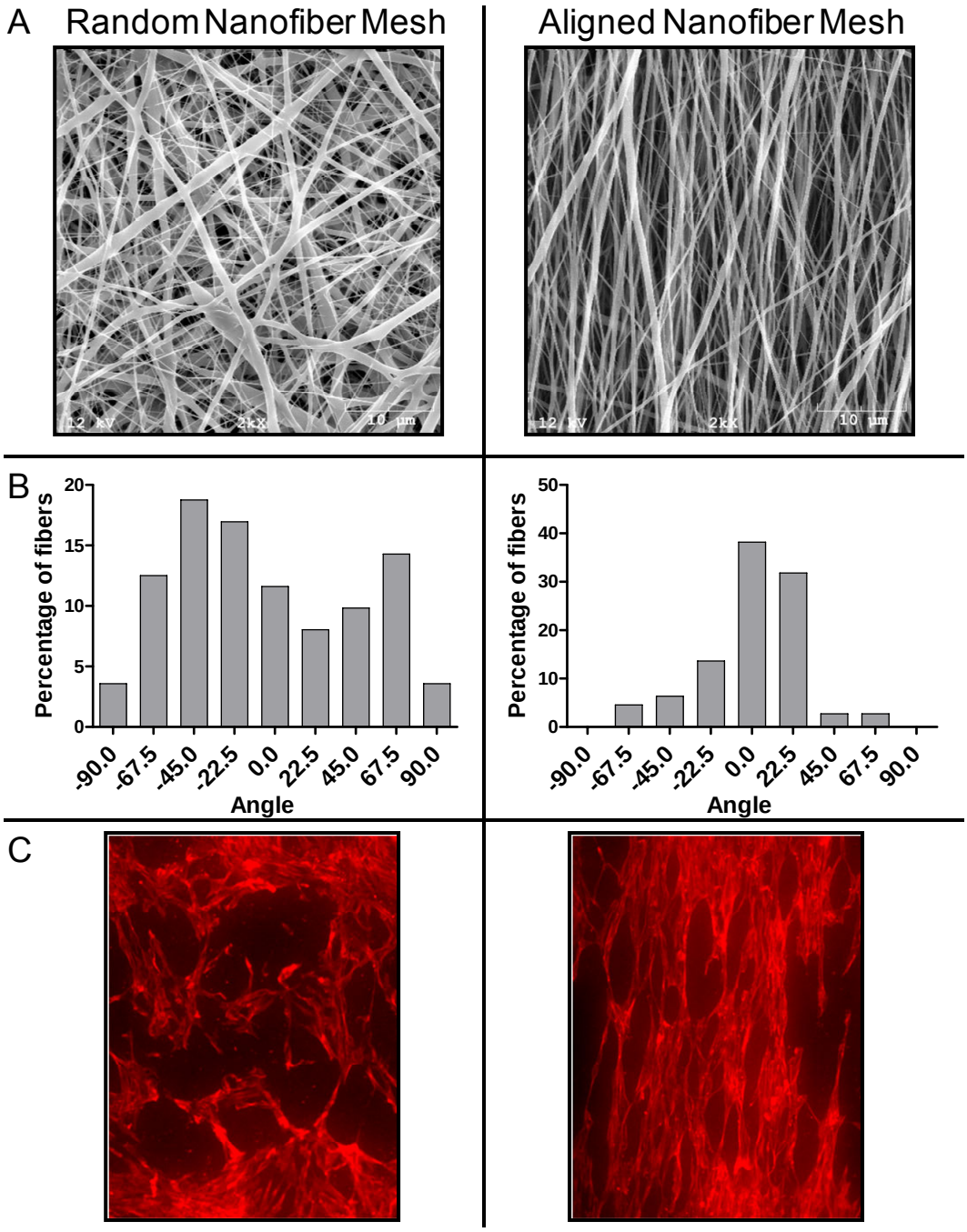

Figure 4.3. Fiber and cell alignment on nanofiber meshes. (A) SEM images of random and nanofiber meshes at 2000X magnification. (B) The fiber angle was measured from the SEM images and the distribution plotted to assess the fiber alignment. Fibers had a preferential orientation in the aligned mesh only. (C) hMSCs were seeded on random and aligned nanofiber meshes, and the cell alignment was observed by staining with rhodamine phalloidin. Images are at 10X magnification. hMSCs aligned along the fiber direction in the case of the aligned nanofiber mesh.

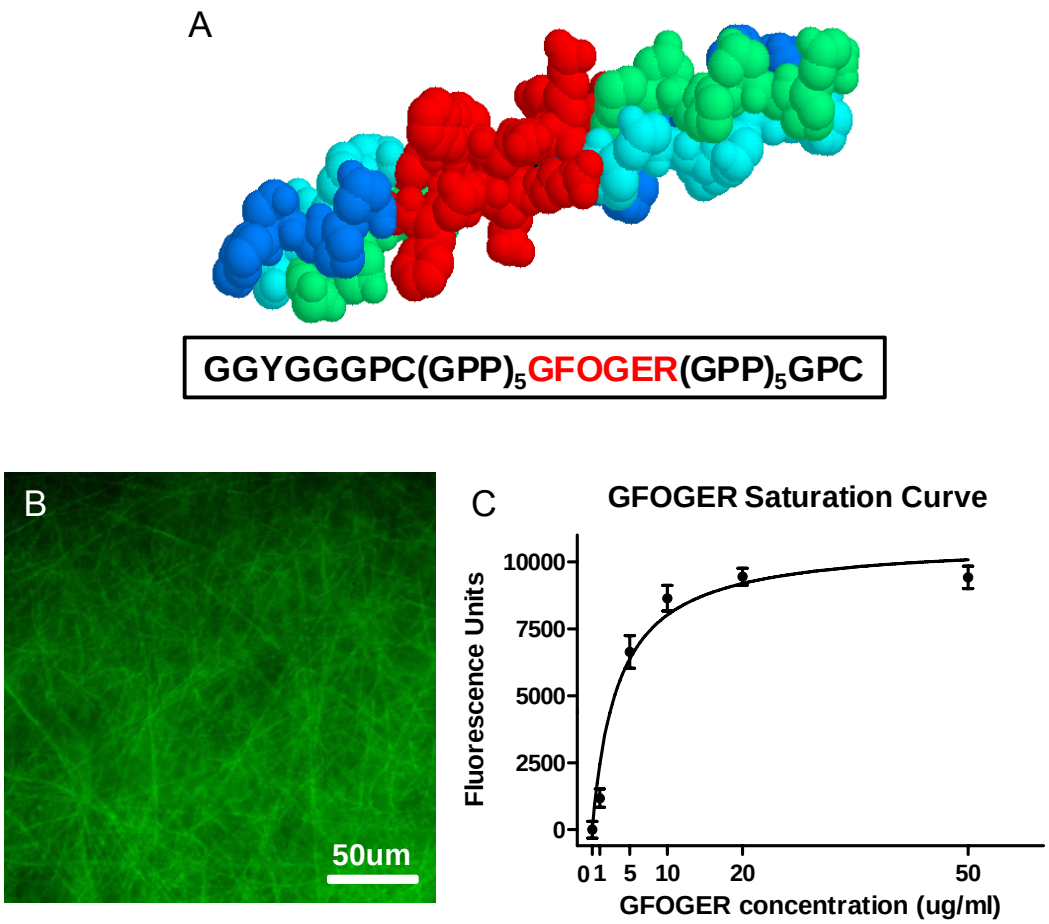

Figure 4.4. GFOGER coating of nanofiber meshes. (A) Space filling model of the triple helical GFOGER peptide (courtesy Dr. Andres J. Garcia, Georgia Tech). (B) Biotinylated GFOGER was passively adsorbed on nanofiber meshes, and the coating visualized using fluorescein conjugated NeutrAvidin®. (C) The amount of GFOGER adsorbed on nanofiber meshes with varying GFOGER concentration was quantified by an ELISA.

Cellular infiltration on nanofiber meshes

An *in vitro* model was developed to study the effect of GFOGER coating and fiber alignment on cellular infiltration on top of nanofiber meshes. A cell-free region was created on the mesh, and the infiltration of hMSCs into this gap was examined by analyzing the DAPI stained images. To observe baseline infiltration, we first performed the experiments with uncoated, random nanofiber meshes (Figure 4.5 A). We verified that a cell-free region was generated in day 0 samples. The mean gap width was found to be 0.874 ± 0.02 mm, which was slightly less than the width of the stainless steel strip (0.9 mm). The number of cells in the gap were counted on days 0, 3, 4 and 5. The cell count in the gap was found to be negligible on day 0. The quantification of cell infiltration revealed that there were significantly more cells in the gap on days 3 and 4 compared to day 0, and on day 5 compared to days 3 and 4 ($p<0.05$). The gap was not completely confluent with cells, even at day 5, indicating a slow infiltration rate on the uncoated and random nanofiber meshes. To investigate whether GFOGER coating had a significant effect on cell attachment efficiency, we counted the cells that attached outside the gap on day 0. The cell counts were observed to be equivalent in both the uncoated and GFOGER coated groups, indicating that GFOGER coating did not modify the cell attachment efficiency (Figure 4.5 B). This implies that both sets of samples start with comparable number of cells on the gap border.

The ability of GFOGER coating and fiber alignment to enhance cellular infiltration in this model was next studied on day 2 after strip removal. Some samples were coated with collagen to compare to the collagen-mimetic GFOGER peptide. The DAPI images revealed that the gaps on the GFOGER coated meshes were completely confluent with cells (Figure 4.6 A). Aligned and collagen coated meshes displayed moderately more cell infiltration than random and uncoated meshes, respectively. The cell numbers were determined in two regions: the entire gap and the middle-third of the gap. The middle-third region of the gap was analyzed as a more stringent measure of

cellular infiltration. Analysis of the cell counts indicates that both coating and fiber alignment had a significant effect on cell infiltration in both the regions (Figure 4.6 B). In the entire gap region on random meshes, GFOGER coated samples displayed higher cell numbers, compared to both uncoated and collagen samples. On the aligned meshes, both GFOGER and collagen coated samples had higher cell counts than the uncoated samples. Fiber alignment enhanced cell infiltration on uncoated and collagen coated samples. However, this effect was not seen on the GFOGER coated meshes, probably due to the fact that the gap was saturated with cells, even on the GFOGER coated, random meshes. Analysis of the middle-third region of the gap revealed that the cell counts displayed the following order for both random and aligned meshes: GFOGER > Collagen > Uncoated. Fiber alignment enhanced the cell infiltration on both uncoated and collagen coated samples, similar to the observation in the entire gap.

Effect of cell proliferation on the infiltration of cells on nanofiber meshes

The cell infiltration observed on nanofiber meshes could be due to the migration and/or proliferation of hMSCs. To assess the contribution of cell proliferation, we blocked proliferation by treating the cells with mitomycin C, a known inhibitor of cell proliferation, 24 hours after seeding. We verified that mitomycin C was able to inhibit proliferation of hMSCs on tissue culture plates by staining with BrdU, a marker of cell proliferation (Figure 4.7). The results demonstrate that 48 hours after mitomycin incubation, the number of proliferating cells (seen with BrdU staining) decreased, thereby reducing the total number of cells (seen with DAPI staining) at this time point. In the absence of mitomycin C, the proportion of proliferating cells during the 24 hour period was 84.1%. This proportion decreased significantly to 6.4% in the presence of mitomycin C, indicating that mitomycin C blocked proliferation in almost all hMSCs.

The effect of inhibiting cell proliferation on the infiltration of hMSCs on nanofiber meshes was next investigated. hMSCs were seeded on nanofiber meshes, with

a stainless steel strip placed on top, and allowed to attach for 24 hours (Figure 4.8 A). The cells were incubated with mitomycin C for 60 minutes, and the strip was removed. After 48 hours of strip removal, the samples were stained with DAPI and analyzed for cell infiltration (Figure 4.8 B). The analysis of both the entire gap and the middle-third gap regions revealed that in the absence of mitomycin C, both GFOGER coating and fiber alignment enhanced cell infiltration, as observed before. With mitomycin C incubation, the overall cell infiltration decreased, indicating that cell proliferation contributed significantly to the infiltration. In the presence of mitomycin C, only the aligned, uncoated mesh samples had a significantly higher cell count than the random, uncoated mesh samples, in the entire gap region. In contrast, in the middle-third of the gap, the random, GFOGER-coated samples demonstrated significantly higher infiltration than the random, uncoated samples. Furthermore, the aligned, uncoated group displayed a higher cell count than the random, GFOGER-coated group. These results suggest that both cell proliferation and migration contribute to the observed cell infiltration on meshes, and that proliferation has a larger influence on infiltration due to GFOGER coating, compared to fiber alignment.

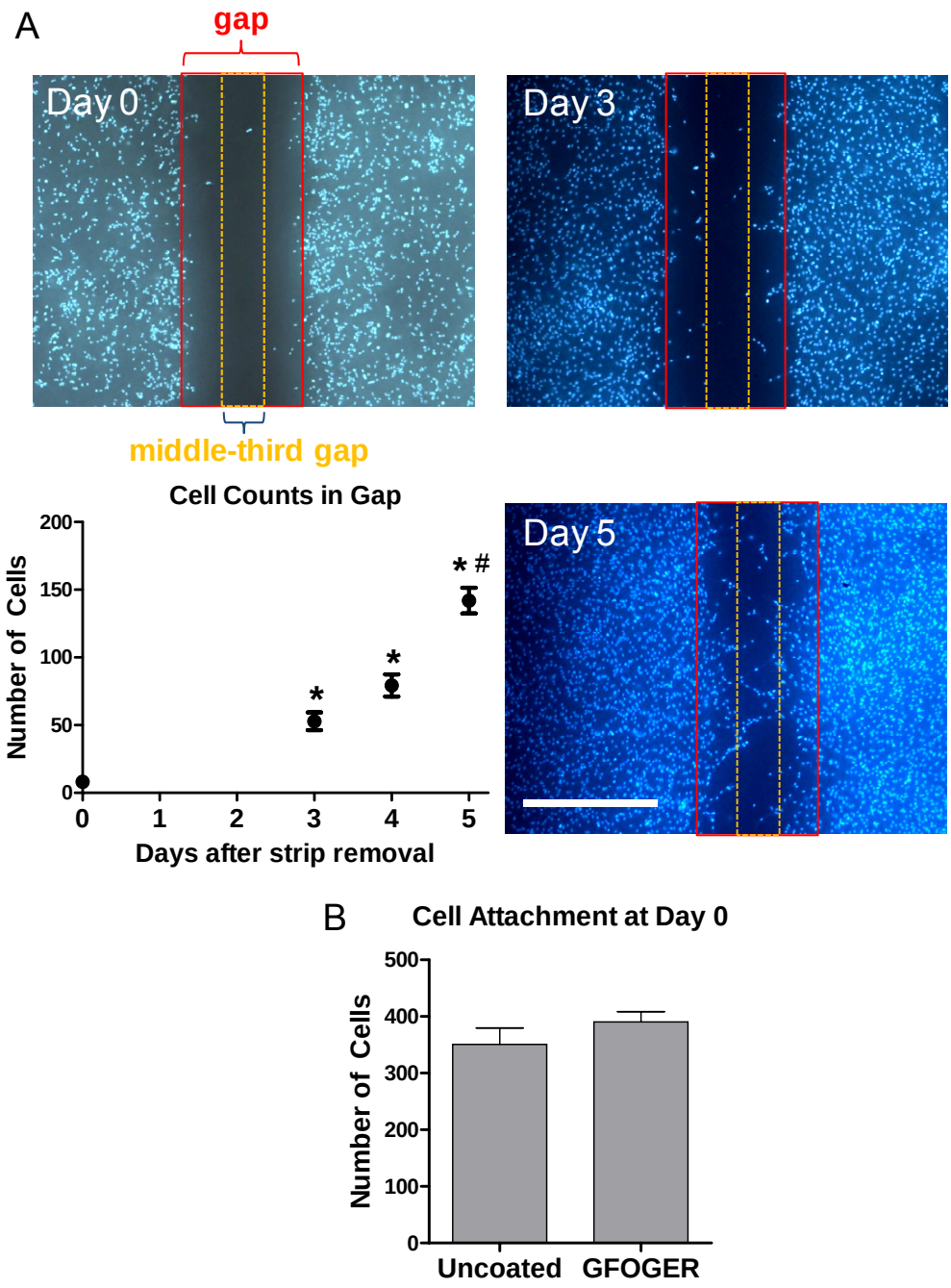

Figure 4.5. Kinetics of cell infiltration on uncoated random nanofiber meshes. (A) The cells in the entire gap were examined on days 0, 3, 4 and 5 after strip removal by DAPI staining. The cell number was quantified by counting the nuclei, and revealed a slow infiltration rate. A middle-third gap region was defined for later studies. Scale bar is 1 mm and applies to all images. (B) The cells attachment efficiency was investigated by quantifying the number of cells that attached outside the gap on day 0. There was no effect of GFOGER coating on cell attachment efficiency. * indicates significantly greater than cell number on day 0. # indicates significantly greater than cell number on days 3 and 4. Significance was set at $p<0.05$.

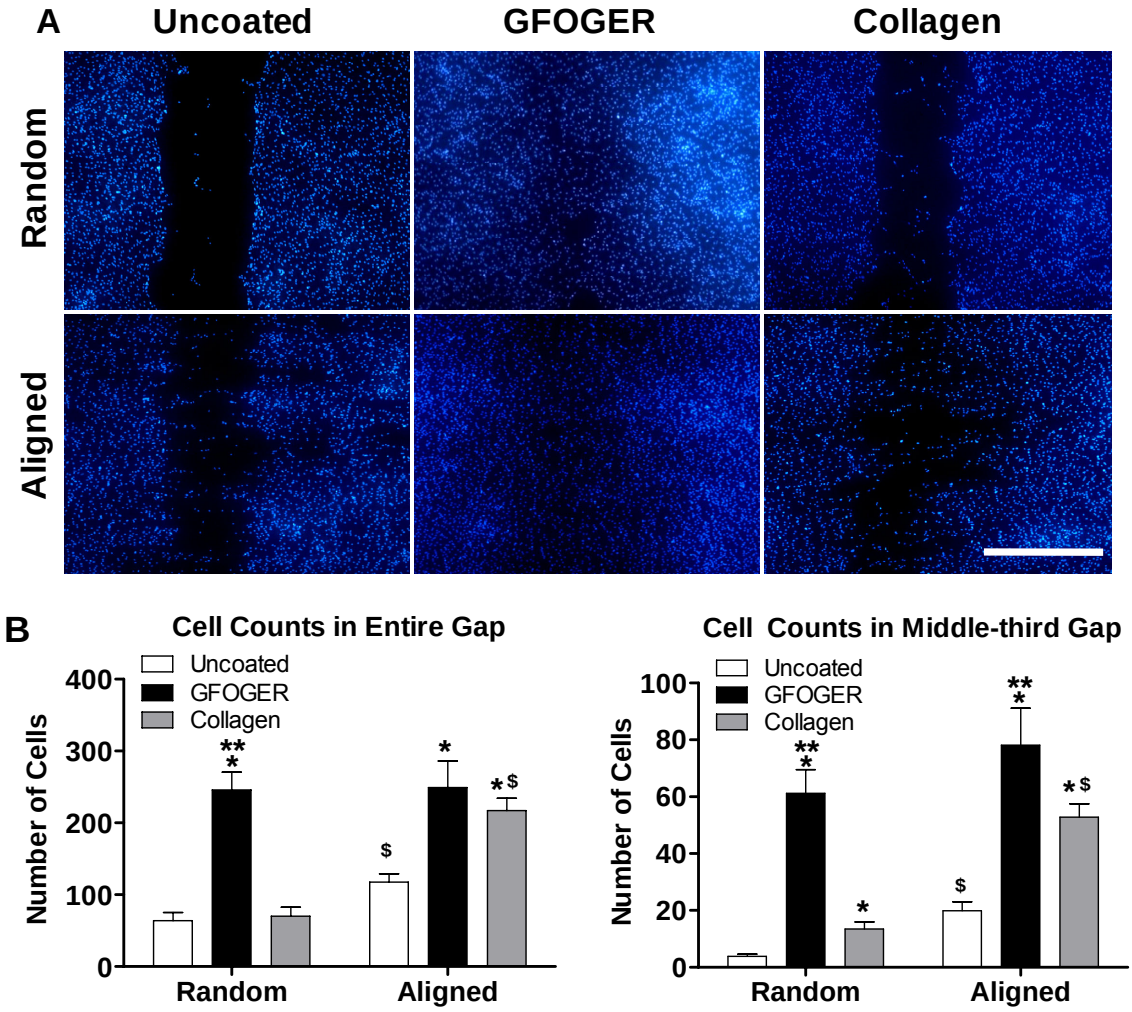

Figure 4.6. Effect of coating and fiber alignment on cell infiltration at 48 hours after strip removal. (A) Images of DAPI stained nanofiber mesh samples illustrating the differences in the degree of cell infiltration. Scale bar is 1 mm and applies to all images. (B) The number of cells present in both entire gap as well as the middle-third of the gap was counted to quantify cell infiltration. ANOVA revealed that both GFOGER coating and fiber alignment enhance cell infiltration. * indicates significantly greater than uncoated with same fiber orientation. ** indicates significantly greater than collagen with same fiber orientation. $ indicates greater than random orientation with same coating. Significance was set at $p<0.05$.

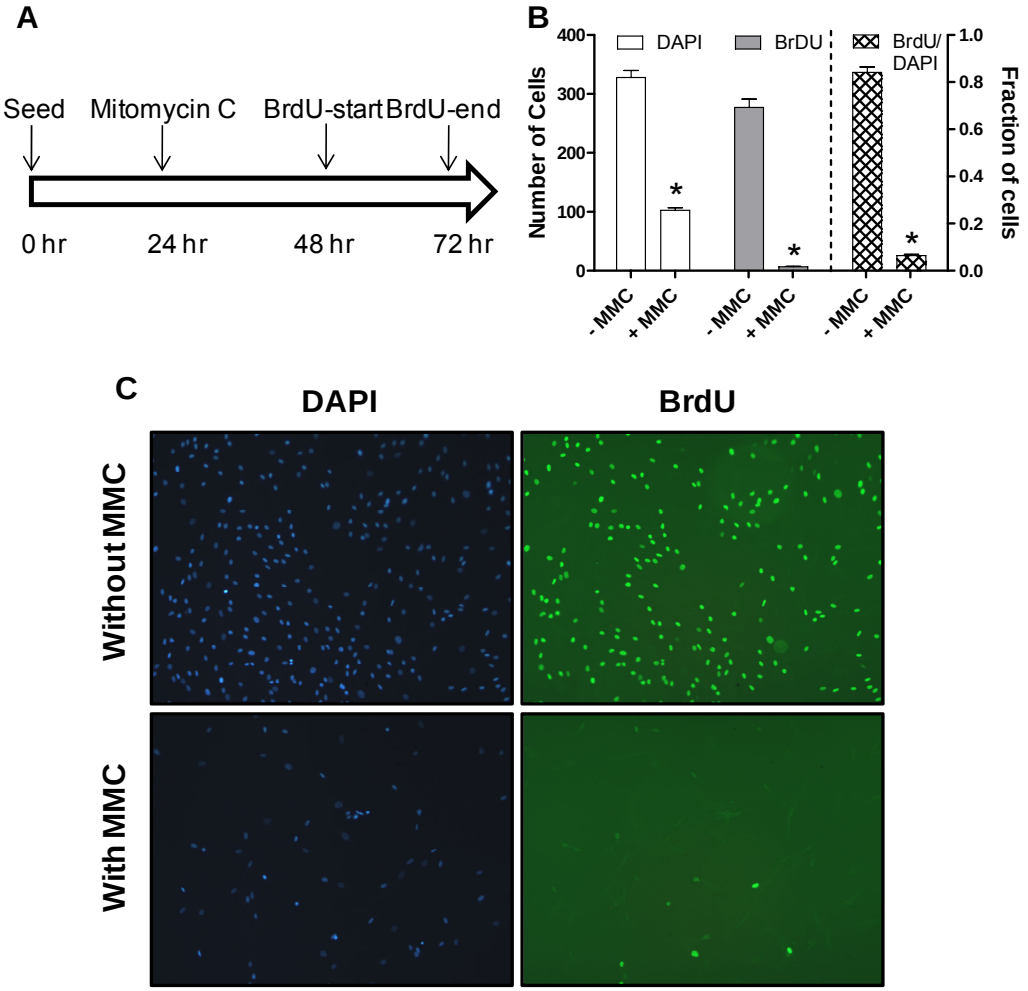

Figure 4.7. Effect of mitomycin C on hMSCs proliferation on tissue culture plastic. (A) Time-sequence of steps in this experiment. Cells were incubated with mitomycin C 24 hours post-seeding to block proliferation, and proliferation was assessed by BrdU staining that ended 48 hours after mitomycin C incubation. (B) The number of BrdU and DAPI stained cells were counted in a 3×3 grid pattern. Data are presented as the BrdU and DAPI cell counts, as well as the proportion of BrdU positive cells. MMC: mitomycin C. * indicates significantly less than without MMC ($p<0.05$). (C) BrdU and DAPI images (10X) illustrating that cell proliferation was inhibited by mitomycic C.

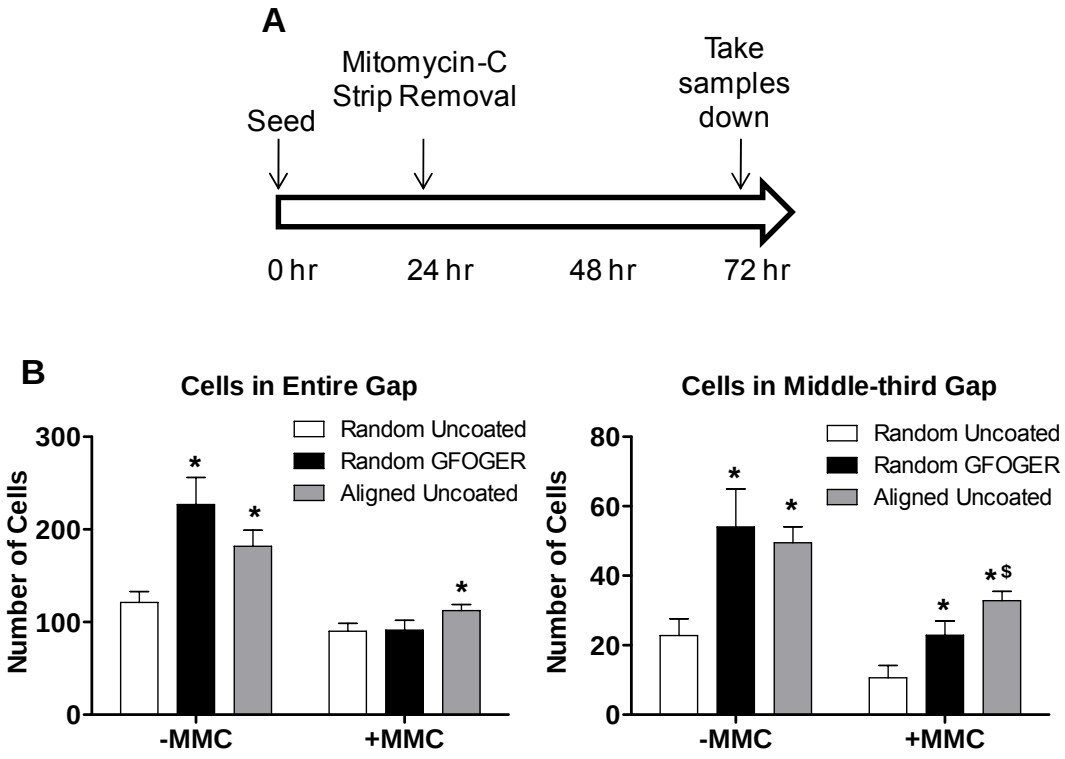

Figure 4.8. Role of cell proliferation in the cell infiltration model. (A) Time-sequence of steps in this experiment. After seeding, cells were allowed to attach for 24 hours, following which they were incubated with mitomycin C and the stainless strip was removed. Samples were taken down 48 hours after strip removal. (B) The cell counts demonstrated that blocking proliferation resulted in reduced infiltration, indicating that both proliferation and migration contribute to cell infiltration. MMC: mitomycin C. * indicates significantly greater than random uncoated with same MMC condition ($p<0.05$). $ indicates significantly greater than random GFOGER with same MMC condition ($p<0.05$).

Influence of nanofiber coating and alignment on total DNA content and osteogenic differentiation

Cells were seeded on circular nanofiber meshes and cultured in either hMSC growth or osteogenic media up to 21 days. This culture system does not involve the use of a stainless steel strip, and the cells are uniformly distributed on the mesh. First, the effect of GFOGER coating on changes in cell number was studied by measuring the amount of DNA extracted from the samples at days 4 and 7. The results demonstrate that GFOGER coating increased the amount of DNA in osteogenic media samples at both days 4 and 7, suggesting an improved proliferation rate (Figure 4.9). GFOGER coating did not have a significant effect on amount of DNA in growth media. The effect of coating and fiber alignment on DNA content in osteogenic media was investigated at a later time point of 21 days. ANOVA revealed that coating had an overall significant effect on amount of DNA, but there were no significant individual differences between the groups (Figure 4.10 A).

The influence of nanofiber coating and alignment on the osteogenic differentiation of hMSCs in osteogenic media was studied by measuring the ALP activity and calcium deposition. Analysis of the ALP activity data revealed that both coating and fiber alignment had a significant effect on ALP activity, and that the GFOGER-coated samples displayed an overall higher ALP activity than the uncoated and collagen coated groups (Figure 4.10 B). In the case of random nanofiber meshes, the GFOGER group also demonstrated significantly higher ALP activity than the uncoated and collagen groups, whereas, on aligned meshes, the GFOGER group displayed significantly higher activity than the collagen group only. Fiber alignment was found to reduce the ALP activity, in the case of GFOGER- and collagen-coated samples.

Under osteogenic stimulation, hMSCs deposited calcium on the nanofiber meshes, indicative of an osteoblast phenotype (Figure 4.10 C). GFOGER coating

significantly enhanced calcium deposition on both random and aligned meshes, compared to uncoated meshes. In addition, on random meshes, GFOGER-coated samples demonstrated significantly higher calcium deposition than collagen-coated samples. Collagen coating increased calcium levels only in the case of aligned meshes. Fiber alignment did not have an overall significant effect on calcium deposition, though a reduction was observed in the case of uncoated meshes.

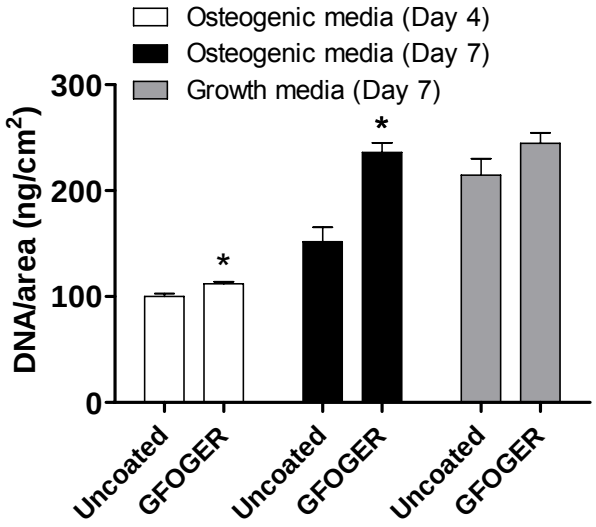

Figure 4.9. Early effect of GFOGER coating on hMSC number. DNA amount was quantified as a measure of cell number on days 4 and 7, in growth and osteogenic media. GFOGER coating increased DNA amount in osteogenic media at both days 4 and 7. * indicates significantly greater than uncoated in the same group.

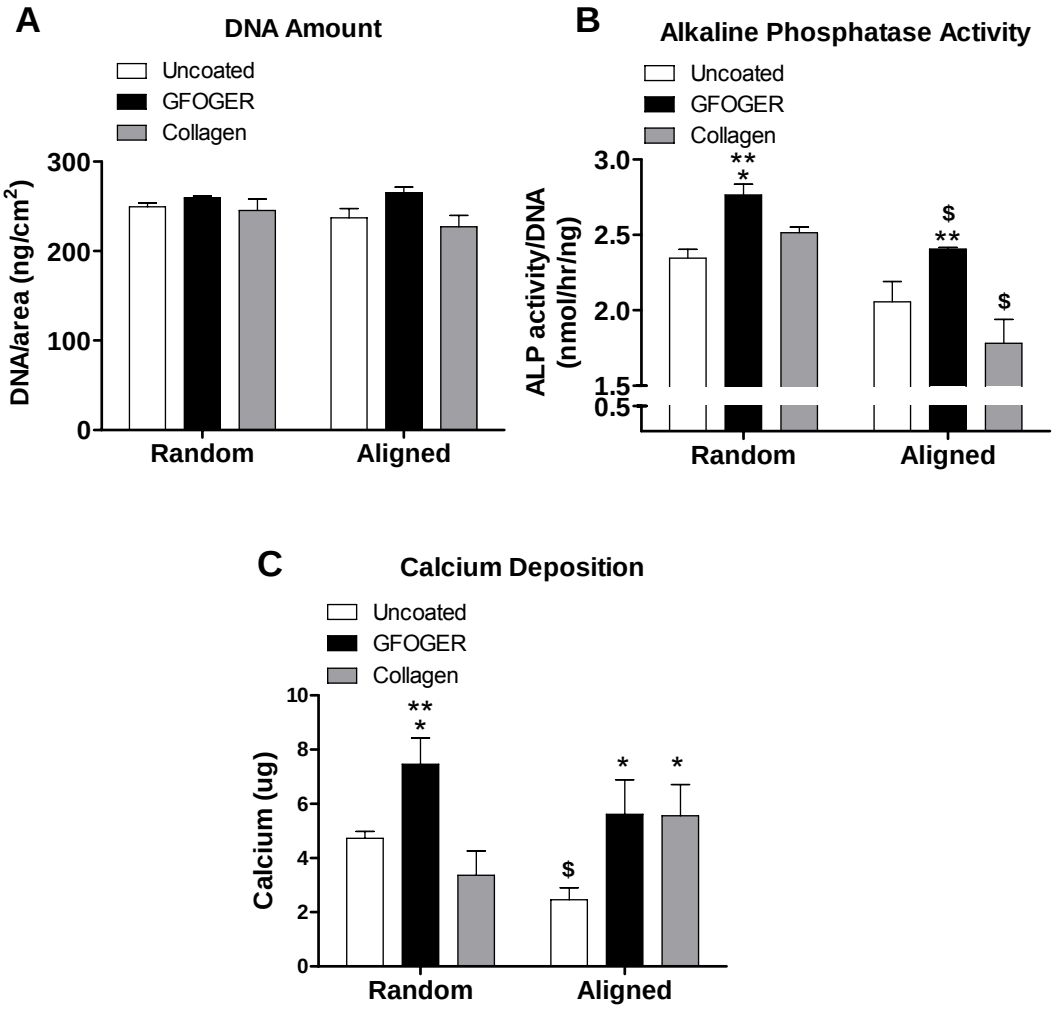

Figure 4.10. Effect of coating and fiber alignment on cell number and osteogenic differentiation of hMSCs in osteogenic media. Cells were seeded on circular nanofiber mesh samples and cultured in osteogenic media for 21 days. (A) DNA amount. No significant differences were seen in the amount of DNA between groups. (B) Alkaline phosphatase (ALP) activity. Samples coated with GFOGER demonstrated increased ALP activity, whereas those with aligned fibers displayed a reduction in ALP activity. (C) Calcium deposition. GFOGER coating enhanced calcium deposition by hMSCs on nanofiber meshes. Fiber alignment did not have a significant overall effect.

Assessment of GFOGER coated nanofiber meshes *in vivo*

To investigate the ability of GFOGER coated nanofiber meshes to enhance bone formation *in vivo*, tubes made from nanofiber meshes were coated with the GFOGER peptide, or left uncoated, and implanted around segmental bone defects created in rat femurs. Radiographs at 4 and 12 weeks displayed new bone formation near the ends and the periphery of the defect (Figure 4.11). However, none of the defects were bridged completely. The results of the μCT analysis and torsional testing at 12 weeks revealed no significant differences between the two groups, indicating that coating nanofiber mesh tubes with GFOGER did not enhance bone formation in this model (Figure 4.12). The cross sectional views of the μCT images illustrated some bone formation along the nanofiber mesh tube and at the native bone boundary. However, capping of defect ends was observed, and presence of bony tissue was not evident at the defect center. Histological analysis of the defect area confirmed capping of the defect ends with newly formed bone (Figure 4.13). A combination of newly formed bone, fibrous tissue and marrow was seen within the defect.

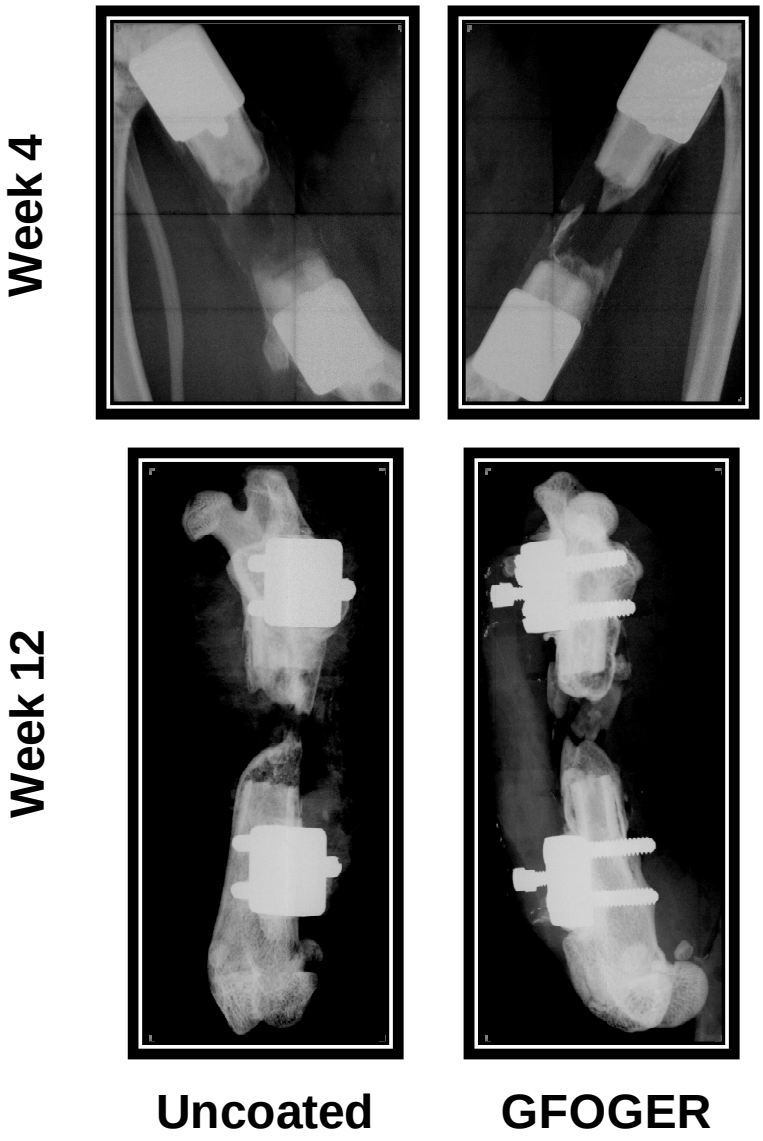

Figure 4.11. Radiographs of femurs implanted with nanofiber mesh tubes at 4 and 12 weeks. Specimens in both groups displayed new bone formation near the ends and the periphery of the defect. None of the defects were bridged completely.

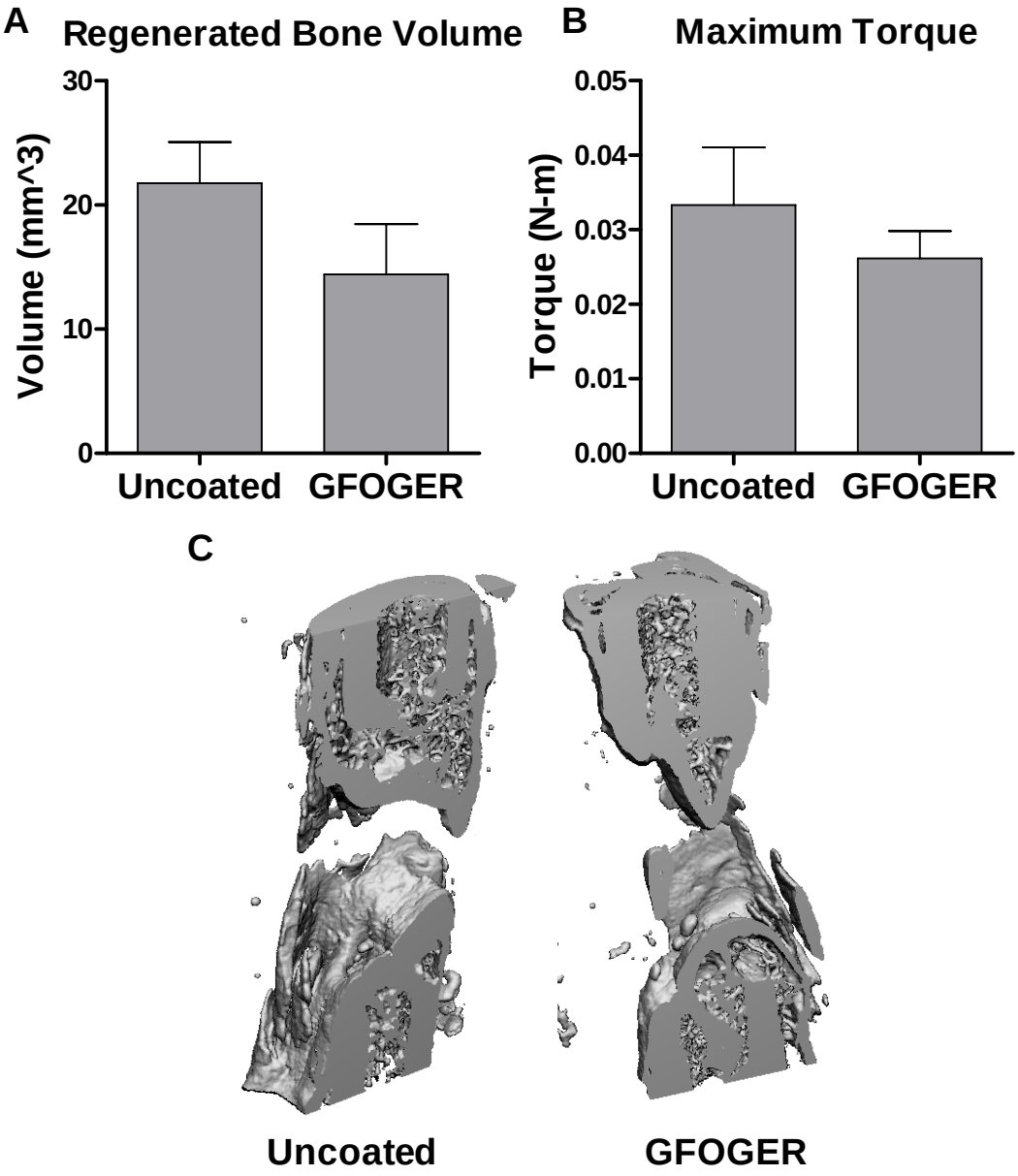

Figure 4.12. μCT analysis and mechanical testing of extracted femurs at 12 weeks. (A) Regenerated bone volume from μCT analysis. GFOGER coating did not have a significant effect on bone volume. (B) Failure strength was calculated by measuring the maximum torque in torsional testing. No significant differences were seen between the groups. (C) Cross sections of μCT images reveal capping of defect ends and some bone formation along the nanofiber mesh tube.

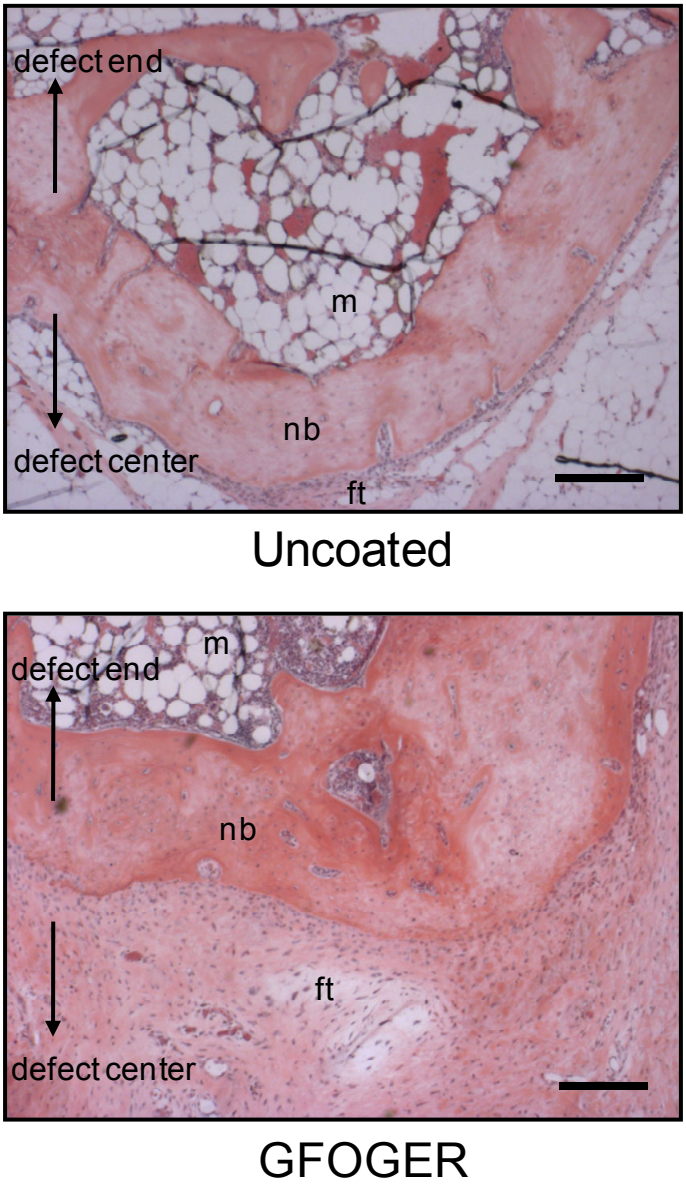

Figure 4.13. Histological analysis with H&E staining at 12 weeks. The defect in both groups contains a combination of newly formed bone (nb), fibrous tissue (ft) and marrow (m). The regenerated bone is limited to the defect ends with capping of the native bone ends. The defect center is populated with fibrous tissue. Scale bars are 200-μm.

Discussion

In this study, we developed bioactive nanofiber meshes with ordered topography for enhancing tissue repair. Nanofibers were functionalized with passive adsorption of the collagen-mimetic GFOGER peptide, and the nanotopography was patterned by aligning nanofiber orientation. The effects of these parameters on the migration, proliferation and osteogenic differentiation of hMSCs were studied. Our results indicate nanofiber surface functionalization and orientation modulate cellular behavior, individually and in combination. GFOGER coating and fiber alignment enhanced hMSC infiltration on nanofiber meshes. Both cellular proliferation and migration contributed to the observed infiltration, with proliferation exerting a larger influence on infiltration due to GFOGER coating, compared to fiber alignment. In contrast, only GFOGER coating enhanced the osteogenic differentiation of hMSCs.

The infiltration of hMSCs into a gap region on top of nanofiber meshes was studied *in vitro* using a modified version of the scratch wound healing assay, which is performed frequently to study migration on tissue culture plastic [261, 264]. Cell infiltration was investigated because it is an important initial step in recruiting endogenous progenitor cells for tissue repair *in vivo*. In addition to analyzing the entire gap region, we also measured cell infiltration in the middle-third area of the gap to isolate cells that infiltrated farther as a more stringent measure of infiltration. It is possible that some of the cells located just inside the gap boundary may be there simply due to the division of cells outside the gap, rather than due to an active response to nanofiber surface modification.

The functionalization of nanofiber surface with GFOGER resulted in the largest elevation of hMSC infiltration (as much as a 16-fold increase), higher than both collagen coating and fiber alignment. Whereas cells did not completely occupy the gap region on uncoated meshes even after 5 days, the gap in the GFOGER coated samples was confluent with cells, just after 2 days. To investigate whether the groups started with

comparable number of cells at the gap boundary, we measured the cell attachment efficiency at 24 hours, the time of strip removal. It was observed that this was indeed the case, with no difference detected between the numbers of cells outside the gap. It is also interesting to note that GFOGER coating displayed a significantly larger effect on cell infiltration compared to collagen coating, even though their effects on cell adhesion has been shown to be equivalent previously [251].

The alignment of fibers along a preferred direction enhanced hMSC infiltration into the gap along this direction. Collagen coating and fiber alignment displayed a synergistic effect on cell infiltration. Fiber alignment did not add to the infiltration in the GFOGER coated groups. However, this was probably because the gap in the GFOGER coated samples was already confluent with cells, even on random meshes, and there was no additional room for cells to infiltrate. Patel and coworkers reported a similar synergistic effect of fiber alignment and protein immobilization on fibroblast infiltration on nanofiber meshes [265]. Though individual fibers were not perfectly oriented along a single direction, the cells that attached to the meshes aligned themselves along the preferred direction. This contact guidance may explain the improved infiltration of cells into the gap. Contact guidance due to fiber alignment has been reported previously in studies published by Bashur et al. and Yang et al., where they observed an increase in cell spreading and aspect ratio on aligned meshes [257, 266]. The fiber diameter in the case of aligned meshes was found to be higher than that in random meshes (256.4 nm vs. 168.0 nm). This was probably due to differences in the electrostatic fields between the stationary and rotating collector setups. Though different configurations of the rotating mandrel were attempted, it was not possible to get similar fiber diameters while maintaining good fiber alignment. It is possible that the difference in fiber diameter may contribute to the observed differences in cell behavior on aligned nanofiber meshes. However, the fibers are still in a narrow submicron range, and the cells may not be able to sense the differences in fiber diameter. This hypothesis is supported by studies that

have reported insignificant differences in cell function with varying fiber diameters within the submicron range [192, 266].

The observed infiltration of cells on nanofiber meshes occurs either due to the physical migration of individual cells, or due to cell proliferation, or a combination of both. To isolate the individual contributions, we blocked proliferation by incubating the cells with mitomycin C. In the absence of proliferation, the infiltration dropped in all groups, indicating that the infiltration on nanofiber meshes is dependent, at least to a certain extent, on cell proliferation. Part of the reduction in total cell numbers could be explained by a decrease in the viability of hMSCs due to mitomycin C; however there is some evidence in the literature that this is not the case [267]. The reduction in infiltration was especially high for the GFOGER coated samples, in which the improvement in infiltration was abolished, when measured in the entire gap region. In the middle-third gap region however, GFOGER coating still enhanced cell infiltration, indicating that at least some of the positive effects of GFOGER coating on infiltration are due to cell migration. This also suggests that the cell counts in the middle-third gap region are a more sensitive measure of cell migration than those in the entire gap. Compared to the GFOGER samples, the aligned meshes were less affected by the inhibition of proliferation, and demonstrated more infiltration in both the gap regions. Overall, these results suggest that both migration and proliferation contribute to the hMSC infiltration that was observed on nanofiber meshes. Kark et al. reported similarly that the gap closure on tissue culture plates, by rat MSCs in response to platelet releasate, was due to the combined effects of migration and proliferation [261]. The mode of infiltration on GFOGER coated samples appears to be more dependent on proliferation, whereas it is more dependent on migration in the case of aligned meshes.

The mechanisms for the improved cellular infiltration on GFOGER coated nanofiber meshes are likely related to the adhesive properties of the collagen-mimetic GFOGER peptide. It is now clear that the GFOGER hexapeptide, which is a sequence in

the α_1(I) chain of type I collagen, is a major binding site for the $\alpha_2\beta_1$ integrin [249, 263]. The $\alpha_2\beta_1$ integrin is abundantly expressed in a wide variety of cells, including MSCs [268]. Since the engagement of integrins with ECM molecules regulate adhesion related functions of cells, which include migration and proliferation, it is plausible that the GFOGER-$\alpha_2\beta_1$ integrin interaction may be driving the infiltration on nanofiber meshes [269-272]. Senger et al. demonstrated that blocking the $\alpha_2\beta_1$ integrin by a soluble antibody resulted in ~40% inhibition of endothelial cells migration toward type I collagen [273]. In addition, Reyes and coworkers have reported that cell adhesion was greater and specific to the $\alpha_2\beta_1$ integrin, when titanium surfaces were coated with GFOGER, compared to uncoated, RGD coated and even serum coated samples [121]. Finally, the GFOGER peptide has been shown to promote formation of mature integrin-mediated focal adhesions, an important event for post-adhesion intracellular signaling [251].

The effects of the mesh design parameters on the proliferation and differentiation of hMSCs on nanofiber meshes were also investigated. Proliferation was studied indirectly by determining the DNA content as a measure of cell number. However, this provides only a snapshot of the number of cells at any time point, and any changes in DNA content could be due to differences in cell attachment, viability and proliferation rate. Since the cell attachment (Figure 4.5) and viability (data not shown) were not significantly affected by mesh design, the DNA amount may be interpreted to be largely determined by the proliferation rate. The quantification of DNA amount in the first week of culture indicated higher DNA content on the GFOGER coated meshes in osteogenic media, suggesting an early enhancement of proliferation by GFOGER. However, by 21 days, there was no significant effect of GFOGER coating on DNA content.

The osteogenic differentiation of hMSCs on nanofiber meshes was evaluated by measuring the ALP activity and the calcium deposition. ALP is a membrane-bound enzyme that hydrolyzes phosphate esters during mineralization, and is considered a marker of early osteogenic differentiation [224]. On the other hand, calcium deposition is

a final measure of matrix mineralization. GFOGER coating enhanced both the ALP activity and calcium deposition, indicating that the peptide is able to differentiate hMSCs to an osteoblast-like phenotype. The GFOGER-$\alpha_2\beta_1$ integrin interaction has been implicated in mediating osteoblast adhesion, differentiation and matrix mineralization [117, 118]. Reyes and coworkers have previously reported the osteogenic differentiation of immature osteoblasts and rat MSCs when cultured on GFOGER coated surfaces [120, 121]. They demonstrated that the peptide triggers signaling pathways that result in the upregulation of Runx2/Cbfa1, a transcriptional activator essential for osteogenic differentiation [120, 274-276]. In contrast to GFOGER coating, fiber alignment did not have an overall positive effect on osteogenic differentiation, and in some groups resulted in a reduction in ALP activity and calcium deposition. This may be due to the cells being more migratory on aligned meshes.

The *in vivo* results indicated that GFOGER coating of nanofiber mesh tubes did not enhance the repair of segmental bone defects. Defects in both the uncoated and the GFOGER coated groups displayed a moderate amount of new bone formation; however, none of the defects were bridged with bony tissue. Unsurprisingly, the biomechanical properties were also found to be much less than that of native bone (failure strength <0.05 N-m compared to 0.31 N-m). Histological analysis revealed that the native bone ends were capped with newly formed bone, with the defect center occupied with fibrous tissue. Taken together with our other *in vivo* data (Chapter 5), these results suggest that when nanofiber mesh tubes are placed alone in large diaphyseal defects with the center left empty, they are not able to provide the structure necessary for complete defect bridging. Previous results have demonstrated the *in vivo* efficacy of the GFOGER peptide for implant osseointegration [121]. In addition, Wojtowicz et al. recently reported that GFOGER coating of three-dimensional scaffolds, with honeycomb architecture, enhanced bone formation in a similar segmental defect model [277]. It is possible that in our system, the GFOGER peptide may present an insufficient osteogenic signal for a

robust healing response, because it is available only on the defect periphery along the mesh tubes. In fact, Wojtowicz et al. reported that bone formation was sensitive to scaffold surface area, with reduced surface area resulting in the suppression of the GFOGER effect [277]. This suggests that nanofiber mesh tubes may not be an appropriate scaffold for providing GFOGER coated surfaces for the repair of large diaphyseal defects. Augmenting the GFOGER coated mesh tubes with another biomaterial inside the tubes may be an effective strategy for diaphyseal defect healing, and this needs to be explored further.

In conclusion, this study demonstrates that nanofiber orientation and surface functionalization modulate hMSC infiltration and osteogenic differentiation. Coating nanofibers with the collagen-mimetic peptide GFOGER enhanced the migration, proliferation and osteogenic differentiation of hMSCs, likely by engaging the $\alpha_2\beta_1$ integrin receptor. GFOGER coated nanofiber meshes were unable to functionally repair large diaphyseal bone defects *in vivo*, and modifications in the scaffold configuration would be needed for improved delivery of the peptide. Fiber alignment increased cell migration on nanofiber meshes along the direction of fiber orientation due to contact guidance, but did not demonstrate a positive effect on osteogenic differentiation. Overall, these results indicate that such design strategies modulating nanofiber orientation and functionalization present a promising biomaterial-based therapy for improving tissue regeneration.

CHAPTER 5

A NOVEL HYBRID SYSTEM FOR GROWTH FACTOR DELIVERY PROMOTES FUNCTIONAL REPAIR OF LARGE BONE DEFECTS

Introduction

Autologous and allogeneic bone grafting are the most widely used treatment modalities for fracture non-unions and large bone defects [45, 49]. However, these techniques are associated with a number of drawbacks, including the limited graft material available for autografts and the high failure rate of allografts [53, 55, 56]. These limitations have stimulated the search for improved techniques for bone repair, and tissue engineering/regenerative medicine (TE/RM) strategies have demonstrated significant potential in developing bone graft substitutes [75, 76]. These approaches promote tissue repair by providing a combination of physical and biochemical cues through structural scaffolds and biologics [64, 65, 77].

Much of bone TE/RM research is focused on the use of three-dimensional scaffolds having adequate strength to support *in vivo* loading [74, 91, 278]. However, structural scaffolds usually do not provide an optimal environment for cellular function and suffer from slow resorption kinetics, thereby impeding functional restoration of the damaged tissue. We previously demonstrated, for example, that poly (L,DL, lactide) scaffolds infused with recombinant human bone morphogenetic protein 2 (rhBMP-2) promoted bone ingrowth but failed to fully restore the mechanical properties of long bone defects [74]. Thin, two-dimensional membranes have been used to promote bone repair by placing them along the periosteal surface to demarcate the osseous from the non-osseous region [92-95]. This technique, termed guided bone regeneration, has been applied successfully in the dental field to regenerate lost alveolar bone [175, 176]. However, few previous studies have investigated the use of polymer membranes in the

treatment of large defects in load bearing bones, and none have quantitatively evaluated the restoration of limb function [179, 181, 184].

Electrospun nanofiber meshes have recently emerged as a new generation of scaffold membranes, possessing a number of features suitable for tissue regeneration [90, 98]. They have fibers of the same size-scale of extracellular matrix (ECM) components and a large surface area, which may improve cellular attachment, morphology, migration and function. Nanofiber meshes have been shown to support osteogenic differentiation of progenitor and stem cells *in vitro* [192, 214, 279, 280], and have been tested in calvarial defect models *in vivo* [96, 193]. However, their efficacy in guiding long bone regeneration *in vivo* remains to be investigated.

Though a scaffold provides a template for guiding bone regeneration, biologic factors such as cells, growth factors or genes are typically required to effectively fill challenging bone defects [74, 125]. Osteoinductive growth factors like rhBMP-2 have demonstrated some clinical success for bone healing, but large doses are needed [101, 241]. Delivery systems that provide sustained release and improved local retention may provide efficacy at lower protein dose, thereby minimizing complications and making the therapy more cost effective [61, 63, 143, 147]. Alginate hydrogels, made from brown algae derived polysaccharides, have been established as a scaffolding material [105] and a spatiotemporal delivery vehicle for a wide range of proteins [170-172]. Though mammalian cells lack receptors for alginate polymers, the alginates can be covalently coupled with adhesion peptides to promote cellular attachment [173]. In addition, the degradation rate of these hydrogels can be increased by Gamma-irradiation, resulting in lower molecular weight polymers. These modified alginates have been demonstrated to be better suited for TE/RM applications by allowing faster ingrowth of cells and tissue [105, 174].

The primary objective of this study was to develop and test a hybrid growth factor delivery system for bone repair that utilizes an electrospun nanofiber mesh and injectable alginate hydrogel. To test this system, we evaluated its ability to deliver rhBMP-2 for the repair of critically-sized segmental bone defects *in vivo*. For control group comparisons, we also examined the ability of the nanofiber mesh alone, and in combination with alginate hydrogel, to heal the bone defects without rhBMP-2. Finally, the effect of a perforated nanofiber mesh design on bone repair was investigated. We hypothesized that rhBMP-2 delivery in the nanofiber mesh/alginate system would promote bone ingrowth and fully restore the mechanical properties of 8 mm segmental bone defects in the rat model. We further hypothesized that the perforated nanofiber mesh design would accelerate bone ingrowth due to enhanced early defect vascularization. We tested our hypothesis in an *in vivo* test bed model that utilizes quantitative techniques to assess differences in bone and vascular regrowth and restoration of mechanical function.

Materials and Methods

Fabrication of nanofiber mesh tubes

Poly (ε-caprolactone) (PCL) pellets (Sigma-Aldrich, St. Louis, MO) were dissolved in a 90:10 volume ratio of hexafluoro-2-propanol (HFP):dimethylformamide (DMF) (Sigma-Aldrich) to obtain a 12% (w/v) polymer solution. DMF was first slowly added to HFP to prevent excessive heat generation, and mixed well on a stir plate for 5 minutes. The PCL pellets were then added to the solvent solution, and gently stirred for 16-24 hours. The solution was visually inspected to ensure a homogeneous and clear solution. The polymer solution was loaded in a 3 mL syringe (Becton-Dickinson, Franklin Lakes, NJ), and a 22 gauge blunt stainless steel needle (Jensen Global Inc., Santa Barbara, CA) was attached to the syringe end. The syringe was mounted on a syringe pump (Harvard Apparatus, Holliston, MA) set at a rate of 0.75 mL/hr. The fibers

were collected on a flat copper plate (McMaster-Carr, Atlanta, GA) which was placed at a distance of 20-23 cm from the needle end. Fibers were electrospun for 5 hours at a voltage of 13-20 kV, supplied by a high voltage power supply (Gamma High Voltage Research, Ormond Beach, FL), to obtain a thick sheet of nanofiber mesh. The residual solvent from the meshes was allowed to evaporate by placing them in a dessicator overnight. The morphology of the nanofiber meshes was examined using a Scanning Electron Microscope (SEM; Hitachi HTA, Pleasanton, CA) after gold coating using a sputter coater (Quorum Technologies, East Granby, CT). The diameter of the fibers were quantified by analyzing the SEM images (at 7000magnification) using a custom MATLAB® (The MathWorks Inc., Natick, MA) code.

The nanofiber meshes, as fabricated above, were used to create tubular implants. Rectangular samples measuring 13×19 mm were cut from a mesh. In some samples, perforations spaced approximately 1.5 mm apart were made in the mesh using a 1 mm diameter biopsy punch (Miltex Inc., York, PA). The rectangular mesh samples were wrapped around a steel mandrel (McMaster-Carr) to form a tube having a diameter of approximately 5 mm and 13 mm length. The overlapping edges of the mesh were secured together by using UV glue (DYMAX Corporation, Torrington, CT), which was cured with a LED spot curing lamp (DYMAX Corporation). The nanofiber mesh tubes were then rinsed twice in 70% alcohol (VWR, West Chester, PA), and sterilized by submerging in 200 proof ethanol (Sigma-Aldrich) and allowing the ethanol to evaporate overnight. After the samples had dried completely, they were pre-wetted with sterile 70% ethanol for 30 minutes. After aspirating the 70% ethanol, the mesh tubes were rinsed three times with excess phosphate-buffered saline (PBS; Mediatech Inc., Manassas, VA), and placed in αMEM (Invitrogen) until implantation.

Preparation of alginate hydrogel with and without growth factors

Irradiated RGD-modified alginates were prepared as described previously [174]. Briefly, MVG sodium alginate (FMC Biopolymer) was subjected to a 5 Mrad dose of gamma irradiation. This reduces the molecular weight of the polymer leading to a faster degradation rate, which makes it more appropriate for *in vivo* studies [105]. The irradiated alginates were then covalently coupled with G_4RGDASSP peptide sequences (Commonwealth Biotechnologies, Richmond, VA) at a density of 2 sequences per polymer chain using standard carbodiimide chemistry [281]. The resulting RGD-alginates were sterile filtered, lyophilized and stored at -20°C.

To prepare hydrogels, the RGD-alginates were reconstituted in α-MEM to obtain a 2.5% (w/v) solution. Lyophilized rhBMP-2 (R&D Systems, Minneapolis, MN) was reconstituted in 0.1% rat serum albumin (RSA; Sigma-Aldrich) made in 4 mM HCl, at a concentration of 200-µg/mL. The alginate solution was then mixed with either the rhBMP-2 solution at a ratio 5:1 (700-µL alginate solution @2.5% (w/v) with 175-µL rhBMP-2 @200-µg/mL or 0.1% RSA). This results in a 2% (w/v) alginate solution containing 40-µg/mL rhBMP-2. The rhBMP-2 containing alginate solution was cross-linked with a calcium sulfate (Sigma-Aldrich) slurry (0.21 g $CaSO_4$ per 1 mL deionized water) at a ratio of 25:1 (35 µL of $CaSO_4$ with 875 µL of alginate/rhBMP-2 solution). The mixing was performed in two 1-mL syringes (Becton-Dickinson, Franklin Lakes, NJ) coupled with a syringe connector (Cole-Parmer, Vernon Hills, IL) with Luer-Lok fittings to minimize air bubbles. Another set of hydrogels was prepared without rhBMP-2 by substituting the rhBMP-2 solution with the carrier (0.1% RSA) alone. The alginate solutions were allowed to gel in the syringes for 30 minutes at room temperature and then transferred to 4°C. The hydrogels were kept at 4°C overnight and used in surgery the following day. Aseptic conditions were maintained in all the above steps, including handling of the exterior of the syringe.

rhBMP-2 release kinetics

RGD-alginate solutions containing rhBMP-2 were cross-linked with a calcium sulfate slurry as above, and immediately injected into custom designed molds containing 4 mm diameter wells. The alginate solutions were allowed to gel for 30 minutes at room temperature, producing cylindrical plugs measuring 4 mm in diameter and 8 mm in length. Each cylindrical alginate plug contained 500-ng rhBMP-2. Following a brief rinse in 0.1 M $CaCl_2$ (Sigma-Aldrich), the samples were incubated at 37°C in 1-mL PBS containing calcium and magnesium ions. At specific time points through day 21, the entire buffer solution was collected and replaced with fresh 1-mL PBS. On days 0 and 21, alginate plugs were dissolved by immersing in 8-mL and 2-mL, respectively, of 2% (w/v) sodium citrate (Sigma-Aldrich) for 30 minutes at room temperature. The amount of rhBMP-2 present in the collected PBS and sodium citrate solution was quantified using an ELISA kit (R&D Systems), following the manufacturer's instruction.

Surgical procedure and analysis

An established critically-sized, femoral segmental defect rat model was used in this study. All surgical procedures were approved by the Institutional Animal Care and Use Committee (IACUC protocol #A05041) at the Georgia Institute of Technology. The rat model and surgical technique has been described previously [74]. Briefly, bilateral 8 mm segmental defects were created in the mid femoral diaphyses of 13-week old female Sasco Sprague-Dawley rats. Prior to defect creation, the femora were stabilized by modular fixation plates consisting of a polysulfone plate and two stainless steel plates (Figure 5.1 E). This is a more challenging segmental defect model compared to the 5-6 mm defect models that are used most frequently in the field. Nanofiber mesh tubes were placed around the adjacent bone ends such that the tube lumen contained the defect and there was an overlap of 2.5 mm with the native bone ends at each end of the tube. In some groups, 125-µL pre-gelled 2% alginate with or without 5-µg rhBMP-2 was injected

in the tube lumen using a 22g needle (Jensen Global Inc.). As it is a soft hydrogel, the pre-gelled alginate is ejected from the needle in a continuous thin filament shape and fits compactly inside the tube. The tubes used for one of the groups had 1 mm diameter perforations to enhance vascular invasion during the repair process. The four groups (n=6-8) were as follows (Table 5.1): (I) Mesh alone, (II) Mesh with alginate, (III) Mesh with alginate containing rhBMP-2, (IV) Perforated mesh with alginate containing rhBMP-2. The groups were assigned to the right and left limbs to evenly distribute pairs of groups and obtain a balanced experimental design. After surgery, the animals were allowed to recover and move freely. For pain relief, the animals were injected with 0.03 mg/kg buprenorphine subcutaneously every 8 hours for the first 48 hours and 0.01 mg/kg buprenorphine for the next 24 hours. Radiographs and *in vivo* micro-computed tomography (μCT*)* images were obtained at 4 and 12 weeks after surgery to evaluate bone healing. The rats were euthanized at 12 weeks and femora were extracted for mechanical testing. Histological analysis was performed on femora extracted at 4 and 12 weeks.

Table 5.1. The four groups utilized in the *in vivo* study, with the implant conditions in each group.

Group #	Nanofiber mesh tube	Perforations	Alginate	rhBMP-2
I	+	–	–	–
II	+	–	+	–
III	+	–	+	+
IV	+	+	+	+

2-D radiographs and 3-D *in vivo* μCT imaging

At 4 and 12 weeks after implantation, two-dimensional radiographs (Faxitron MX-20 Digital, Faxitron X-ray Corp., Wheeling, IL) of the femur were taken to qualitatively assess bone regeneration and defect bridging. For the quantitative evaluation of bone formation, *in vivo* μCT was performed at the same time points. The rats were anesthetized by isoflurane and placed in an *in vivo* μCT system (Viva-CT, Scanco

Medical, Bassersdorf, Switzerland). The femoral defect region was scanned at a 38.5-µm voxel resolution, a voltage of 55-kVp and a current of 109-µA. The radiotranslucent polysulfone plate does not interfere with µCT scanning and therefore allows longitudinal evaluation of bone ingrowth. To obtain a consistent volume of interest (VOI) between animals and to avoid including the native bone ends, only the central 4 mm of the 8 mm defect was analyzed *in vivo* by drawing circular contours. A Gaussian filter (sigma = 1.2, support = 1) was used to suppress noise in the VOI, and a global threshold corresponding to a density of 270.3 mg hydroxyapatite/cm^3 was applied to obtain the regenerated bone volume. This threshold was selected by the visual inspection of individual scan slices to detect newly formed bone and to exclude soft tissues, the polysulfone fixation plate and the nanofiber mesh tube. The volume and density of the segmented bone was noted. In addition, the density map was calculated in the segmented bone volume, and presented as a pseudo color-scaled image.

Torsional testing

The freshly extracted femora at 12 weeks were wrapped in gauze moistened with PBS, and stored at -20°C. Just before testing, samples were thawed in PBS and the majority of soft tissues adjacent to the bone removed. The ends of the femur were embedded in end blocks using Wood's metal (Alfa Aesar, Wood Hill, MA) and aligned using a custom fixture. The polysulfone plate was then detached from the metal plates to enable loading of the bone. The potted femur was loaded into holding brackets mounted on a Bose ElectroForce system (ELF 3200, Bose EnduraTEC, Minnetonka, MN) fitted with a 2 Nm torsional load cell. The samples were rotated to failure at a rate of 3° per second under displacement control, and the torque and rotation were recorded. Maximum torque was calculated by locating the failure torque, which occurred within the first 15° for bridged defects. Samples that did not bridge displayed a gradual increase in torque and the absence of a sharp failure point, due to soft tissue stretching. For these samples,

the failure torque was measured in the first 60° to avoid analyzing the forces generated due to the stretching of soft tissues. Stiffness was calculated by finding the slope of the straight line fitted to the linear portion of the torque-rotation plot before failure.

Histological analysis

One representative sample from each group was selected for histological evaluation at 4 and 12 weeks. The extracted femora were fixed in 10% neutral-buffered formalin for 48 hours. They were dehydrated in a series of alcohol solutions of increasing concentrations, infiltrated with methyl methacrylate (MMA), and embedded by polymerizing the MMA. Ground sections, 50-80 μm thick, were generated using a EXAKT Grinding System (EXAKT Technologies, Oklahoma City, OK). The sections were stained with Sanderson's Rapid Bone Stain [282] and a van Gieson counter stain (SURGIPATH Medical Inc., Richmond, VA, USA). This stain permits the detection of bone (pink), muscle (blue green) and cells (blue).

Analysis of vascularity during bone regeneration

The vascular regrowth at the defect area was investigated at 3 weeks post-surgery by using a modified version of the μCT–based angiography technique developed in our laboratory [278, 283]. After induction of anesthesia using isoflurane, a 25 gauge catheter was introduced into the abdominal aorta and 250 units (0.25 mL of 1000 units/mL) heparin were injected. The rat hind limb vasculature was cleared with PBS, fixed with 10% neutral buffered formalin and cleared again with PBS using a peristaltic pump (Masterflex, Cole-Parmer). The rats were euthanized by an overdose of isoflurane before the formalin perfusion. A radiopaque, lead chromate based contrast agent (Flow Tech, Carver, MA) was then injected and allowed to polymerize for at least two hours. The femur along with its musculature was excised carefully, fixed in 10% neutral buffered formalin for 48 hours, and decalcified for 2 weeks using a formic acid based solution

(Cal-Ex II, Fisher Scientific). The samples were rinsed in PBS and stored in 10% neutral buffered formalin until imaging. They were imaged in a μCT system (Viva-CT, Scanco Medical) at a 21.5-μm voxel size. Two VOIs were defined to analyze the vessels inside the defect and adjacent to the defect. The images were globally thresholded based on X-ray attenuation to segment the contrast-filled vasculature from surrounding tissues.

Statistical analysis

Data were analyzed by analysis of variance (ANOVA) conducted in Minitab® 15 (Minitab Inc., State College, PA). Pairwise comparisons were made using the Tukey multiple comparison procedure. The normality of the residuals was evaluated by the Anderson-Darling normality test. To detect the presence of any pattern in the residual distribution, they were plotted against fitted values. To maintain the constancy of error variance and normality of error terms, data were transformed according to the Box-Cox procedure, wherever required [221, 222]. To investigate the effect of time on sequential *in vivo* μCT data, paired t-tests were performed. A p-value < 0.05 was considered statistically significant. All data are shown as mean ± standard error of mean (SEM).

Results

Nanofiber mesh tube characterization and placement

The nanofibers obtained by electrospinning were observed to be smooth and bead-free (Figure 5.1 A). The fibers ranged in diameter from 51 nm to 974 nm with 82% of the fibers between 50 nm and 150 nm. The mean and the median fiber diameter were found to be 154 nm and 107 nm respectively. After 5 hours of electrospinning, the mesh was found to be approximately 300-400 μm thick. This thickness was sufficient to provide a bending stiffness that prevented collapse of the mesh in solution. The thick nanofiber meshes were able to be wrapped tightly around a steel mandrel, and glued to form a tube (Figure 5.1 B and C). Due to the fast curing time of the UV glue, it was

localized to the overlapping edges and did not seep to the rest of the mesh. The perforated meshes held the tubular structure well, and the holes accounted for 10% of the total surface area of the mesh tube. The nanofiber mesh tubes were deformed slightly to place them around the native bone ends of the segmental defect, but they regained their original shape due to the elasticity of the mesh. The overlapping ends and the surrounding musculature resulted in the tubes being stably located around the defect for the duration of the study (Figure 5.1 D and E). In some samples that were taken down after one week, the alginate was found to be still present inside the tube lumen, even in perforated tubes, with hematoma formation at the bone ends (Figure 5.1 F).

Alginate release kinetics

The *in vitro* release of rhMBP-2 from alginate hydrogel plugs was monitored over a period of 21 days (Figure 5.1 G). After dissolving the alginate plugs on day 0, 275.5 ± 15.6 ng rhBMP-2 was detected in the resulting solution, indicating that the functional encapsulation percentage was 55.1%. Of the amount encapsulated, 25.8% (71.2 ± 3.8 ng) was released in the buffer solution in active form by day 21. The majority of the release took place within the first 7 days (98.6% of total released). We also assayed for the amount of rhBMP-2 retained in the gels by dissolving them at day 21, and found that 9.9% (27.2 ± 3.3 ng) of the encapsulated amount was still present in the gels. It is possible that the binding of some of the rhBMP-2 molecules to the alginate fibers masks the antibody binding site. This subset of rhBMP-2 molecules would not be detected by the ELISA, and therefore the actual amount of rhBMP-2 present in the hydrogels may be higher.

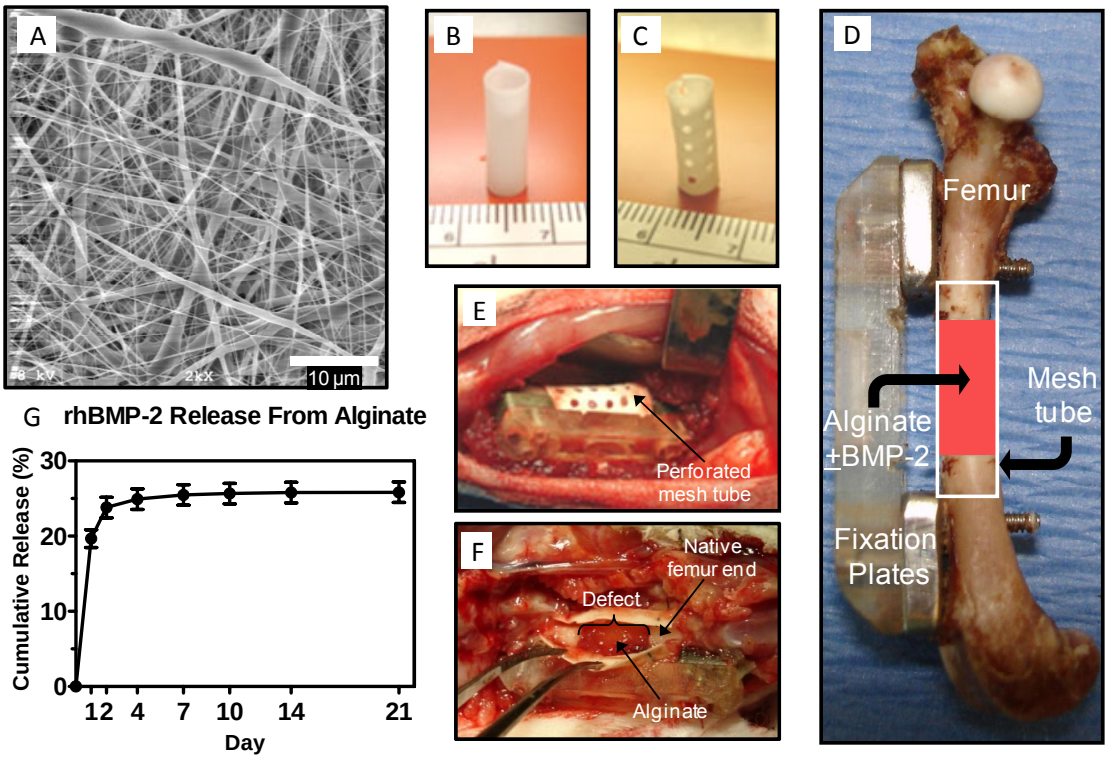

Figure 5.1. Nanofiber mesh tubes and alginate hydrogel for surgery. (A) SEM image of electrospun nanofiber mesh illustrating the smooth and bead-free nano-scaled fibers. (B) Hollow tubular implant without perforations made from nanofiber meshes. (C) Tubular implant with perforations. (D) Implants in segmental bone defect. Modular fixation plates are used to stabilize the femur. A nanofiber mesh tube is placed around the 8 mm defect. In some groups, alginate hydrogel, with or without rhBMP-2 is injected inside the hollow tube. (E) Picture of defect, after placement of a perforated mesh tube. The alginate inside the tube can be seen through the perforations. (F) A specimen was taken down after 1 week and the mesh tube was cut open. The alginate was still present inside the defect, with hematoma present at the bone ends. (G) Alginate release kinetics over 21 days *in vitro*. Sustained release of the rhBMP-2 was observed during the first week.

Radiographs

Two-dimensional radiographs were taken at 4 and 12 weeks for qualitative assessment of bone healing (Figure 5.2). Radiographs at the early time point of 4 weeks indicated that Groups I & II (Table 1) specimens had small amounts of bone formation, originating from the cut native ends and extending somewhat along the periphery. Group I samples were implanted with a nanofiber mesh tube alone, whereas Group II contained, in addition, alginate hydrogel inside the mesh tube. On the other hand, samples from Groups III and IV, in which 5-µg rhBMP-2 was delivered within alginate, demonstrated significant infiltration of mineralized tissue throughout the defect. Group IV specimens that were implanted with the perforated mesh tube exhibited the most robust mineralization. Group IV demonstrated the highest bridging rate (5/8) at the 4 week time point, whereas the remaining 3/8 defects were nearly bridged. Group III had none bridged, but 3/6 defects were nearly bridged. At 12 weeks, Groups I and II had still not achieved osseous union in any specimen, with most of the bony tissue formed on the periphery. In contrast, all specimens in Groups III and IV were completely bridged with densely packed bone.

***In vivo* µCT imaging**

Animals were scanned in an *in vivo* µCT system at 4 and 12 weeks for quantifying bone formation (Figure 5.3). The three-dimensional µCT images revealed that new bone formation in Groups III and IV occurred throughout the cross-section of the defect, whereas it appeared predominantly at the native bone margins and the periphery in Groups I and II (Figure 5.3 A). The analysis of regenerated bone volumes indicated that Groups III and IV (Table 1) had significantly more (a; $p<0.05$) bone formation in the defect compared to Groups I and II, at both time points (Figure 5.3 B). At 4 weeks, Group IV, implanted with the perforated mesh, had significantly more (b; $p<0.05$) bone formation than Group III, which contained the mesh tubes without holes.

However at 12 weeks, there was no difference in bone volumes between Groups III and IV. There was a significant increase in bone volumes with time in Groups I ($p = 0.048$), III ($p < 0.001$) and IV ($p = 0.001$), but not in Group II ($p = 0.08$). Group III (37.65 ± 2.22 mm^3) samples demonstrated the greatest increase in bone volume between 4 and 12 weeks, followed by Group IV (20.02 ± 2.96 mm^3). Compared to these two groups, Groups I (3.96 ± 1.40 mm^3) and II (2.09 ± 0.80 mm^3) had significantly less bone accumulation during the same period.

The density of the newly formed bone within the defect was also calculated at 4 and 12 weeks (Figure 5.3 C). At 4 weeks, Groups I and II contained higher density bone than Groups III and IV (b and c respectively; $p<0.05$). Group IV samples demonstrated a density higher than Group III, at both 4 and 12 weeks (b; $p<0.05$). There was a significant increase in density with time for all groups from 4 to 12 weeks.

Biomechanical properties

Torsional testing was performed on extracted femora at 12 weeks to test their biomechanical properties (Figure 5.4). Age-matched non-operated femora were also tested to obtain properties of native intact bone. The maximum torque and stiffness in torsion was calculated from the torque-rotation data. Groups III and IV had significantly higher (a; $p<0.01$) maximum torque and stiffness compared to Groups I and II, as did the intact bone. There was no significant difference between Groups III and IV. However, compared to the intact bone, only Group IV samples had statistically equivalent maximum torque and stiffness, whereas Group III samples had significantly lower properties (b; $p<0.05$). The mechanical properties for Group IV were on average approximately 75% of those for intact bone.

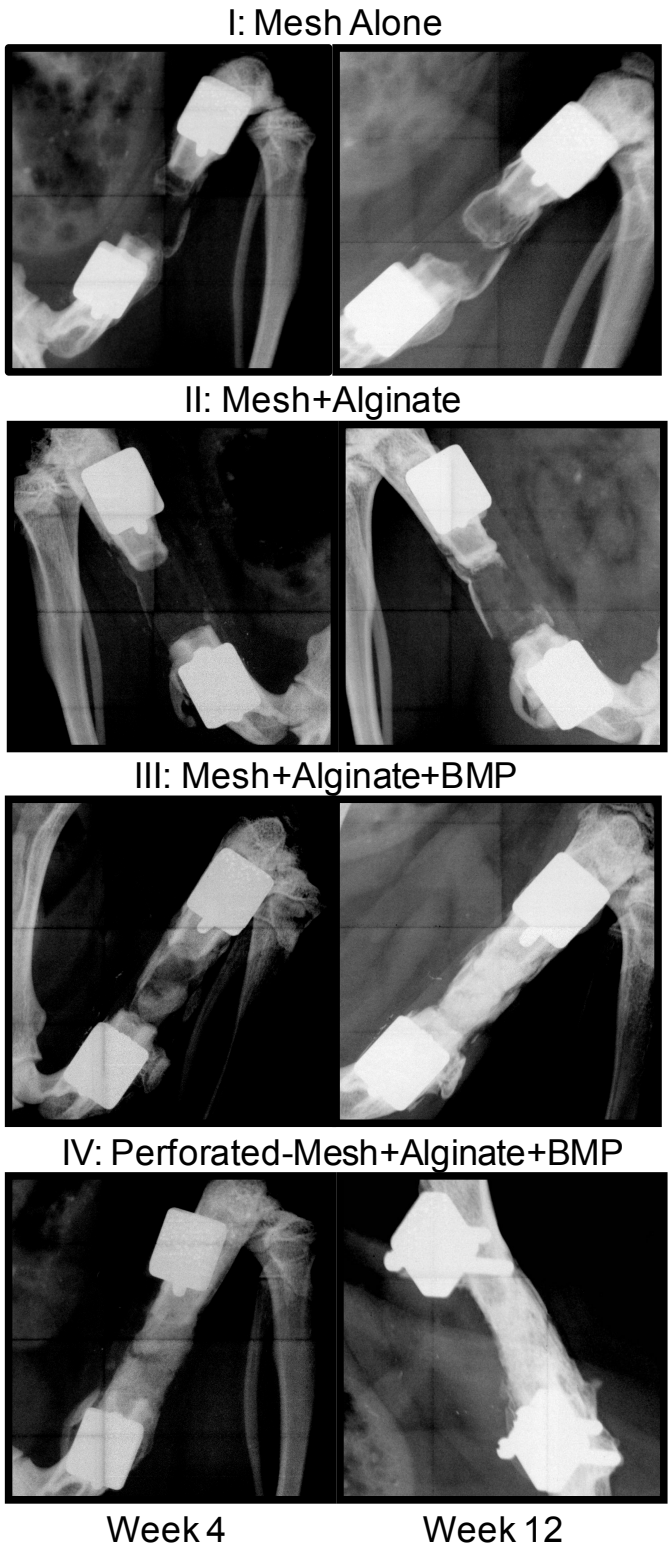

Figure 5.2. Representative radiographs at 4 and 12 weeks. Defects in Groups I and II demonstrated small amount of bone formation, and did not bridge, even after 12 weeks. At week 4, defects in Groups III samples were infiltrated with considerable bony tissue, while Group IV samples exhibited the most robust mineralization. All samples in Groups III and IV were bridged with densely packed bone at week 12.

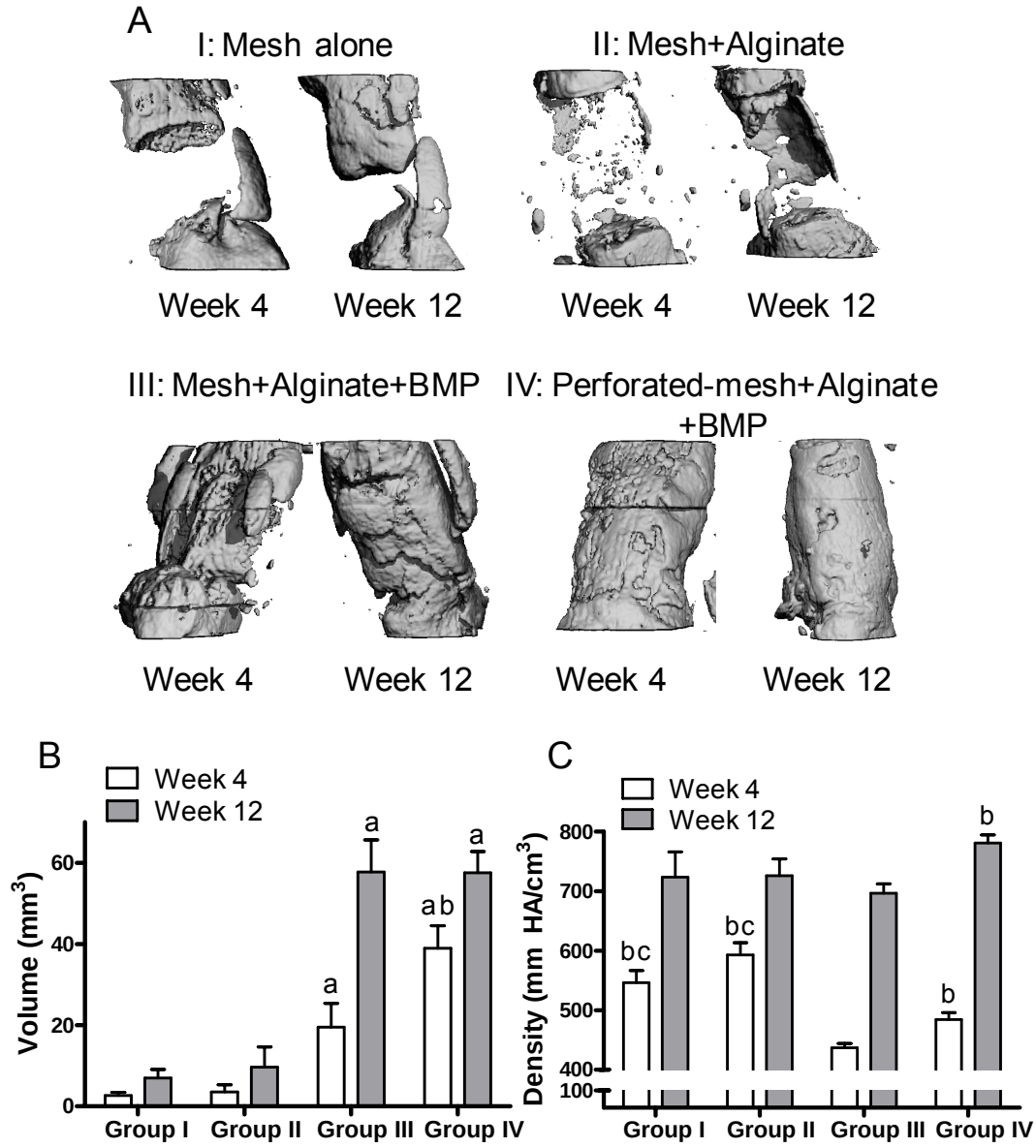

Figure 5.3. μCT analysis of bone regeneration at 4 and 12 weeks. (A) μCT images illustrate that defects in Groups III and IV were filled with newly formed bone, while those in Groups I and II possessed limited new bone at the native bone ends and the defect periphery. (B) Quantification of regenerated bone volume revealed that the rhBMP-2 groups (Group III and IV) had significantly more bone formation than the groups without rhBMP-2 (Groups I and II), at both 4 and 12 weeks. Perforations in the nanofiber mesh tubes accelerated bone formation at 4 weeks (Group IV > Group III). (C) Mean density of regenerated bone. At week 4, samples in Groups I and II demonstrated higher density than the other two groups. Density of Group IV samples was higher than those in Group III, at both time points. (a – significantly different than Groups I and II; $p<0.05$); (b – significantly different than Group III; $p<0.05$).

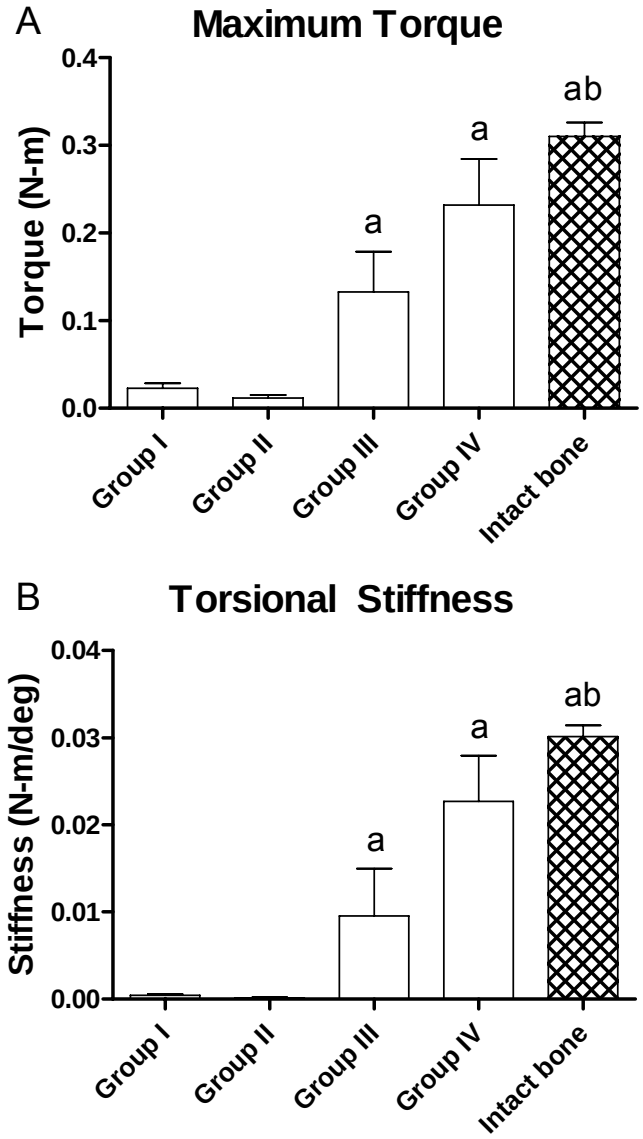

Figure 5.4. Mechanical properties of femora at 12 weeks. (A) Maximum torque and (B) torsional stiffness. Mechanical properties in Groups III and IV were significantly higher than in Groups I and II. Compared to intact bones, Group III samples had significantly lower properties, whereas Group IV samples were statistically equivalent. (a – significantly different than Groups I and II; $p<0.01$); (b - significantly different than Group III; $p<0.05$). (I) Mesh alone, (II) Mesh with alginate, (III) Mesh with alginate containing rhBMP-2, (IV) Perforated mesh with alginate containing rhBMP-2.

Histological analysis

Ground MMA sections were stained and analyzed for examining the regenerated tissue (Figure 5.5 A and B). The nanofiber mesh tube was partially degraded due the MMA processing steps, but is still seen to be located around the defect. In Groups I and II, very little mineralized tissue was observed in the defect site at 12 weeks, similar to the radiographic and μCT results (Figure 5.5 A: I and II). The defects in these specimens were sparsely populated with fibrous tissue. The new bone formation was limited to the proximity of native bone ends and along the mesh tube. The end of the defects remained disconnected, with the capping of the native ends with bony tissue. The sections from Groups III and IV revealed extensive mineral deposition and bony bridging of the defects in these groups (Figure 5.5 A: III and IV). The newly formed bone was observed to be a combination of immature woven bone and mature lamellar bone. There was good continuity of the newly mineralized matrix with the native bone ends. Group IV, in particular, demonstrated the presence of a higher amount of lamellar bone, better integration at the native bone interface and development of marrow-like tissue. The dark areas correspond to undegraded alginate and the partially degraded mesh. The higher magnification images of Groups III and IV indicated the presence of osteocytes embedded in lacunae and osteoblasts lining the new bone surfaces (Figure 5.5 B). Histological analysis performed at 4 weeks revealed no evidence of cartilage tissue formation or endochondral ossification, indicating direct, intramembranous bone formation within the alginate gel (data not shown). The density maps obtained from the μCT indicate good correlation with histology sections (Figure 5.5 C). In addition, Group IV appeared to contain higher density mineralized tissue, which was distributed in a tubular pattern, similar to that of native cortical structure.

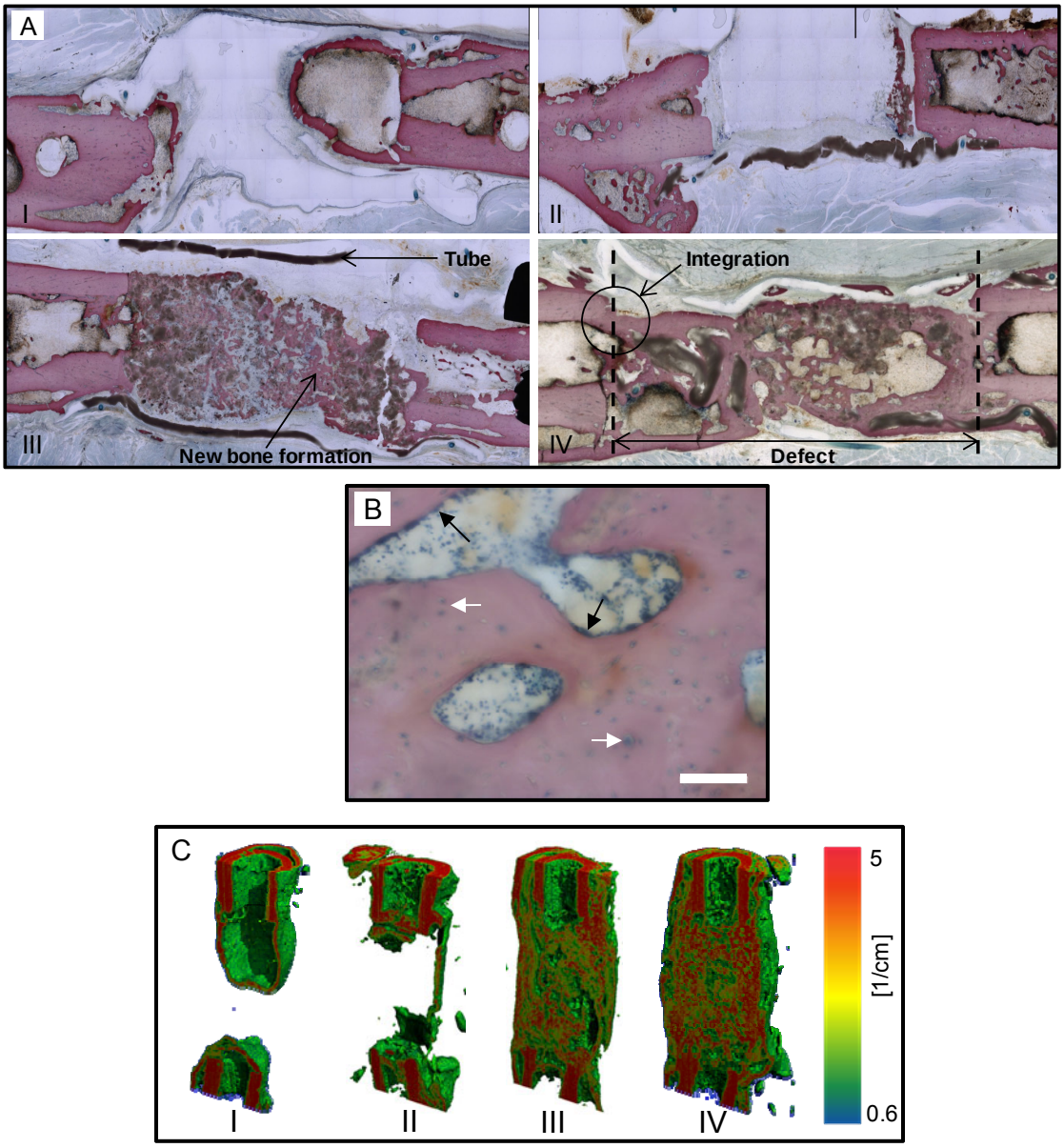

Figure 5.5. Histological analysis at 12 weeks. (A) Ground sections were stained with Sanderson's rapid bone stain at 12 weeks (4X magnification). Defects in Groups I and II were sparsely populated with fibrous tissue, with the native ends capped with bony tissue. Defects in Groups III and IV had extensive bone deposition throughout the defect, with Group IV samples demonstrating better integration with the native bone. (B) Higher magnification section, representative of the newly formed bone in Groups III and IV (10X magnification). White arrows point to osteocytes embedded in lacunae. Black arrows point to osteoblasts lining the bone surface. Scale bar is 100 µm. (C) Density maps obtained from the µCT analysis at 12 weeks indicate good correlation with histology sections. The color scale to the right correlates to the attenuation of bone. Red color indicates higher density bone (higher attenuation), whereas green color represents lower density bone (lower attenuation). Compared to Group III, Group IV samples contained higher density bone, distributed along the native cortices. (I) Mesh alone, (II) Mesh with alginate, (III) Mesh with alginate containing rhBMP-2, (IV) Perforated mesh with alginate containing rhBMP-2.

μCT–based angiography

Animals implanted with the rhBMP-2 containing Groups III and IV were euthanized at 3 weeks post-implantation, and their hind limb vasculature perfused with a radiopaque contrast agent. The femur and the surrounding soft tissues were imaged using μCT to quantify vascular ingrowth at an early time point preceding bone regeneration. Contours were drawn to define two VOIs. The first VOI included only the volume inside the defect region, whereas the second contained both the defect and the periphery of the defect, termed the total VOI (Figure 5.6). The analysis of the vasculature revealed the presence of vessels, both inside and outside the defect. The majority of the vascularity was observed in the periphery, as indicated by the significantly larger vessel volume in the total VOI (a; $p<0.001$). There were no significant differences in vascular volume between Groups III and IV, in either the defect or the total VOI.

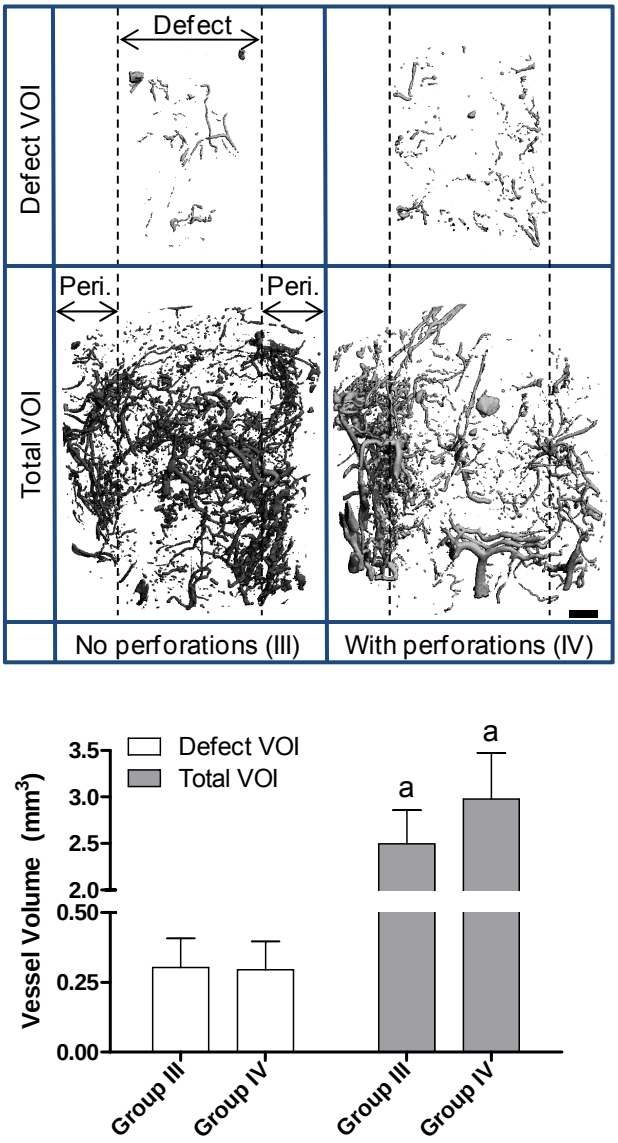

Figure 5.6. Vascular ingrowth at defect site at 3 weeks. Only Groups III and IV were included in this experiment. The defect VOI contains only the defect volume, whereas the total VOI contains the periphery of the defect in addition to the defect. The vascular volume was found to be significantly higher in the total VOI compared to the defect VOI. No significant differences were observed in the presence of perforations. Scale bar is 1 mm and applies to all images. Peri. – periphery of defect. (a – significantly different than the defect VOI; $p<0.001$). (III) Mesh with alginate containing rhBMP-2, (IV) Perforated mesh with alginate containing rhBMP-2.

Discussion

The treatment of large osseous defects remains a challenge for orthopaedic surgeons. We have developed a novel growth factor delivery technique for the functional repair of large bone defects using an electrospun nanofiber mesh tube and alginate hydrogel. Tubular scaffolds constructed from nanofiber meshes were placed around segmental defects. Alginate hydrogel containing 5-µg rhBMP-2 was injected into the tubes and constrained within the defect site by the mesh tube. Our results demonstrate that this technique results in substantial bone formation and complete defect bridging. Importantly, samples implanted with both perforated mesh tube and rhBMP-2 containing alginate had statistically equivalent biomechanical properties to those of intact age-matched femora, indicating functional restoration of the limb function.

The majority of scaffolds proposed for bone reconstruction are structural scaffolds designed to support *in vivo* loads and provide a three-dimensional framework for cell attachment. They are examples of "hard scaffolds", usually made from slowly hydrolyzing polymers or ceramics with unpredictable degradation [65, 87, 125]. Though they provide a structure for tissue growth, it is difficult to fine-tune their degradation rate to match the rate of tissue formation. Oest et al. reported that the use of such a scaffold hindered complete bone restoration by occupying space and confining the bone formation to the pores and the periphery of the scaffold [74]. The use of structural scaffolds also precludes the use of the intramedullary pin for limb fixation, a technique frequently used by orthopaedic surgeons. In addition, the regular geometric shape of these scaffolds made them unsuitable to be placed inside fractures, which usually have irregular edges. Thin scaffold membranes have also been used for bone repair in a procedure termed guided bone/tissue regeneration [175, 179]. In this technique, the membranes are positioned on the periosteal surface to provide a structure for bone formation. It has been argued that while 3-D scaffolds support the ingrowth of cells and tissue, the 2-D membranes may also protect the defect from soft tissue ingrowth and guide cell migration from the

periosteum [92, 182]. Since the membranes are placed on the periphery of the defect, they retain space for bone deposition throughout the defect. However, when a large mass of bone is lost, repopulating the entire defect with cells would be a challenge due to the presence of a large void.

Hydrogels are a class of highly hydrated materials that enable cellular and tissue infiltration with relative ease [164]. Alginate hydrogels are an example of such a "soft scaffold" that can deployed using minimally invasive procedures, conform to the shape of the defect and be manipulated by cells during tissue regeneration [165]. In addition, they can be used for sustained delivery of osteoinductive growth factors, a typical requirement for healing large defects. The primary concern with hydrogels is their inadequate mechanical stiffness, which causes them to deform easily under load.

In this study, we present a novel hybrid technique that utilizes both a nanofiber mesh membrane and an alginate hydrogel. The mesh tubes prevent soft tissue invagination into the defect and create a space for tissue regeneration. In addition, they potentially guide the migration of progenitor cells along the periosteal surface, and retain the osteogenic factors within the defect site. However, nanofiber mesh tubes, alone or in presence of alginate hydrogel without rhBMP-2, were not sufficient to bridge the 8 mm segmental defects in rat femora. Without the presence of the osteoinductive protein, the center was only sparsely populated by cells and bony tissue capped the ends of the defect. This is not surprising, since previous studies have demonstrated the need for a biologic stimulus for effective bone regeneration in this challenging model [74, 278]. A series of studies have been performed to investigate the ability of polymer membranes to heal segmental diaphyseal defects [92, 181, 182, 284]. Pineda et al. implanted porous polylactide membranes thermoformed into tubes in 1-cm defects in the rabbit radius, and observed bridging with new endosteal bone generation from the native bone ends [182]. However, in more challenging defects in the sheep tibia, bone grafting or a vascularized periosteal flap was needed, in addition to a membrane, to heal the defect [93, 183].

In contrast, we found significantly higher bone formation with the sustained release of rhBMP-2 from the alginate hydrogel. All defects in the rhBMP-2 groups (Groups III and IV) were bridged by 12 weeks with densely packed, cell mediated mineralized tissue. This suggests that the release of rhBMP-2 is able to attract osteoprogenitor cells into the defect from the adjacent periosteum, marrow and vascularized tissues, and induce them to undergo osteogenic differentiation. The release of proteins from alginate occurs due to a combination of diffusion and gel degradation. It is interesting to note that after 21 days, at least 10% of the functionally encapsulated rhBMP-2 was still present in the alginate, though the amount of the protein released at this time point was negligible. This suggests that a portion of the protein binds to the alginate polymer, which at later time points may be available to the invading cells. It has been reported that alginate can reversibly bind proteins like BMP-2 through heparin-binding domains [285]. The binding of the protein to alginate could be an advantage, as this is thought to enhance the biological activity of the protein, perhaps by protection from premature degradation [286], and maintain a spatial cue during the tissue regeneration process. The RGD functionalized alginate used in this study also supported the robust penetration of osteogenic cells and tissue resulting in functional restoration.

The presence of perforations in nanofiber mesh tubes accelerated early bone formation and defect bridging. The utilization of *in vivo* μCT scanning techniques permitted the sequential scanning of animals at multiple time points, and revealed that perforations in mesh tubes enhanced bone formation at 4 weeks. However, by 12 weeks, the group without perforations (Group III) had comparable bone volume to the group with perforations (Group IV). The differences in the bone deposition rate between 4-12 weeks could be attributed to the fact that at week 4, Group IV defects were almost filled with newly formed bone, whereas Group III defects still exhibited substantial space for bone formation. Compared to Group III, the density of the newly formed bone was significantly higher in Group IV. Also, only Group IV femora demonstrated functional

restoration of biomechanical properties. These results indicate that perforations in the nanofiber mesh tube expedited bone formation, resulting in advanced bone remodeling and improved mechanical properties. Gogolewski and coworkers used a perforated membrane along with autologous bone graft for treating segmental defects in sheep tibiae, and concluded that the perforations improved bone regeneration by enhancing graft survival [93, 183]. They hypothesized that the perforations allow sufficient vascularization to develop, while limiting soft tissue ingrowth.

There are two potential mechanisms that mediate the acceleration of bone formation due to perforations in our hybrid delivery system. The perforations may enhance invasion of vascularity or improve osteoprogenitor cell migration from the surrounding soft tissues into the defect region. We initially hypothesized that perforations improve vascular invasion, and employed a μCT-based technique to quantitatively assess the vascularity in the early stages of bone regeneration [287]. However, our results indicated that the perforations did not have a significant effect on vascularity at the defect site. In addition, it was seen that only a fraction of the total vessels were present inside the defect. It is possible that the scan resolution was too low to detect the microvasculature in the developing bone [288]. The lack of differences in vascular regrowth due to the perforations suggests that the acceleration of bone formation was due to improved osteoprogenitor cell migration into the defect.

The current clinical technique for rhBMP-2 delivery involves soaking a collagen sponge with rhBMP-2 solution, which primarily relies on the adsorption of the protein to collagen [241]. Numerous sustained delivery systems are being currently developed from natural and synthetic materials for reducing the high rhBMP-2 dose required clinically [91, 100, 289-292]. For example, Johnson et al. obtained the sustained release of rhBMP-2 without a large burst release by utilizing lipid-based microtubes [289]. A gelatin hydrogel engineered for the sustained released of rhBMP-2 resulted in the repair of a large ulnar defect [293]. On the other hand, Rizzi and co-workers reported that the

physical linkage of rhBMP-2 to a recombinant protein-poly(ethylene glycol) hydrogel prevented optimal bone healing of murine cranial defects [169]. This was attributed to the inability of the bound rhBMP-2 to be released to provide a chemotactic signal and the insufficient degradation of the hydrogel matrix. By providing a sustained and localized release of rhBMP-2 and permitting robust cell infiltration, the hybrid alginate/nanofiber mesh system creates an environment conducive for bone regeneration. The 5-μg dose utilized in this study is in the lower range of what has been reported (2-20 μg) in similar models [74, 91, 294, 295]. For example, in a 8 mm rat segmental defect model, 20-μg of rhBMP-2 delivered on inactive dimineralized bone matrix was required for defect bridging [294]. Future studies will compare our hybrid system with the clinically used rhBMP-2 delivery technique to determine the effect of alginate/nanofiber mesh delivery on bone repair.

In conclusion, a novel hybrid growth factor delivery system was presented in this study. This system resulted in complete bony bridging of challenging segmental bone defects in a rat model. Perforations accelerated the deposition of mineralized tissue, and resulted in functional repair, by perhaps improving osteoprogenitor cell migration into the defect. The mesh tube alone, or in combination with alginate hydrogel, did not generate a strong repair response. The sustained delivery of rhBMP-2 via alginate hydrogel was required for substantial regeneration to occur. These results indicate that this hybrid technique may be clinically useful for bone regeneration in the case of fracture non-unions and large bone defects.

CHAPTER 6

DELIVERY OF BONE MORPHOGENETIC PROTEIN WITHIN NANOFIBER MESH/ALGINATE ENHANCES SEGMENTAL BONE DEFECT REPAIR

Introduction

Large bone defects caused by trauma, tumor resection or disease present a significant clinical problem. Current treatments include autologous and allogeneic bone grafting, and more recently ceramic and composite substitutes for these [45, 48, 49]. Autologous bone grafting remains the gold standard for bone healing because of the rich biologic environment it provides, but this treatment modality is limited by the amount of graft material available [49, 53]. Furthermore, morbidity of the donor site is a serious drawback [52]. Structural allografts have been used as an alternative, but are unable to support revascularization and remodeling, and therefore are associated with a high rate of complications [54-56]. Bone graft substitutes, made from ceramics or polymers, suffer from limited bioactivity, and usually need to be supplemented with osteogenic cells or bone graft material [51]. There is, therefore, a tremendous need to find alternatives to these treatment options, and biomimetic materials and molecules, which can recruit endogenous progenitor cells and provide osteogenic cues, represent a new and promising class of therapies for bone repair.

The role of bone morphogenetic proteins (BMPs) in bone formation has been studied extensively (for reviews, see [19, 29]). BMPs are necessary for fetal tissue development as well as for fracture repair [30, 31, 296, 297]. BMPs are present primarily in native bone tissue, and serve to attract progenitor cells to the defect site and promote their osteogenic differentiation. In the last decade, recombinant human bone morphogenetic protein-2 (rhBMP-2) and rhBMP-7 have been approved by regulatory

bodies worldwide for spinal fusion, oral-maxillofacial applications and the treatment of certain fractures, [101, 241]. However, challenges remain due to the suboptimal delivery vehicles, poor spatiotemporal dosage control, short protein half-life, and the cost-restrictive supraphysiologic concentrations required to initiate cellular responses [63, 143, 147]. Currently, osteoinductive proteins are delivered in solution on a purified type I collagen matrix. However, high doses (3.5 – 12 mg) are required for obtaining a substantial healing response. The high doses have resulted in complications arising due to diffusion of the BMP away from the defect site [60, 61, 144], and the high cost has prevented this treatment from being used routinely [62, 63].

Due to the limitations of the current BMP delivery technique, numerous biomaterial-based sustained delivery vehicles are being developed to improve protein pharmacokinetics *in vivo* [289, 290, 293, 298]. Spatial distribution of the protein is also important to maximize efficacy and minimize side effects. In a previous study, we demonstrated that a hybrid BMP delivery system using an electrospun nanofiber mesh tube and alginate hydrogel results in the functional repair of large bone defects (Chapter 5). In this technique, a nanofiber mesh tube is used to cover the defect region and RGD-functionalized alginate hydrogel that contains BMP is injected inside the tube. The alginate provides sustained availability of the growth factor and supports cell infiltration into the defect space, while the nanofiber mesh aids in retaining the hydrogel and growth factor within the defect site.

The purpose of this study was to compare the hybrid nanofiber mesh/alginate BMP delivery technique with the clinical standard of BMP delivery on collagen matrix. In addition, the role of the nanofiber mesh tube as a spatial constraint was investigated. Our hypotheses were that BMP delivery within alginate hydrogel would enhance bone formation, and that the mesh tube would aid in the spatial retention of the regenerated bone. To test this hypothesis, we evaluated the structural and biomechanical properties of the regenerated bone in a challenging rat segmental defect model.

Materials and Methods

Nanofiber mesh tube fabrication and alginate preparation

Nanofiber meshes were made by electrospinning and formed into tubes as described in Chapter 5. Briefly, a 12% (w/v) solution of poly (ε-caprolactone) (PCL) was made by dissolving the polymer in a 90:10 volume ratio of hexafluoro-2-propanol:dimethylformamide. The following parameters were used during electrospinning: flow rate: 0.75 mL/hr; voltage: 13 kV; collector distance: 17 cm; needle gauge: 22. Fibers were collected for 6 hours to obtain nanofiber meshes having a thickness of approximately 300-400 μm. Perforations measuring 1 mm in diameter and spaced approximately 1.5 mm apart were made in rectangular 13×19 mm mesh samples using a biopsy punch. The mesh samples were wrapped around a steel mandrel and glued using UV glue (DYMAX Corporation, Torrington, CT) to form hollow tubular implants having a diameter of approximately 5 mm and 13 mm length.

Medical grade alginate, MVG (FMC Biopolymer, Philadelphia, PA), was irradiated with a 5 Mrad dose of Gamma irradiation, and covalently coupled with RGD-containing G4RGDASSP peptide sequences. Alginate hydrogels, encapsulating 33.33 μg/mL rhBMP-2, were prepared in 1 mL syringes at a concentration of 2% (w/v) by crosslinking the alginate with calcium sulfate slurry (Chapter 5). For one of the experimental groups, the hydrogels were made in the form of cylindrical plugs (Ø5 mm; 9 mm length) by using a custom built mold.

Animal model and bone regeneration analysis

A previously described segmental defect animal model [74] was employed to compare three different rhBMP-2 delivery methods. Briefly, femora of 13 week old female Sasco Sprague-Dawley rats were stabilized with custom fixation plates. Bilateral 8 mm segmental defects were created in the mid femoral diaphyses with an oscillating

saw under irrigation. A 5 μg dose of rhBMP-2 was delivered to each defect in one of three different ways shown in Table 6.1. In Group I, a collagen scaffold (Ø5 mm; 9 mm length) was soaked with 150 μL of 33.33 μg/mL rhMBP-2 solution for 15 minutes, and implanted in the defect. The collagen scaffolds were obtained from a fibrous collagen sheet (average pore size 61.7 μm, 93.7% pore volume, Kensey Nash, Exton, PA). Group II implants consisted of a cylindrical scaffold (Ø5 mm; 9 mm length) made from alginate containing 5 μg rhBMP-2. In Group III, perforated nanofiber mesh tubes were placed around the defect, and injected with 5 μg rhBMP-2-containing alginate using a 22g needle.

Radiographs and μCT images of 8-10 samples per group were obtained at 4 and 12 weeks to assess bone formation. Radiographs were also taken at 2 weeks to assess early differences between groups. In addition to the volume of newly formed bone at each time point, μCT data was processed to obtain mean density, connectivity density and temporal changes in volume of the regenerated bone. Based on the two dimensional scan slices, an appropriate threshold was selected at each time point to detect new bone formation.

Torsional testing was performed on extracted femurs at 12 weeks using a Bose ElectroForce system (ELF 3200, Bose EnduraTEC, Minnetonka, MN) to test their biomechanical properties. Maximum torque and failure angle were measured at the failure point from the torque-rotation data, and the work to failure was calculated using these values. Torsional stiffness was calculated by fitting a straight line to the linear portion of the curve before failure. Histological analysis was also performed at 12 weeks by embedding decalcified femurs in glycol methacrylate (GMA) and staining 5 μm sections with H&E.

Data analysis

Data are presented as mean ± standard error of mean (SEM). Data were analyzed using ANOVA and Tukey's tests for pairwise comparisons (significance set at $p<0.05$). When data were not normal, the nonparametric Mann-Whitney test was used to compare between groups. Minitab® 15 (Minitab Inc., State College, PA) was used for all statistical analysis.

Table 6.1. Experimental groups

Group	Description
Group I	Collagen scaffold + 5µg rhBMP-2
Group II	Alginate scaffold + 5µg rhBMP-2
Group III	Perforated nanofiber mesh tube + Alginate + 5µg rhBMP-2

Results

Radiographs

The radiographs at the early time point of 2 weeks illustrated that, while considerable new bone deposition was evident in the collagen scaffold group (Group I), the alginate groups (Groups II and III) demonstrated comparatively less bone formation (Figure Figure 6.1). In contrast, the radiographs at 4 and 12 weeks revealed that the alginate groups exhibited higher amount of bone, though there was substantial bone regeneration in all groups at 4 weeks and bridging of all defects after 12 weeks. In addition, there were differences in the distribution and density of bone deposition among groups. Group I samples appeared to have more trabecular-like bone that was not as densely packed as the other two groups. Group II demonstrated mineral deposition both within and outside the defect, suggesting some alginate scaffold displacement or protein diffusion. In contrast, samples in Group III exhibited consistent localization of dense new bone formation inside the defect.

Figure 6.1. Representative radiographs at 2, 4 and 12 weeks. At 2 weeks, Group I specimens possessed more bony tissue in the defect than Groups II and III. However, at 4 and 12 weeks, Group II and III defects demonstrated qualitatively higher bone formation. All defects in the three groups were bridged with bony tissue by 12 weeks. The newly formed bone in Groups II and III appeared more densely packed that Group I. Note that the new bone formation was better contained within the defect in Group III, with the nanofiber mesh tube. (I) Collagen scaffold + rhBMP-2, (II) Alginate scaffold + rhBMP-2, (III) Perforated nanofiber mesh tube + Alginate + rhBMP-2.

μCT analysis

The three-dimensional μCT images obtained in vivo at 4 and 12 weeks were consistent with the radiographs (Figure Figure 6.2). The collagen scaffold group (Group I) demonstrated substantial bone formation in the defects by 4 weeks. Specimens in the alginate scaffold group (Group II) exhibited a fragmented distribution of mineralized tissue, with substantial bone formation occurring outside the defect region. In contrast, in the presence of a nanofiber mesh tube (Group III), new bone formation was confined within the defect region and displayed a continuous distribution.

μCT analysis determined that the amount and distribution of regenerated bone was significantly affected by the rhBMP-2 delivery method. Two volumes of interest (VOI) were defined for the quantitative analysis of bone distribution. The central VOI corresponds to an interior cylindrical volume that captures the defect. The total VOI contains the entire volume of mineralization, in and around the defect, including the irregular bone formation outside the defect. At both 4 and 12 weeks, the alginate delivery groups (Groups II and III) had significantly more bone formation than the collagen delivery groups (Group I) (Figure Figure 6.3 A). The bone volume in the central VOI at 4 weeks was not significantly higher in Group II compared to Group I; however the p value was very close to significance ($p=0.051$). Although there was no difference between Groups II and III at 4 weeks, the central VOI analysis at 12 weeks revealed a significant increase in bone formation within the defect region associated with use of the nanofiber mesh tube (Group III). However, it was observed that the total bone volume at 12 weeks was not significantly different between Groups II and III. The change in bone volume between 4 and 12 weeks was calculated for each specimen (Figure Figure 6.3 B). This analysis demonstrated that Group III specimens had the largest increase in mineral accumulation between the two time points.

Mean density and connectivity density of the newly formed bone were evaluated at 4 and 12 weeks (Figure Figure 6.4). The results indicate that the mean bone density in

Group III specimens was significantly lower than those in Groups I and II, at both time points and in both VOIs. There was more than a 50% increase in the density of all groups between 4 and 12 weeks, indicating maturation of the mineralized tissue. At 4 weeks, the connectivity density in Group III was significantly higher than the other two groups, though there were no differences at 12 weeks. Finally, it was observed that the newly formed bone in the central VOI displayed higher connectivity density than that contained in the total VOI.

Biomechanical properties

Biomechanical properties of the regenerated femurs were obtained from torsional testing at 12 weeks. The maximum torque was 58% higher for Group III (alginate + mesh) specimens, compared to Group I (collagen) specimens (Figure Figure 6.5). In addition, the torsional stiffness and work to failure of Group III specimens were significantly higher than those in Group I by 58% and 102%, respectively. Though the value of mean failure angle was largest in the case of Group III, there were no significant differences between the groups. Importantly, there were no differences in the biomechanical properties between Groups I (collagen) and II (alginate). There were no significant differences in any of the mechanical parameters between Groups II and III; however the mean values of all parameters were higher for Group III specimens.

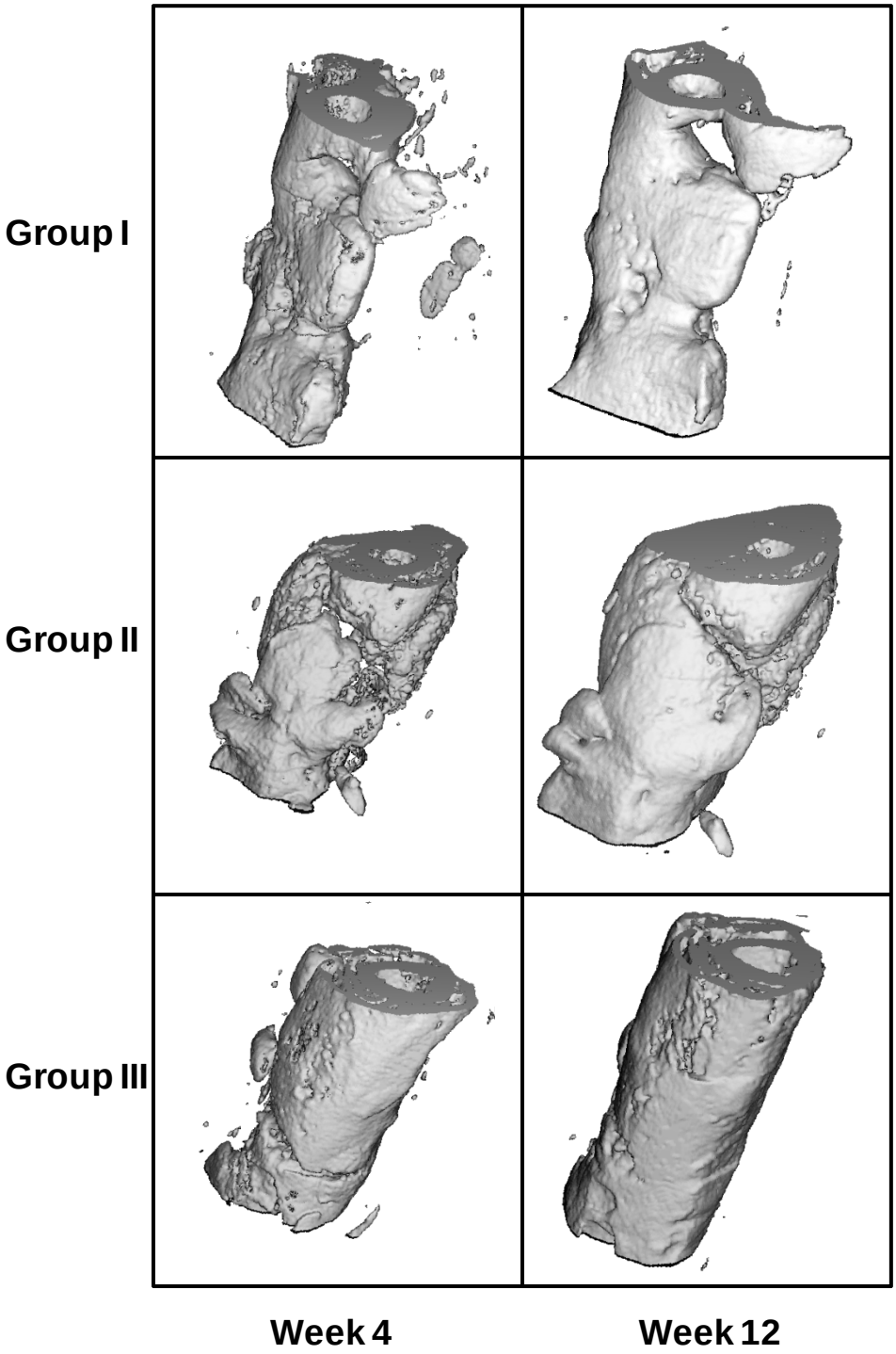

Figure 6.2. Three-dimensional *in vivo* μCT images at 4 and 12 weeks. There was evidence of ample bone formation in Group I samples by 4 weeks. Substantial bone formation in Group II specimens occurred outside the defect. Group III specimens, with a nanofiber mesh tube, demonstrated continuous cylindrical bone distribution within the defect. (I) Collagen scaffold + rhBMP-2, (II) Alginate scaffold + rhBMP-2, (III) Perforated nanofiber mesh tube + Alginate + rhBMP-2.

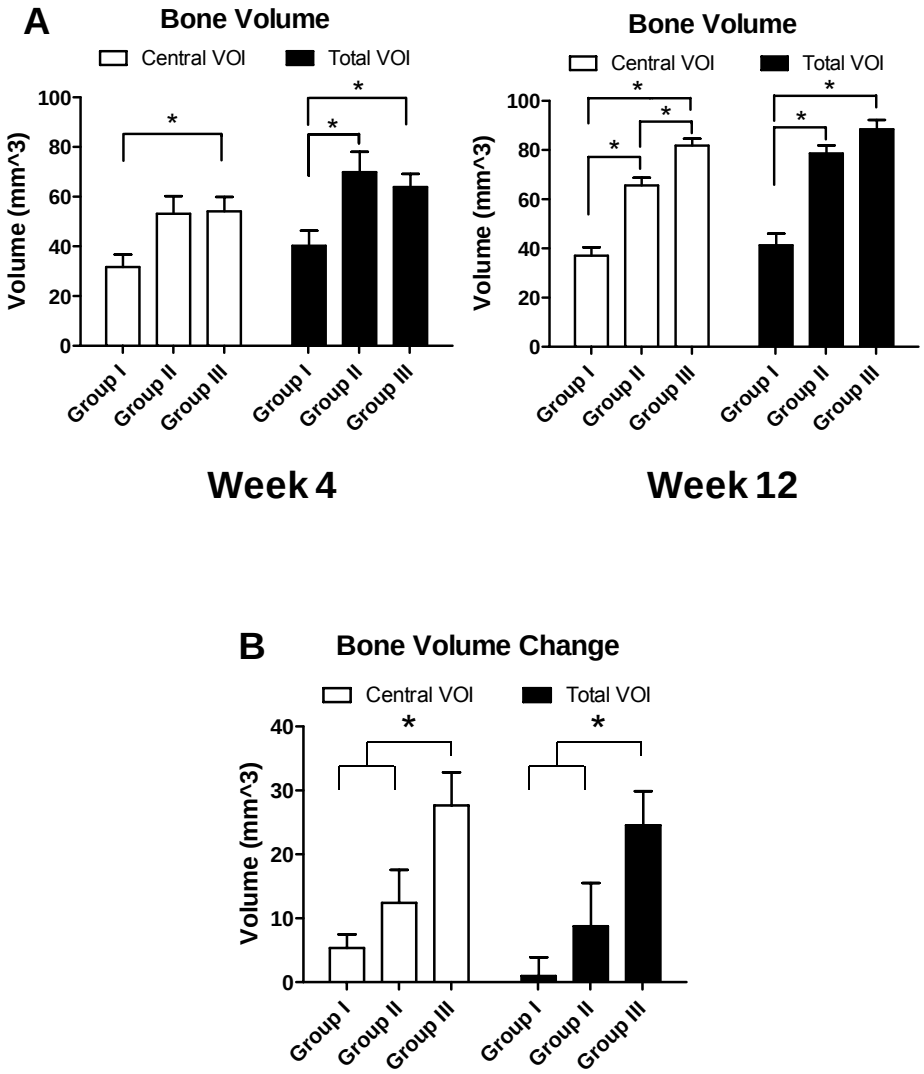

Figure 6.3. Quantitative μCT analysis of new bone volume. Groups II and III had significantly higher bone formation than Group I at both time points. In addition at 12 weeks, Group III possessed more bone in the central VOI region than Group II, consistent with the three-dimensional images. Group III also saw the largest increase in the bone volume between 4 and 12 weeks. * indicates significantly different ($p<0.05$). (I) Collagen scaffold + rhBMP-2, (II) Alginate scaffold + rhBMP-2, (III) Perforated nanofiber mesh tube + Alginate + rhBMP-2.

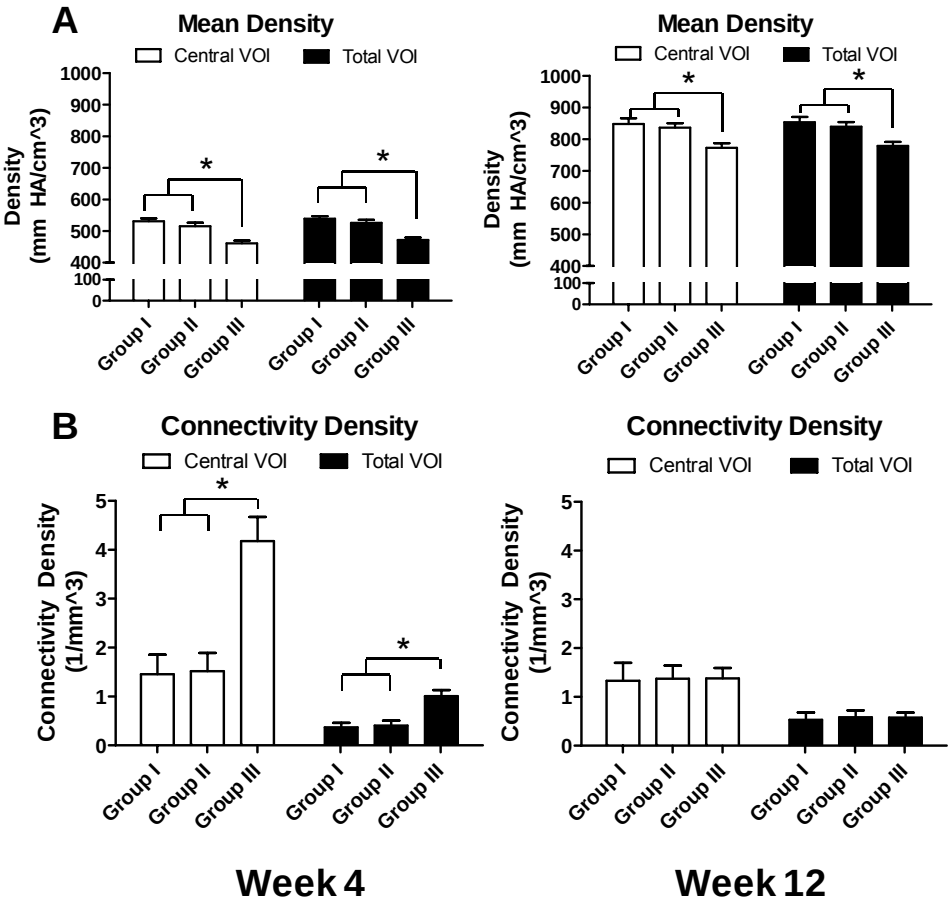

Figure 6.4. Mean density and connectivity density of the newly formed bone, obtained from μCT analysis. Mean density was significantly lower in Group III, compared to the other two groups at both time points, and in both VOIs. At week 4, connectivity density was the highest in Group III specimens. * indicates significantly different ($p<0.05$). (I) Collagen scaffold + rhBMP-2, (II) Alginate scaffold + rhBMP-2, (III) Perforated nanofiber mesh tube + Alginate + rhBMP-2.

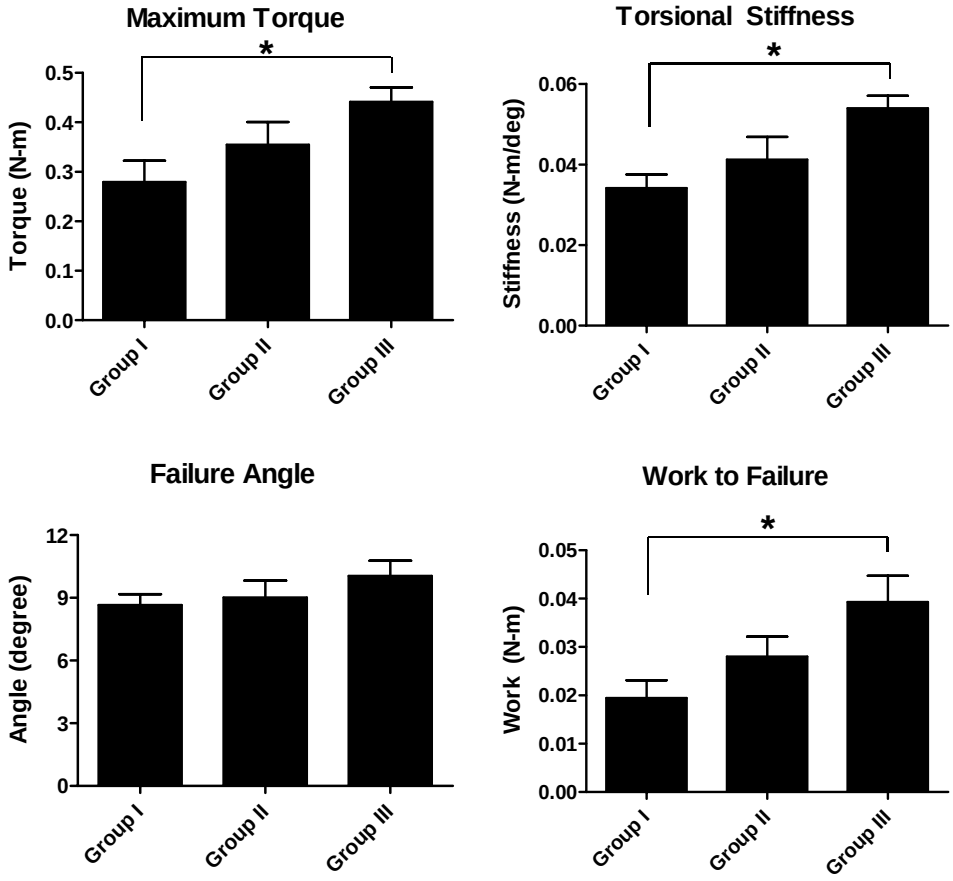

Figure 6.5. Biomechanical properties of regenerated femurs at 12 weeks. Group III specimens demonstrated higher maximum torque, torsional stiffness and work to failure than those in Group I. * indicates significantly different ($p<0.05$). (I) Collagen scaffold + rhBMP-2, (II) Alginate scaffold + rhBMP-2, (III) Perforated nanofiber mesh tube + Alginate + rhBMP-2.

Discussion

This study quantitatively compares a novel hybrid BMP delivery system to the current clinical standard for challenging bone defect repair. Compared to delivery on a collagen matrix, rhBMP-2 delivered at the same dose via alginate hydrogel resulted in enhanced bone formation as early as four weeks. The addition of a perforated nanofiber mesh to spatially retain the BMP hydrogel resulted in an increased mineral accumulation between 4 and 12 weeks, leading to enhanced bone ingrowth into the defect region at 12 weeks, compared to all other groups. Finally, biomechanical function was significantly improved following treatment with the hybrid nanofiber mesh/hydrogel delivery system, compared to collagen matrix delivery.

The amount and distribution of newly formed bone was influenced by the BMP delivery method. At two weeks, there appeared to a greater amount of mineral deposition with the collagen matrix delivery (Group I), compared to the alginate delivery (Groups II and III). However, by 4 weeks, the alginate groups demonstrated higher bone volume than the collagen matrix delivery, and this trend continued at 12 weeks. These results indicate that the kinetics of bone repair is dependent on the delivery system. This suggests that, whereas a majority of rhBMP-2 was released from the collagen matrix by 2 weeks, protein retention at the defect site beyond 2 weeks was improved with alginate hydrogel delivery. This is consistent with other studies that report that less than 5% of rhBMP-2 is retained within a collagen sponge by 2 weeks *in vivo* [159, 160]. Addition of the nanofiber mesh tube to the alginate hydrogel did not enhance overall bone formation that was seen in the total VOI. However, the pattern of bone formation that was observed in the alginate group without the mesh tube (Group II) indicated substantial bone formation outside the defect region, which implies leakage of the hydrogel and/or protein to the surrounding area. Analysis of the central VOI, which excluded this abnormal bone formation, revealed that presence of the nanofiber mesh tube (Group III) indeed enhanced bone formation within the defect region. This indicates that the nanofiber mesh tube is

able to improve the spatial retention of rhBMP-2 within the defect by containing the alginate and/or the growth factor.

Differences due to the BMP delivery method were observed in mineral deposition rate, as well as mineral density and biomechanical properties of the regenerated bone. Mineral accumulation between 4 and 12 weeks was highest for specimens in the hybrid delivery group (Group III), even higher than the alginate group without the mesh tube (Group II). This suggests that presence of the nanofiber mesh tube improves localization of rhBMP-2 within the defect site for a longer time period. It is possible that the nanofiber mesh tube slows the protein diffusion away from the implant, by perhaps binding the protein through nonspecific interactions. In an *in vitro* study, we observed that overnight incubation of a nanofiber mesh sample with a model protein, ovalbumin, resulted in 90% of the protein bound to the mesh, which remained attached to the mesh even at 1 week (data not shown). As the surface area of the nanofiber mesh is relatively large, these interaction effects may have a substantial effect on protein retention. Alternatively, the nanofiber mesh tube may function by constraining and therefore compacting the BMP-containing hydrogel, which could improve the local retention at later time points. In contrast to mineral accumulation, the density of the mineralized tissue was lowest in Group III. This suggests that new, immature bone is still being laid down in Group III specimens at later time points, which lowers the overall bone density in this group. It should be noted that the density obtained from the μCT is the actual density of the bone tissue, and not the apparent density of the entire bone. This would explain the lower tissue density in Group III specimens, even though the regenerated bone in these specimens appeared denser in the radiographs. In spite of the lower tissue density, maximum torque, torsional stiffness and work to failure were significantly higher in Group III specimens, when compared to those in Group I. This indicates that the higher bone volume in Group III compensated for the lower mineral density in contributing to the biomechanical properties. It should be noted that the Group III

torsional properties exceeded those of age-matched intact femurs determined previously (Chapter 5). For example, the mean maximum torque of Group III samples was observed to be 0.44 Nm, whereas it was 0.31 Nm in the case of intact femurs. There were no significant differences in the biomechanical properties between Groups II and III; however the mean values were consistently higher for Group III specimens. This suggests that, although there was significantly higher mineralization in Group III inside the defect region, the bony tissue outside the defect in Group II contributed somewhat to the overall mechanical properties.

The connectivity of the regenerating bone was also affected by the protein delivery system. Connectivity density is a parameter used to analyze trabecular bone, and is a measure of the number of trabeculae in a unit volume [299]. Though regenerating bone does not consist of mature trabeculae, the direct mineralization induced by BMPs is initiated at discrete locations, which then develop connections as the mineralization progresses [13]. The connectivity obtained from the μCT analysis of regenerating bone is a measure of these connections. At 4 weeks, Group III specimens demonstrated the highest connectivity density, compared to the other two groups, indicating a more interconnected bone structure, perhaps because of the spatial guidance provided by the alginate hydrogel and the containment effect of the nanofiber mesh tube. Containment due to the mesh tube may have facilitated connection of the mineralized nodes formed during intramembranous ossification. There were no differences in connectivity density at 12 weeks, and the values were uniformly low. This could be due to the fact that as the defect fills with bony tissue, the discrete bone initiation centers merge to form a continuous volume, which would reduce the connectivity density.

The results of this study demonstrate that delivery of rhBMP-2 via the hybrid nanofiber mesh/alginate system results in improved bone repair compared to delivery on a collagen matrix, the technique currently used by orthopaedic surgeons. This improvement may be due to the sustained delivery and spatial control achieved by the

hybrid system. It should, however, be noted that the processing of the collagen matrix used in this study is different than that of the absorbable collagen sponge (ACS) used in the clinic, and may affect the BMP delivery. Delivery of BMPs on collagen matrix has been shown to result in significant initial burst release, in the range of 40-90% [160]. Winn et al. reported that collagen sponges loaded with rhBMP-2 exhibited a continuous release for 2 weeks with a half life of 3-5 days in a rat ectopic model; however the long term release was not investigated [159]. They hypothesized that rhBMP-2 release from the collagen sponge is mediated by desorption of the protein from the collagen, degradation of the sponge and solubility of the protein. The binding of rhBMP-2 to collagen sponges has been found to be extremely sensitive to pH, suggesting that the interaction between collagen and rhBMP-2 is due to electrostatic forces [153]. As desorption and collagen degradation is expected to occur rapidly and unpredictably *in vivo*, this suggests that the growth factor may not be available at later time points, when delivered by this technique. The ability of alginate hydrogel to maintain sustained delivery of protein has been reported in a number of studies [74, 105, 172, 286]. In a previous *in vitro* release study, we observed that approximately 10% of the encapsulated rhBMP-2 remains attached to alginate after 3 weeks, though the amount released in the media was negligible at this time point (Chapter 5). This suggests that the protein binds to the alginate matrix and may be available to invading progenitor cells at later time points, which would mean that the function of the alginate hydrogel is more to improve long term availability than sustained release. Binding of the protein by alginate may be advantageous by protecting it from degradation [285, 286]. Our results also suggest that the nanofiber mesh tube may aid in containing the exogenous growth factor within the defect region. A couple of recent studies have highlighted the advantage of utilizing a 'container' in retaining biologic factors at the defect site [94, 300]. For instance, Giardino et al. demonstrated that when a 400 μm thick poly-DL-lactide tube was utilized to

constrain dimineralized bone matrix and bone marrow stromal cells within segmental defects, it led to a significant increase in the thickness of newly-formed bone [94].

There are a number of drawbacks associated with the use of natural collagen for the delivery of rhBMP-2. The collagen matrix is typically obtained from an animal source and further crosslinked with formaldehyde to improve its mechanical properties. The risk of an immunogenic reaction to collagen or pathogen transmission to the host cannot be eliminated [161, 162]. Concerns also persist regarding the heterogeneity of the product, as it is derived from animals. In addition, the collagen processing steps such as crosslinking and sterilization have a large impact on the interaction of BMPs with the collagen matrix, and therefore on the release profile [83, 301]. Crosslinking reduces BMP binding; however uncrosslinked collagen degrades faster and leads to a rapid loss of the growth factor [301]. These contradictory requirements create challenges in developing an optimal delivery system. Finally, loss of the BMP solution when the collagen sponge is handled during surgery has to be considered.

The delivery of BMPs on collagen matrix has been tested in a number of animal models of large bone defect repair; however high protein doses are typically required [302-306]. For instance, Cuomo et al. reported that delivery of 10 μg rhBMP-2 (double the dose used in this study) resulted in bony bridging of a 6 mm rat segmental defect [305], which is less challenging than the 8 mm defect we utilized. The injection of 5 μg rhBMP-2 in this study is equivalent to a 20 μg/kg dose, which is around $1/5^{th}$ the clinical dose used in humans. It should be noted that sensitivity to rhBMP-2 varies with species; however our dose is still low compared to that used in similar models [74, 91, 294, 295]. By maintaining sustained and localized availability of rhBMP-2, the hybrid alginate/nanofiber mesh system could result in functional bone restoration at a lower dose, thereby reducing the cost and complications associated with collagen matrix delivery [60, 61]. In conclusion, this study provides promising evidence in a challenging

small animal model that spatiotemporal delivery strategies may enhance the therapeutic efficacy of BMP for repair of large bone defects.

CHAPTER 7

SUMMARY AND FUTURE DIRECTIONS

Overall Summary

Tissue engineering/regenerative (TE/RM) strategies have demonstrated great potential for the repair of bone defects. Such approaches typically involve the delivery of biological agents on a carrier scaffold. The function of the scaffold is to provide a template for cell guidance and tissue deposition, while biological cues induce a strong healing response. Biological agents such as stem and progenitor cells directly participate in the tissue regeneration process, and in addition may secrete factors that attract endogenous cells. Another set of TE/RM strategies rely solely on the recruitment of endogenous cells by the implant. These acellular strategies utilize soluble growth factors or biomimetic surfaces to attract and provide specific signals to local cells. The optimum combination of scaffolds and biologics may vary with different bone defects and patient populations.

The goal of this thesis was to investigate the potential of electrospun nanofiber mesh scaffolds for bone regeneration. Nanofiber meshes were utilized in a three-pronged approach. First, we validated their ability to robustly support osteogenic cell functions, including proliferation and matrix mineralization. We also demonstrated their efficacy as a cell delivery vehicle (Aim I; Chapter 3). Second, we investigated the effects of modulating nanofiber bioactivity and orientation on stem cell programming (Aim II; Chapter 4). Our results indicate that functionalization of nanofiber meshes with the collagen-mimetic GFOGER peptide enhanced the migration, proliferation and osteogenic differentiation of cells. Fiber alignment improved cell migration along the direction of fiber orientation. Finally, a nanofiber mesh based hybrid system for growth factor delivery was developed for bone repair and tested in a challenging animal model (Aim III; Chapters 5 and 6). The delivery of rhBMP-2 via this system resulted in the functional

restoration of limb function, and in fact proved more efficacious than the current clinical standard for rhBMP-2 delivery.

Aim I: Nanofiber Meshes for Cell Culture and Delivery

The electrospinning techniques developed in Aim I of this thesis were utilized for the fabrication of nanofiber meshes in subsequent studies. In this Aim, we also validated the ability of nanofiber meshes to support vital osteogenic functions of two stem cell types. Finally, in an *in vitro* study, we demonstrated that a cell-seeded nanofiber mesh wrapped around a three-dimensional scaffold can effectively colonize the scaffold.

Nanofiber mesh as a model cell culture surface

Our results provide support to the utilization of electrospun nanofiber meshes as a model cell culture surface *in vitro*. Tissue culture plastic is ubiquitously used for studying cell behavior *in vitro*. However, this culture surface is flat and inert, and does not resemble the *in vivo* ECM milieu that the cell interacts with. In fact, in our studies, cells frequently lifted off the tissue culture plastic implying a poor adherence to the surface. Cell culture substrates that are structurally closer to the *in vivo* environment would better allow cells to display their native behavior. For example, Matrigel, which is a basement membrane ECM secreted by mouse tumor cells, has found acceptance with researchers studying the differentiation and invasive activity of tumor cells [307]. Nanofiber meshes have fibers in the nanometer range, and scale-wise resemble collagen fibrils in native tissue [97]. They can also be manufactured from natural materials like collagen and fibrinogen to further imitate the ECM. In our studies, we observed that cells demonstrated improved adherence and mineralization on nanofiber meshes. Other studies have also demonstrated the advantages of using nanofibrous over flat surfaces in supporting cellular differentiation [236, 237]. Future studies could further characterize the osteogenic differentiation process on the nanofiber meshes versus tissue culture

plastic. This may involve, for example, analyzing differences in adhesion strength [262] and osteogenic gene expression [237] due to the culture surfaces.

Nanofiber Mesh as a Cell Delivery Vehicle

The efficient delivery of exogenous cells to sites of injury is one of the main stumbling blocks in the commercialization of cell-based therapies. We have engineered a periosteum-like tissue by seeding a high density of cells on a nanofiber mesh. This tissue engineered periosteum has a cellular and a fibrous layer, much like native periosteum. When this construct was wrapped around a collagen scaffold *in vitro*, with cells facing the inside, some cells migrated on to the scaffold and populated it. Compared to the direct seeding method, we observed improved viability of cells on the scaffold when they were delivered on the nanofiber mesh construct. This may be due to the limited nutrient transport to the center of the three-dimensional scaffold, which would result in cell death.

The efficacy of the engineered periosteum to deliver cells *in vivo* needs to be investigated in further studies. One limitation of this method is that fewer numbers of cells can be accommodated on the nanofiber mesh surface, compared to seeding directly on three-dimensional scaffolds. For example, on a 15×10 mm mesh sample, a very high seeding density of 200,000 cells/cm^2 still results in only 300,000 cells on the mesh. In contrast a Ø4×9 mm scaffold can easily hold 2-4 million cells. However, if a majority of the implanted cells inside the scaffold are not able to survive due to the initial lack of vascularity [137, 140], the number of cells surviving may turn out to be greater with the nanofiber mesh delivery.

Aim II: Modulation of Nanofiber Mesh Design

Though the synthetic random meshes from Aim I supported the osteogenic activities of cells, we investigated whether they could be further improved by adding two design elements: a biomimetic surface and an oriented topography. First, nanofiber

meshes were coated with the collagen-mimetic adhesive peptide, GFOGER. The motivation behind this is the fact that the interaction of cells with the GFOGER motif via integrin receptors is a critical event in the osteogenic differentiation pathway. We also electrospun meshes with fibers aligned along a preferred direction with the expectation that the aligned fibers would provide contact guidance thereby improving cell migration. Our results are in line with our original conjecture, and demonstrate that GFOGER coating enhanced the migration, proliferation and osteogenic differentiation of cells, whereas fiber alignment improved cell migration.

Mechanism of GFOGER action

The positive effects of GFOGER on cell function likely occur via the $\alpha_2\beta_1$ integrin. Future studies could delineate the molecular mechanism of how GFOGER potentiates the migration and osteogenic differentiation of cells on nanofiber meshes. For example, by using an antibody against the α_2 integrin, Reyes et al. demonstrated that the adhesion of osteoblast-like cells on GFOGER coated titanium surfaces was specific to the $\alpha_2\beta_1$ integrin [121]. It would also be interesting to study the intracellular events that occur after the GFOGER-integrin engagement.

Effect of fiber diameter, surface area and porosity

One confounding factor in studying the effects of GFOGER coating and fiber alignment was the difference in fiber diameters between random and aligned nanofiber meshes. We attempted to maintain similar diameters by changing various electrospinning parameters, but were unsuccessful. In addition to the differences in diameters, other parameters such as surface area and porosity may also have been affected by the fiber alignment. For example, differences in surface area would change the overall surface density of the adsorbed GFOGER and collagen, which could have a considerable effect on cell function. Unfortunately, it was not possible to calculate these parameters in

nanofiber meshes due to the lack of specialized equipment needed to make these measurements. Future experiments could further scrutinize the effects of fiber diameter, surface area and porosity on cell behavior.

GFOGER immobilization on nanofiber surfaces

An improvement over the passive adsorption of GFOGER may be the immobilization of the peptide on the nanofiber surfaces through the primary amine terminal [251]. This would result in the peptide being orientated in a specific direction, making the cell recognition site highly accessible, and thereby improve peptide activity. In contrast, in the passive adsorption method that was utilized in this study, the peptide can adopt a range of orientations, some of which could mask the cell recognition site. The immobilization scheme would, in addition, prevent desorption of the peptide from the surface, which could result in longer term signaling.

Promoting *in vivo* bone regeneration with nanofiber mesh tubes

Despite the substantial improvement in cell migration and differentiation *in vitro*, GFOGER coating did not enhance bone regeneration *in vivo*. GFOGER coated nanofiber mesh tubes did not result in the bridging of segmental bone defects. The likely explanation is that the nanofiber mesh tube alone is not able to provide the structure for bony bridging in this challenging 8 mm defect. With the inside of the defect kept empty, the cells from the periosteum and bone ends are perhaps not able to migrate to the defect center. As the hematoma is limited to the bone ends, there is a large void at the defect center that cannot support cell colonization. It is still surprising that improved mineral deposition was not seen even on the surface of the GFOGER coated tubes.

It is possible that smaller defects (5-6 mm) may see a benefit simply due to a nanofiber mesh tube. Guided bone regeneration of diaphyseal defects solely by the placement of membranes on the periosteal surface has been reported in literature, though

the defects have been relatively small [180, 182, 284]. A future strategy could involve the tethering of a growth factor like rhBMP-2 on the nanofiber mesh surface. The presence of this potent osteoinductive protein may generate a strong healing response despite the empty center. The binding of rhBMP-2 to the nanofiber surfaces could be achieved by using di-NH_2-PEG and heparin as linkers [265].

The addition of a RGD conjugated alginate hydrogel inside the nanofiber mesh tube also did not result in defect bridging (Chapter 5). This implies that a strong osteogenic stimulus is required throughout the defect in this model. One approach future studies could take is the covalent conjugation of the GFOGER peptide with alginate, which would be injected inside a GFOGER coated tube. This would ensure the presence of the osteoinductive peptide at the defect interior and periphery. Another method for improving bone formation could be the placement of a GFOGER coated structural scaffold inside the nanofiber mesh tube.

Aim III: Nanofiber Mesh/Alginate Growth Factor Delivery System

From the *in vivo* studies in Aim II, it was clear that in order to repair a large diaphyseal bone defect, a scaffolding material containing a strong biologic stimulus would need to be present inside the nanofiber mesh tube. Therefore, a novel hybrid growth factor delivery system was developed in this study. This system consists of placing a nanofiber mesh tube around the bone defects, and injecting alginate hydrogel that contains rhBMP-2 inside the tube. The utilization of this system resulted in bony bridging of challenging segmental defects *in vivo*. However, a number of parameters need to be examined to optimize the repair process.

The role of perforations in defect healing

A perforated mesh tube design resulted in the acceleration of bone formation over a non-perforated mesh tube. We originally hypothesized that this acceleration is due to

the improved vascular invasion of the defect site through the perforations. However, μCT analysis of the vascular ingrowth at the defect site at 3 weeks by using a radiopaque contrast agent did not support this hypothesis. In fact, very little vascularity was detected inside the defect volume at this time point. This is surprising as significant bone formation is observed by 4 weeks. In tissue development, the deposition of bony tissue is preceded by cell migration and condensation. It is possible that the cell migration in our system occurred, not via the vasculature, but due to the chemotactic attraction of rhBMP-2. If true, this would also support the hypothesis that the perforations in the mesh enhanced the migration of progenitor cells from the surrounding soft tissues. Given that perforations in the mesh tube improved bone regeneration, it would be interesting to fabricate nanofiber meshes from a polymer which degrades faster than PCL, such as Poly(lactic-co-glycolic acid) (PLGA). The faster degradation of PLGA mesh tubes may enhance vascular ingrowth and/or progenitor cell migration into the defect.

It would be interesting to analyze the vascular ingrowth at a later time point, following substantial bone formation. This may also prevent the problem of contrast agent leakage that was observed in some samples, which occurred perhaps due to the immature vessels at the early time point. A resolution of 21.5 μm was utilized for the vascular analysis in order to maintain a balance between image resolution and computational power. It is possible that a higher resolution of 10 μm would permit better detection of the microvasculature. However it has been reported previously that the higher resolution did not significantly alter the vascular volume, though it affected other parameters like connectivity and vessel thickness [107].

Mechanical stimuli and tissue remodeling

The delivery of rhBMP-2 in the nanofiber mesh/alginate system resulted in the robust bridging of segmental bone defects by 12 weeks. In fact, almost the entire defect space was occupied by bony tissue, though there was some marrow development. Though

the mechanical properties exceeded those of intact femurs, the cortical structure of the femur diaphysis was not restored. This was not surprising considering that the 12 week time point is still short for significant remodeling events to occur. In addition, the continued presence of the stable fixation plate does not permit the mechanical loading of the bone, an important for remodeling. Other studies in our laboratory are being performed to provide mechanical stimuli in this model by utilizing compliant fixation plates [308]. To investigate the remodeling at late time points, we extended our observation period on a few animals (n = 3) up to 22 weeks. The radiographic images over the entire course of the study revealed that the majority of the new bone was deposited by 8 weeks, and no gross remodeling or resorption took place up to 22 weeks (Figure 7.1). To investigate whether the restored limb may be able to bear physiologic loads, we removed the polysulfone plate that stabilizes the defect at 22 weeks. We observed that not only did the limb not collapse after plate removal, but the animal started putting full weight on that limb and resumed normal ambulation a few weeks later. This indicates that in addition to regaining the original mechanical properties, the limb is fully functional again. This is a remarkable achievement and a first, in our laboratory at least. Surprisingly, even 4 weeks after the plate removal, there did not appear to be major signs of remodeling of the regenerated bone at the whole bone level, despite the existence of direct mechanical stimuli. Future studies could investigate this further using μCT to analyze any microstructural changes and at later time points after plate removal.

Growth factor dosage

In all our *in vivo* studies with the nanofiber mesh/alginate system, a 5 μg dose of rhBMP-2 was selected to demonstrate the feasibility of this system. This dose is in the lower range of what has been reported in literature (2-20 μg). In addition, most rat femoral defects are 5-6 mm, less than the 8 mm defects used in this study. Previous studies in our lab have delivered 2 μg rhBMP-2 in alginate hydrogel, though they utilized

a slow degrading three-dimensional scaffold [107]. In addition to the partial bridging observed with this dose, comparisons of the torsional testing results with respect to the nanofiber mesh/alginate system indicate much lower mechanical properties. In view of the robust bridging observed in our studies, an important question is: what is the lowest dose of rhBMP-2 that can be delivered in the hybrid system while still obtaining consistent defect bridging? We have conducted a preliminary study (n = 1) in which a dose of 1 μg rhBMP-2 was delivered via the hybrid system. The results indicate that 1 μg rhBMP-2 was sufficient in robust bridging the defect (Figure 7.2). However, compared to the 5 μg dose, bone volume appeared to be lower. As the torsional properties of regenerated femurs with the 5 μg dose exceeded those of native femurs by approximately 33%, the reduced bone volume at the 1 μg dose may still lead to properties equivalent to native femurs. Future studies could investigate this dose dependency, and establish the minimum rhBMP-2 dose required to be delivered through the hybrid system. If these studies can obtain consistent bridging with even 1 μg rhBMP-2, it will be the lowest dose reported in the literature for healing femoral diaphyseal defects [74, 91, 294, 295]. A lower dose of BMP than the 3.5-12 mg currently used in humans would decrease the cost of the procedure and reduce the side effects, thereby improving physician and reimbursement acceptance.

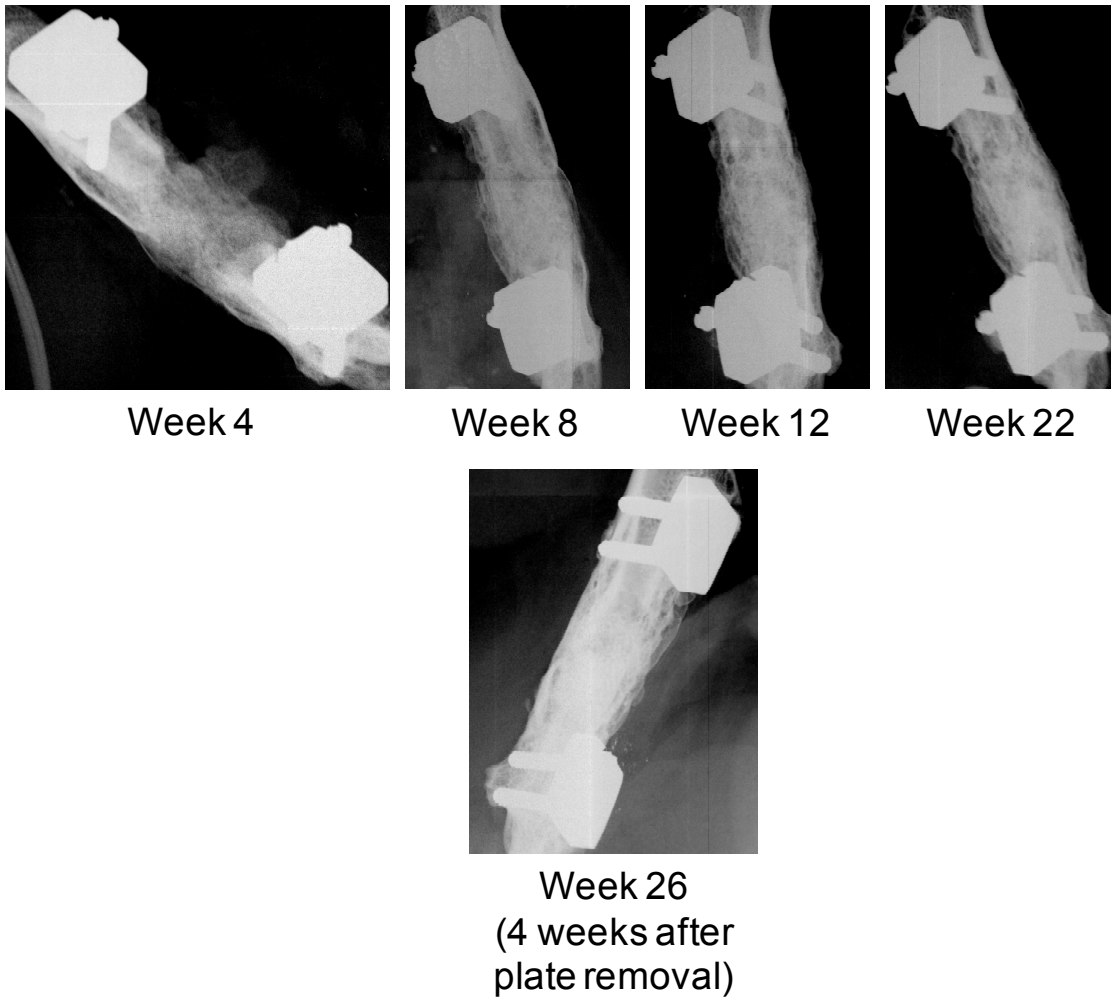

Figure 7.1. Long-term observation of a regenerated femur. In a preliminary study, one specimen was observed beyond the usual 12 weeks of observation. At 22 weeks, the polysulfone plate was removed to enable loading of the regenerated femur. The specimen was observed for a further 4 weeks, up to a total of 26 weeks from the original surgery. No significant change in bone volume or distribution is seen beyond 8 weeks, even after loading. The loaded femur did not collapse and remained intact.

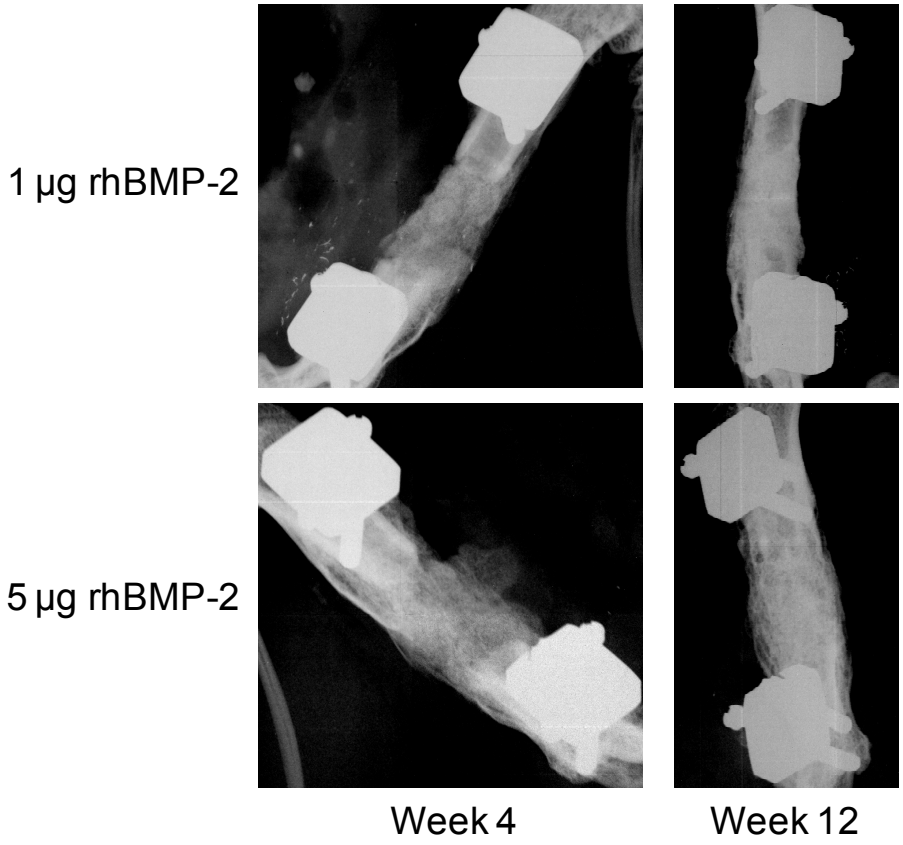

Figure 7.2. Dependence of rhBMP-2 dose on segmental bone defect repair. In a preliminary study, we investigated whether a lower dose of rhBMP-2 would lead to defect bridging. A dose of 1 µg rhBMP-2 was sufficient in to heal the defect, though the bone volume appeared to be lower than in the case of the 5 µg rhBMP-2 dose.

Growth factor delivery considerations

The performance of the alginate hydrogel in delivering rhBMP-2 in our studies warrants further discussion. In the *in vitro* release study, of the 500 ng rhBMP-2 that was added to the alginate, only 276 ng was recovered immediately after gelation, indicating that the functional encapsulation percentage was 55%. It is possible that the binding of some rhBMP-2 molecules to the alginate matrix prevents the detection of the protein by the antibody, even after dissolving the hydrogel. In this case, the actual encapsulation percentage will be higher than what the ELISA results suggest. An alternative explanation for the low encapsulation percentage in our studies could be the denaturation of the rhBMP-2 due to the high shear forces applied during the crosslinking step.

The binding of rhBMP-2 to alginate could also be part of the reason why only 26% of the *encapsulated* protein is released to the buffer. A recent study estimated the total *in vitro* release of another protein, VEGF, from a similar alginate hydrogel to be 40% of the *total* amount over 21 days [286]. It should however be noted that a radiolabeled VEGF was utilized in this study for protein detection, instead of an ELISA. This also brings into question the ability of the antibody based ELISA to detect alginate-bound protein after its release into the buffer. The other potential reason for the low release percentage is that the remaining protein is denatured or degraded by the time it is released, and therefore not detected. Interestingly, we noted that 10% of the protein was found to be still present inside the hydrogel at 21 days. As the half life of rhBMP-2 in its free form is relatively short, this suggests that a substantial amount of the protein binds to the alginate matrix and is protected from degradation. This could explain why we obtain robust bone formation with the alginate/nanofiber mesh rhBMP-2 delivery at later time points, even though the encapsulation percentage was low and majority of the release occurred within the first week. It should be kept in mind though, that the release study was done *in vitro*, and may not correspond to the *in vivo* release due to differences in

numerous conditions. Future studies could investigate the *in vivo* retention of the protein at the defect site by using a radioactive label on the protein [159, 160].

Due to the relatively low functional protein encapsulation percentage and the non-optimal release kinetics of alginate, it may be replaced by another hydrogel in the hybrid system. Another drawback of alginate is inability to support cell-mediated remodeling and breakdown, even with RGD functionalization. Histological images revealed the continued presence of alginate in the defect at 12 weeks, even though the low molecular weight formulation we utilized degrades faster. This could be explained by the fact that *in vivo* degradation is highly dependent of the local environment, and the isolated alginate islands within the dense bone matrix remain trapped there. In fact, the gross observation of the newly formed bone reveals a granular consistency of the mineral, perhaps due to the presence of the residual alginate islands. Hydrogels constructed from biomaterials that have better cell compatibility and degrade faster, such as collagen and gelatin, may be used to replace alginate. For example, Tabata and coworkers have developed gelatin hydrogels for growth factor release, which have demonstrated *in vivo* degradation and release profiles suitable for tissue regeneration [67]. Another advantage of gelatin is its long history of clinical use.

Delayed growth factor delivery

The timing of the growth factor delivery is another factor that future studies could investigate. It is well known that the first phase of the fracture healing process consists of an inflammatory response, which lasts for around one week. However, during this time, majority of the growth factor is released from the delivery system, despite the fact that the defect site is not yet ready for osteogenic activities. Therefore, a substantial portion of the exogenous growth factor is probably wasted, which would explain the supraphysiologic doses of BMPs needed to generate a strong repair response. The delayed delivery of BMPs to bone defects, after the subsidence of the inflammatory

process, could improve the healing efficiency by presenting the growth factor only when the injury site is ready to respond to it. The hybrid nanofiber mesh/hydrogel system is conducive to delayed delivery because the nanofiber mesh tube maintains space and prevents invagination of soft tissue in the defect, for at least 2 weeks. The growth factor-hydrogel can be injected inside this space at the later time point using minimally invasive procedures. This delayed delivery system could result in a further reduction in the rhBMP-2 dose required for successful bone repair. This hypothesis is supported by the recent data reported by Betz et al., which demonstrate an improvement in segmental bone defect repair, when the percutaneous injection of adenoviral BMP-2 vector was delayed until 5 or 10 days after defect creation [309].

Conclusions

Though TE/RM approaches have demonstrated significant promise for bone regeneration, very little has been translated to clinical practice. The studies performed in this thesis have suggested novel techniques for improving the repair of clinically challenging bone defects. The central theme of our work consists of delivering bioactive molecules on electrospun nanofiber meshes. We have validated our approach in a challenging small animal model, and demonstrated that a hybrid nanofiber mesh/alginate delivery system performs better than the current clinical system for BMP delivery. Our results indicate that the delivery of BMP via the hybrid system may reduce the dose and side effects of BMP, thereby broadening the use of BMP based bone augmentation procedures. The utilization of a small animal model permitted quantitative μCT analyses of bone regeneration that enabled us to identify the best configuration for protein delivery. The hybrid system has to be tested next in a large animal model before initiating clinical trials. If proven successful in these studies, our protein delivery system has the potential to become the standard of care for clinically challenging bone defects, including large bone defects, open tibial fractures, and nonunions.

APPENDIX A

NANOFIBER MESH PROTOCOLS

A.1 Electrospinning Nanofiber Meshes

Supplies

- 5 ml Syringe
- 22 Gauge needle tip
- Solution: 12 w/v % PCL in 90/10 hexafluoro-2-propanol/dimethylformamide (HFP/DMF). Using a stir bar, start with mixing HFP and DMF (add DMF gradually). Then add PCL. Keep overnight. Use within 1-2 days.

Procedure

1. To change infuse rate: press “set” then “infuse rate”
2. To change diameter: press “set” then “diameter”
3. Put the plate at a certain distance from the surface
4. Put the voltage source around the needle tip.
5. Push the setup such that the needle goes inside.
6. Put an aluminum foil paper so the mesh is deposited on it.
7. Put a towel paper before you start up so the first spray will go on it.
8. Click on run
9. Once you see the solution coming out of the needle tip, click voltage on.
10. Continue increasing the voltage until a drop forms at the needle tip and doesn’t drop. The drop should form a cone; if the drop is big, increase voltage.
11. Check on the mesh every 1-2 hours to ensure drop is still the right size. Increase voltage to reduce drop size, if needed.

Typical Electrospinning Parameters

- Needle gauge: 22
- Distance: 20-23 cm
- Flow rate: 0.75 ml/hr
- Voltage: 13-20 kV
- Electrospinning time: 5-6 hours (gives thick enough mesh for surgery)

A.2 Fabrication of Perforated Nanofiber Mesh Tubes

Supplies

- Thick mesh
- Petri dish (10 cm)
- Ethanol absolute (200 proof)
- Biopsy punch (dia = 1 mm)
- Steel mandrel (dia = 4.5 mm)
- UV glue (Dymax 1187-M-VT)
- Lamp for curing UV glue

Procedure

1. Cut rectangular pieces of mesh and punch holes as shown in figure below:

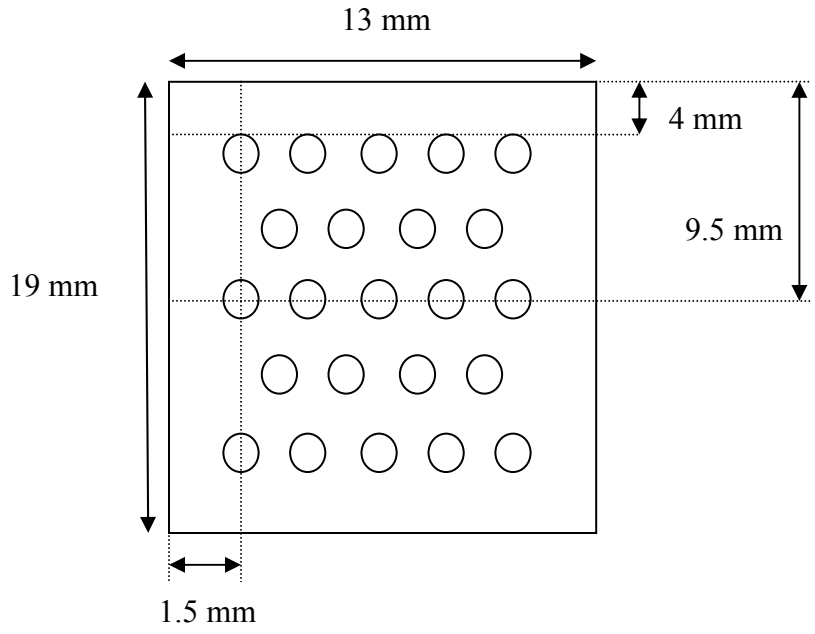

2. Wrap the above rectangular piece of mesh around the steel mandrel over the longer edge to form a cylinder having an inner diameter of 4.5 mm and 13 mm length. Close the overlapping edge with the UV glue. Use a 25g needle to draw a line of UV glue on the edge, and cure it with the lamp.
3. Wash the tubes in ethanol 2X and sterilize by ethanol evaporation overnight in petri dish.
4. Add sterile 70% ethanol to the petri dish to wet the tubes. Keep for 30 minutes.
5. Wash 3X with excess of PBS.
6. Aspirate PBS and add α-MEM the night before surgery.

A.3 Nanofiber Mesh Sample Preparation and Cell Culture

Fabricating nanofiber meshes and preparing samples for cell culture

1. Electrospin meshes of desired thickness, alignment, and fiber diameter. We typically make meshes from poly (ε-caprolactone) (PCL).
2. (Optional): Obtain SEM images of the meshes to confirm fiber diameter and alignment.
3. Nanofiber meshes can be stored long term in a desiccator to minimize exposure to moisture.
4. Cut the meshes to the desired size/shape using a ruler and scissors. The mesh can be placed face down, and the desired size/shape can be marked on the aluminum foil. Be careful not to put too much pressure on the mesh. Use another piece of foil on the bottom so that the mesh is resting on a smooth surface. If circular samples are required, a biopsy punch of appropriate diameter can be used. The biopsy punch allows for more accurate control of sample area, but thick meshes are somewhat difficult to punch out. We usually use either 1X1-cm rectangular samples or 12-mm diameter circular sample.
5. To separate the mesh from the aluminum foil, immerse the meshes in 70/30 (v/v) ethanol/water solution in a Petri dish. Reagent alcohol can be substituted for pure ethanol. Once wet with the solution, separate the mesh from the foil using fine tipped forceps. Touch the mesh only at the edges to minimize damage and indentation marks on the mesh. Thick meshes may have some air trapped inside – try to gently press and remove them.

Sterilizing meshes

1. Transfer the meshes from the Petri Dish to sterile plates using forceps in a laminar flow hood. We use 24-well low cell attachment plates, so that the only surface the cells can attach to is the mesh.
2. Submerge the meshes in 200 proof ethanol (in 24-well plates, 500 uL is enough).
3. Let the ethanol evaporate completely in the hood overnight. After this the mesh is considered sterile.

Cell seeding and culture

1. After ethanol evaporation, the mesh will be dry. Submerge the meshes in sterile 70/30 (v/v) ethanol/water solution for 2-3 minutes. This will help wet the mesh before adding media – PCL is quite hydrophobic initially.
2. Aspirate the ethanol/water solution. If the mesh samples tend to float in the well, place a sterile dead weight on the mesh edges to keep them on the bottom of the well. We use sterile stainless steel staples for this purpose.
3. Wash the meshes at least three times with excess PBS to remove any residual ethanol. Leave the meshes submerged in PBS until cells are ready to seed. At this point, the meshes can be coated with collagen, fibronectin or any other adhesive molecule to improve cell attachment.
4. Prepare culture media and cells.
5. Aspirate the PBS and replace with desired amount of culture media (we use a total of 1 mL per well in 24-well plates – therefore we add 800 µL of media in this step and seed cells in 200µL in the next step).
6. Seed cells at a density of 10,000-40,000 cells/cm^2. We usually seed at a density of 20,000 cells/cm^2 for differentiation studies. The area is based on the well bottom area and not the mesh area. Cells will sit on the well bottom

surface as well, but if low attachment plates are used, then they will be able to attach only to the mesh.

7. Incubate for 2-4 days before any media change. We usually seed the cells in growth media and change to osteogenic media after 3-4 days. This is considered day 0 for osteogenic differentiation.
8. Change media every 3-4 days or as required for the specific cells used.
9. Take down samples for various assays between 0-5 weeks. We usually do DNA and ALP assays from 0-5 weeks, and calcium assays from 3-5 weeks. For the calcium assay, it is good to have an appropriate acellular or non-mineralizing cell control to eliminate the possibility of non-cell mediated mineral deposition. FTIR can also be performed to evaluate physiologic nature of the deposited mineral.

A.4 Infiltration Assay

Fabricating and preparing meshes

1. Electrospin meshes of desired thickness, alignment, and fiber diameter
2. (Optional): Obtain SEM images of the meshes to confirm fiber diameter and alignment
3. Cut the meshes to the desired size/shape using a ruler and scissor.
4. To separate the mesh from the aluminum foil, immerse the meshes in 70/30 v/v ethanol/water solution in a container (i.e. in a petri dish). Once wet with the solution, separate the mesh from the foil using forceps (be careful not to damage or leave indentation marks on the mesh with the forceps)

Sterilizing meshes

1. Transfer the meshes from the container to sterile plates (we use 24-well plates, non-TC) using sterile forceps in a sterile hood.
2. Submerge the meshes in sterile 70/30 v/v ethanol/water solution (in 24-well plates, 500 uL is enough).
3. Ethanol-dry the meshes in the hood overnight.

Autoclaving

1. Autoclave the required number of sterile stainless steel strips (we use 0.9 mm wide strips) and "holding strips" (we use stainless steel staples); one holding staple and one strip per mesh. Also autoclave forceps.

Cell seeding and infiltration

1. Submerge the ethanol-dried meshes in sterile 70/30 v/v ethanol/water solution for 2-3 minutes.
2. Wash the meshes at least three times with excess PBS to remove any residual ethanol. Leave the meshes submerged in PBS until cells are ready to seed.
3. Prepare culture media.
4. Prepare cells.
5. Aspirate the PBS and replace with desired amount of culture media (we use 1 mL per well in 24-well plates).
6. Place the holding staples on the meshes and the strips in the center of the meshes.
7. Seed cells at 40,000 cells/cm^2.
8. Incubate for 24 hours.
9. Remove the strip to create the region of no cells.
10. Observe infiltration into the gap using DAPI staining.

APPENDIX B

CELL FUNCTION ANALYSIS PROTOCOLS

B.1 Extraction of DNA and ALP

Collection of mesh samples

1. Wash 3X with PBS on shaker plate.
2. Pick mesh up with forceps and place in eppendorf tube containing 0.5 ml of 0.05% Triton X-100/PBS.
3. Store samples at -80C (or -20C) if needed, or continue with the lysis.

Cell lysis

1. Add plenty of dry ice to the bottom of an ice bucket.
2. Add methanol to the bucket till it is 2-3 cm. above the dry ice, and allow the methanol to become cold for around 5 minutes. (Solution is cold enough when the contents of the tubes freeze within 3-5 minutes.)
3. Immerse the rack with eppendorf tubes into the methanol for ~5 minutes making sure the methanol is just below the cap.
4. Once the samples have frozen, remove them from the dry ice/methanol, and place them in a water bath containing water at room temperature. Allow samples to thaw completely.
5. Vortex vigorously.
6. Repeat steps #3-5 for a total of 3 freeze and thaw cycles.
7. Store samples at -80C (or -20C) until ready to assay.

B.2 ALP Assay

Solutions/Reagents

REAGENT	Recipe for working solution
1. 2-Amino-2-Methyl-1-Propanol (AMP) Stock: ct# A65182; liquid; MW 89.14; density 0.934 g/mL; *in the dry chem. shelf* Working solution: 1.5 M balance to pH 10.25 with HCl; store at 4C; good for 2 months	7.18 mL/42.82 mL (3.59 mL/21.41 mL) (in DDI water) (pH to 10.25)
2. Sigma 104 phosphatase substrate/p-Nitrophenyl phosphate disodium hexahydrate (pNPP) Stock: ct# 1040/ (new-P4744); crystalline; MW 371.14; *in the PCR room freezer* Working solution: 20 mM; store at 4C; **protect from light**; good for one month	371.14 mg/50 mL (185.57 mg/25 mL) (in DDI water) (protect from light)
3. $MgCl_2$ Stock: ct# M4880; powder; MW-95.22; *in the dry chem. shelf* Working solution: 10 mM; store at 4C; good for one week	47.61 mg/50 mL (in DDI water)
4. NaOH Stock: 10 N Working solution: 1 M; prepare 0.1mL/well; prepare fresh each day; maintain at room temperature	2 mL/18 mL (in DDI water)

5. 0.05% Triton X-100 in PBS	0.25 mL Triton X-100 to 500 mL PBS
6. Substrate working solution (AMP-pNPP-$MgCl_2$) Working solution: prepare fresh from above solutions each day; 0.05mL/well (except standards); maintain at room temperature	Combine #1,#2 and #3 in a 1:1:1 ratio
7. p-Nitrophenol standard (pNP) Stock: ct# N7660 (10 mM) Working solution: 800µM (Maximum standard); stored at 4C; **protect from light**	80 µL/920 µL (in 0.05% Triton-X 100 in PBS)

Procedure

1. Extract ALP by freeze/thawing (ALP-DNA extraction for mesh.doc), and store at -80C.
2. Thaw extracted samples at room temperature, and put on ice.
3. Dilute samples in 0.05% Triton X-100/PBS, if needed.
4. Prepare pNP standards in microcentrifuge tubes as follows:
    a. Dilute 80 µL of 10 mM pNP standard in 920 µL of 0.05% Triton X-100/PBS to get the 800 µM standard.
    b. Make an additional six serial dilutions in 0.05% Triton X-100/PBS, and reserve the eighth standard for a blank.

pNP stds (µM, nmol/mL)	800	400	200	100	50	25	12.5	0
Final pNP conc in 200 µl (µM)	200	100	50	25	12.5	6.25	3.125	0
pNP (nmol) in 50 µL	**40**	**20**	**10**	**5**	**2.5**	**1.25**	**0.625**	**0**

5. Pipette 50 µL of each standard in triplicate in rows A-H columns 1-3 of a clear Costar 96-well plate. Do this in the dark to protect from light.
6. Pipette 50 µL of each experimental sample in triplicate to the appropriate wells of the 96-well plate.
7. Add 50 µL of substrate working solution to all the wells containing the standards and experimental samples. Use either the repeater or the multipipetor.
8. Incubate at 37C for 1-3 hours. Watch for color change to yellow, and remove from incubator when color change is seen in majority of the wells. Note incubation time.
9. Immediately add 100 µL of the NaOH solution to all the wells containing the standards and experimental samples, and read at 405 nm.

Notes

- If enzyme is present at a high concentration, it may need to be diluted. At high enzyme concentrations all the substrate may be used up, and a saturation point will be reached before the end of the assay.
- All groups from one experiment need to be assayed at the same time to enable comparison. This is due to the fact that there may be subtle differences in the substrate working solution from lot to lot that may cause large differences in pNP produced in the same time period.

- By comparing the absorbance of the sample with the standards, we are able to find out how much pNP has been produced by the enzyme in our samples. The Y axis will be nmol of pNP produced by the enzyme (i.e. enzyme activity) in 500 µL of sample. The ALP enzyme is stable for 48 hours at 4C, and a few months at -20C.

B.3 DNA Assay

Solutions/Reagents

- PicoGreen dsDNA quantification kit (molecular probes cat# P11496)
  - PicoGreen dsDNA reagent
  - lambda DNA standard (100 ug/ml)
  - 20X TE buffer (200mM tris-HCL, 20 mM EDTA, pH 7.5)
- 0.05% triton-X100 in PBS
- 96-well black plates (Corning Costar #3915)
- Repeater

REAGENT	Recipe for working solution
1. TE buffer - 20X in kit; dilute to 1X - ~0.4mL/sample for dilution + ~10mL for standards + PicoGreen reagent volume	5 mL to 95 mL DNase-free water (2.5/47.5)
2. PicoGreen dsDNA reagent - dilute 1: 200 from kit; protect from light - 0.1mL/well	0.1 mL to 19.9 mL 1X TE (0.05/9.95)
3. Lambda DNA standard - 100 µg/ml in kit; dilute to 1 µg/mL	0.015 mL to 1.485 mL assay buffer

Procedure

1. Extract DNA into solution (by proteinase K digestion, freeze thaw etc.).
2. Thaw samples at room temperature.
3. Dilute samples in 1X TE to get <1000 ng/mL (<130,000 cells/mL). (For 24-well studies, 1:10 has been an appropriate dilution. Pipette 40 µL of sample into 360 µL of 1X TE.)
4. Prepare lambda DNA standards (this will be enough for 3 plates only):

µL of 1 µg/mL DNA	1000	100	10	1	0
µL of assay buffer	0	900	990	999	1000
DNA (ng/mL)	**1000**	**100**	**10**	**1**	**0**

5. If available, prepare standards from a known amount of cell suspension (e.g. 1e6/mL; enough for 3 plates):

µL of 1e6 cells/mL	100	10	1
µL of assay buffer	900	990	999
Cells (cells/mL)	**100,000**	**10,000**	**1,000**

6. Prepare PicoGreen working solution. This solution should be used within a few hours of its preparation.
7. Pipette 100 µL of standards and samples in triplicate to a **black** Costar 96-well plate.

8. In the dark, add 100 µL of working reagent to all the wells containing the standards and experimental samples. Use either the repeater (with the 5mL tip) or the multipipetor.
9. Incubate for 5 minutes at room temperature, protected from light.
10. Read the plate using the Perkins-Elmer HTS 7000 fluorescent plate reader at an excitation of 485-nm, emission of 535-nm and manual gain of 60 using the HTSoft program. Ensure that the reader is set for the Costar 96-well black plate (cos96fblk).

Notes

- Standards should be made up in the same solution that the assay samples are in. It is called the assay buffer in this protocol. For e.g. if the samples are in 0.05% Triton X-100, and I dilute them 1:10 in 1X TE, then make a 1:10 dilution of 0.05% Triton X-100 in 1X TE, and use this to make the standards. This is because the fluorescence intensity can change due to the presence of these other compounds.

B.4 Calcium Assay

Solutions/Reagents

- PBS
- 1N acetic acid
- Calcium reagent (Arsenazo III, Diagnostic Chemicals Limited # 140-24 (1L))
- Calcium standard (1 mg/ml)

Procedure

1. Wash samples 3X with **calcium free** PBS.

2. Remove samples from wells/plates and place in microcentrifuge tube with 500 µL of 1N acetic acid.
3. Vortex samples overnight in refrigerator.
4. If needed, spin samples down in small centrifuge on maximum speed for 8-10 minutes, and remove supernatant into fresh tubes.
5. Prepare standards (maximum 100 µg/mL, and 6 serial dilutions; in 1N acetic acid).
6. Pipette 25 µL of standards and samples in triplicate to a **clear** Costar 96-well plate.
7. Add 300 µL of reagent to each well (dilute samples if color change is more than maximum standard).
8. Incubate for 30 seconds at room temperature.
9. Read samples on plate reader at 650 nm (color is stable for 30 minutes).

Notes

- For cells in plates, put acid in plate overnight at 4C. Next day use cell scraper to scrape off the cells, and transfer cells and acid to microcentrifuge tubes. Vortex samples overnight in refrigerator.
- Store samples at -20C.
- According to the reagent manual, when using 20µL of sample and 2 mL of reagent (1/100 ratio), the assay is linear up to 200µg/mL. The linearity will depend on the ratio of sample/reagent used. When using the ratio above, the relationship is linear for < 20 µg/mL, but a quadratic equation fits the standards very well. A fourth order polynomial equation fits the standards almost perfectly.
- In the case of the ratio above, the saturation limit of the assay is ~175 µg/mL.
- To figure out the dilutions required for each group, you can compare color change in 1-2 samples from each group with the standards using n=1.

B.5 Calcein Staining

Solutions/Reagents

- PBS without Ions (PBS-)
- Calcein (Sigma # C0875-5G)
  - Make 1 mg/ml solution of calcein in PBS-. Not all calcein will go into solution. Mix well, and immediately dilute 1:10 in PBS- to get a 100µg/ml stock solution. Confirm that the pH is between 7.0-7.4. Sterile filter, wrap container with foil, and store at 4C.
- bisBenzimide H 33342 trihydrochloride (Hoechst 33342) (Sigma # B2261-500MG)
  - Make 10 mg/ml stock solution of the dye in DI water. Dilute 1:1000 in DI water to get a working solution of 10 µg/ml.

Procedure

1. On the take-down day, add calcein to the media such that the final concentration is 10 µg/ml. (for example, add 333µl of 100 µg/ml calcein to 3 ml media.)
2. Incubate for 4 hours in the incubator.
3. Wash 2X with PBS-.
4. Fix cells with 10% neutral buffered formalin for 10 minutes.
5. Wash 2X with DI water.
6. Add 10 µg/ml Hoechst dye solution, and incubate for 30 minutes at room temperature.
7. Wash 2X with DI water.
8. Take images using microscope.

Notes

- As an alternative to the 4 hour incubation, you can use 1 µg/ml calcein and incubate the cells for 24 hours. If continuous monitoring is required, 1 µg/ml calcein can be added throughout the culture period.

APPENDIX C

CAD DRAWINGS OF FIXATION PLATES

C.1 Polysulfone Plate

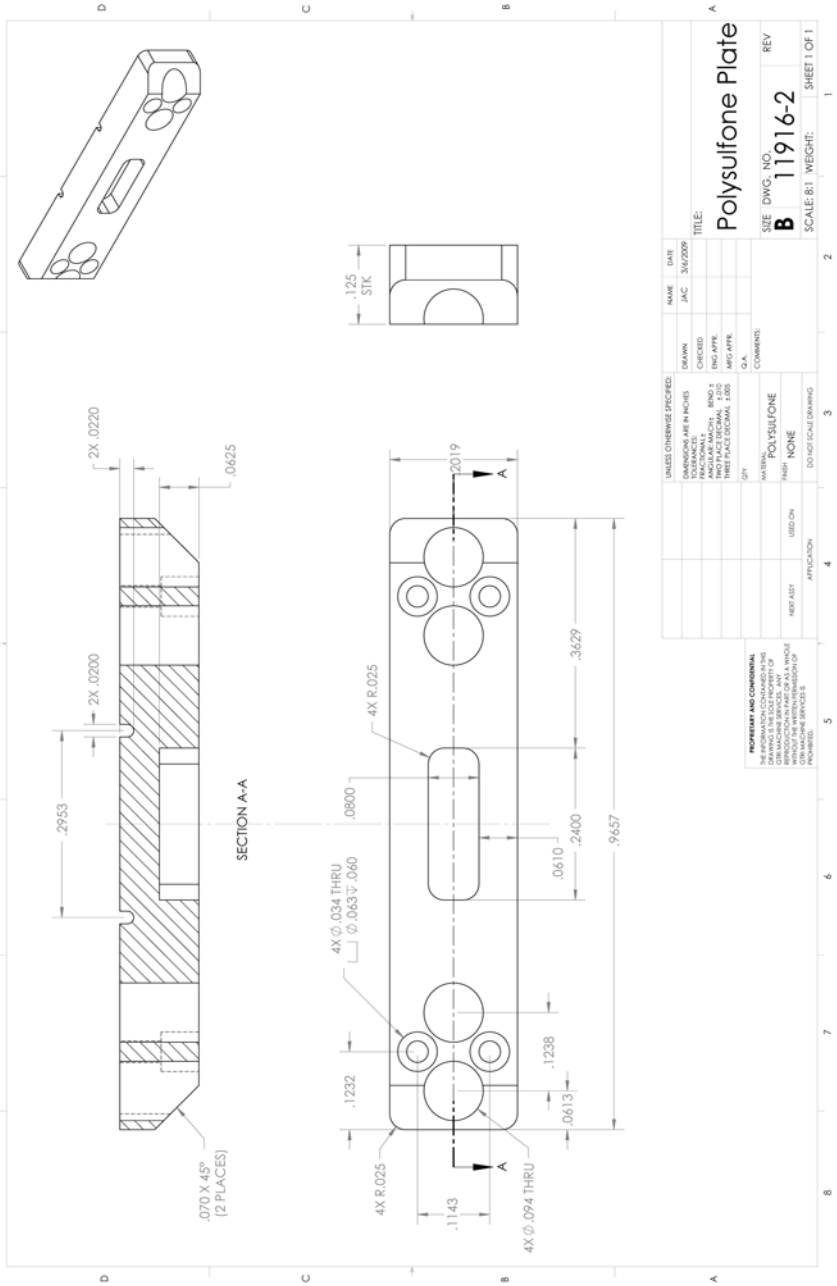

C.2 Stainless Steel Plate

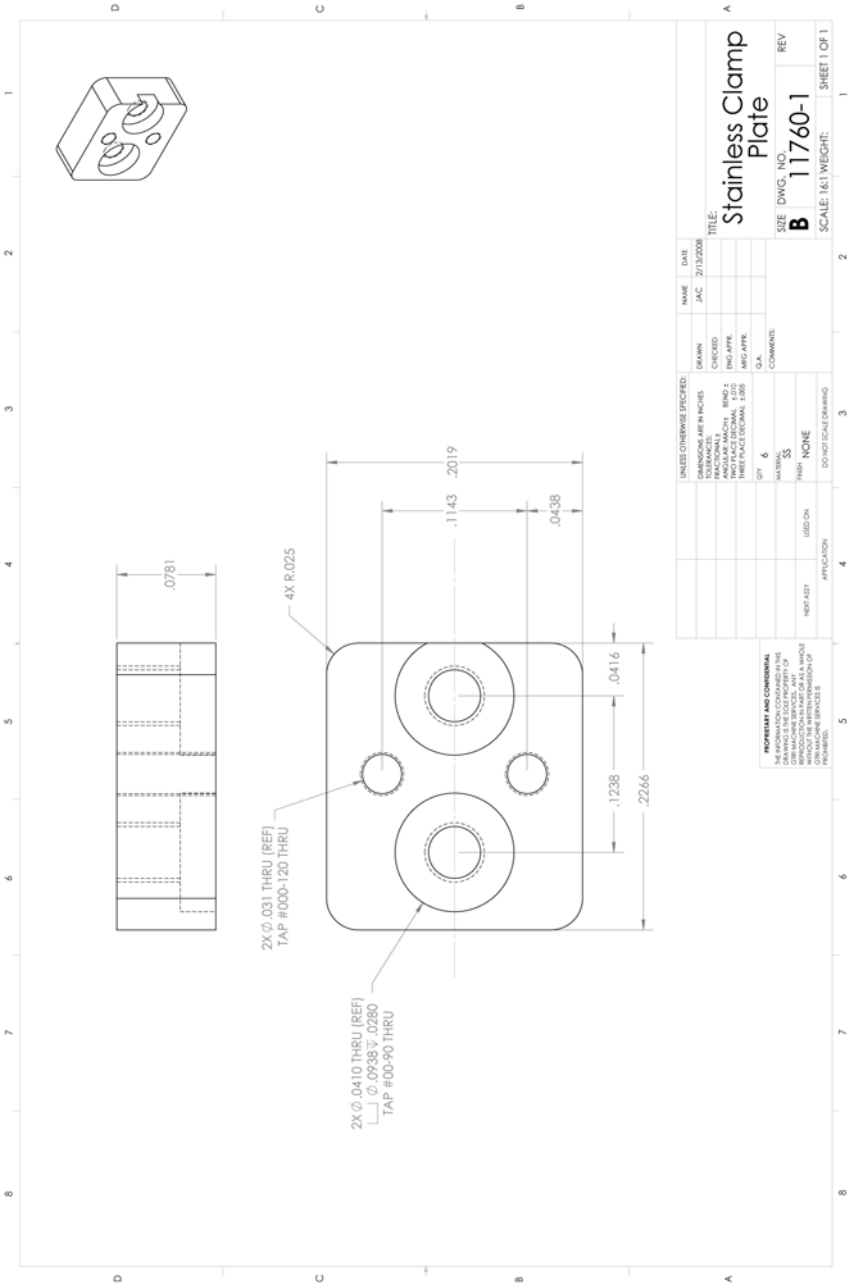

REFERENCES

1. Yaszemski, M.J., et al., *Evolution of bone transplantation: molecular, cellular and tissue strategies to engineer human bone.* Biomaterials, 1996. 17(2): p. 175-85.

2. Junqueira, L., J. Carneiro, and R. Kelley, *Bone*, in *Basic Histology*. 1989, Prentice Hall. p. 136-159.

3. Buckwalter, J.A., et al., *Bone biology. I: Structure, blood supply, cells, matrix, and mineralization.* Instr Course Lect, 1996. 45: p. 371-86.

4. Rey, C., et al., *The carbonate environment in bone mineral: a resolution-enhanced Fourier Transform Infrared Spectroscopy Study.* Calcif Tissue Int, 1989. 45(3): p. 157-64.

5. Rey, C., et al., *Non-apatitic environments in bone mineral: FT-IR detection, biological properties and changes in several disease states.* Connect Tissue Res, 1989. 21(1-4): p. 267-73.

6. Cooper, R.R., J.W. Milgram, and R.A. Robinson, *Morphology of the osteon. An electron microscopic study.* J Bone Joint Surg Am, 1966. 48(7): p. 1239-71.

7. Blair, H.C., et al., *Osteoclastic bone resorption by a polarized vacuolar proton pump.* Science, 1989. 245(4920): p. 855-7.

8. Beresford, J.N., *Osteogenic stem cells and the stromal system of bone and marrow.* Clin Orthop Relat Res, 1989(240): p. 270-80.

9. Taylor, J., *The periosteum and bone growth.* Bone, 1992. 6: p. 21–52.

10. Vogelin, E., et al., *Healing of a critical-sized defect in the rat femur with use of a vascularized periosteal flap, a biodegradable matrix, and bone morphogenetic protein.* J Bone Joint Surg Am, 2005. 87(6): p. 1323-31.

11. Muramatsu, K. and A.T. Bishop, *Cell repopulation in vascularized bone grafts.* J Orthop Res, 2002. 20(4): p. 772-8.

12. Hutmacher, D.W. and M. Sittinger, *Periosteal cells in bone tissue engineering.* Tissue Eng, 2003. 9 Suppl 1: p. S45-64.

13. Buckwalter, J.A., et al., *Bone biology. II: Formation, form, modeling, remodeling, and regulation of cell function.* Instr Course Lect, 1996. 45: p. 387-99.

14. Ferguson, C., et al., *Does adult fracture repair recapitulate embryonic skeletal formation?* Mech Dev, 1999. 87(1-2): p. 57-66.

15. Einhorn, T.A., *The cell and molecular biology of fracture healing.* Clin Orthop Relat Res, 1998(355 Suppl): p. S7-21.

16. Duvall, C.L., *The Role of Osteopontin in Postnatal Vascular Growth: Functional Effects in Ischemic Limb Collateral Vessel Formation and Long Bone Fracture Healing.* Ph.D. Thesis, Department of Biomedical Engineering, Georgia Institute of Technology, 2007.

17. McKibbin, B., *The biology of fracture healing in long bones.* J Bone Joint Surg Br, 1978. 60-B(2): p. 150-62.

18. Obert, L., F. Deschaseaux, and P. Garbuio, *Critical analysis and efficacy of BMPs in long bones non-union.* Injury, 2005. 36 Suppl 3: p. S38-42.

19. Reddi, A.H., *Role of morphogenetic proteins in skeletal tissue engineering and regeneration.* Nat Biotechnol, 1998. 16(3): p. 247-52.

20. Deckers, M.M., et al., *Bone morphogenetic proteins stimulate angiogenesis through osteoblast-derived vascular endothelial growth factor A.* Endocrinology, 2002. 143(4): p. 1545-53.

21. Hoffmann, A., et al., *Perspectives in the biological function, the technical and therapeutic application of bone morphogenetic proteins.* Appl Microbiol Biotechnol, 2001. 57(3): p. 294-308.

22. Epari, D.R., et al., *Instability prolongs the chondral phase during bone healing in sheep.* Bone, 2006. 38(6): p. 864-70.

23. Le, A.X., et al., *Molecular aspects of healing in stabilized and non-stabilized fractures.* J Orthop Res, 2001. 19(1): p. 78-84.

24. Lienau, J., et al., *Initial vascularization and tissue differentiation are influenced by fixation stability.* J Orthop Res, 2005. 23(3): p. 639-45.

25. Urist, M.R., *Bone: formation by autoinduction.* Science, 1965. 150(698): p. 893-9.

26. Wozney, J.M., et al., *Novel regulators of bone formation: molecular clones and activities.* Science, 1988. 242(4885): p. 1528-34.

27. Nakashima, M. and A.H. Reddi, *The application of bone morphogenetic proteins to dental tissue engineering.* Nat Biotechnol, 2003. 21(9): p. 1025-32.

28. Bessa, P.C., M. Casal, and R.L. Reis, *Bone morphogenetic proteins in tissue engineering: the road from the laboratory to the clinic, part I (basic concepts).* J Tissue Eng Regen Med, 2008. 2(1): p. 1-13.

29. J.R. Lieberman, A.D., T.A. Einhorn, *The Role of Growth Factors in the Repair of Bone: Biology and Clinical Applications.* The Journal of Bone and Joint Surgery, 2002. 84-A(6): p. 1032-1044.

30. Schmitt, J.M., et al., *Bone morphogenetic proteins: an update on basic biology and clinical relevance.* J Orthop Res, 1999. 17(2): p. 269-78.

31. Tsuji, K., et al., *BMP2 activity, although dispensable for bone formation, is required for the initiation of fracture healing.* Nat Genet, 2006. 38(12): p. 1424-9.

32. Reddi, A.H., *Initiation of fracture repair by bone morphogenetic proteins.* Clin Orthop Relat Res, 1998(355 Suppl): p. S66-72.

33. Amedee, J., et al., *Osteogenin (bone morphogenic protein 3) inhibits proliferation and stimulates differentiation of osteoprogenitors in human bone marrow.* Differentiation, 1994. 58(2): p. 157-64.

34. Long, M.W., et al., *Regulation of human bone marrow-derived osteoprogenitor cells by osteogenic growth factors.* J Clin Invest, 1995. 95(2): p. 881-7.

35. Rickard, D.J., et al., *Induction of rapid osteoblast differentiation in rat bone marrow stromal cell cultures by dexamethasone and BMP-2.* Dev Biol, 1994. 161(1): p. 218-28.

36. Lecanda, F., L.V. Avioli, and S.L. Cheng, *Regulation of bone matrix protein expression and induction of differentiation of human osteoblasts and human bone marrow stromal cells by bone morphogenetic protein-2.* J Cell Biochem, 1997. 67(3): p. 386-96.

37. Fiedler, J., et al., *BMP-2, BMP-4, and PDGF-bb stimulate chemotactic migration of primary human mesenchymal progenitor cells.* J Cell Biochem, 2002. 87(3): p. 305-12.

38. Mishima, Y. and M. Lotz, *Chemotaxis of human articular chondrocytes and mesenchymal stem cells.* J Orthop Res, 2008. 26(10): p. 1407-12.

39. M.P. Bostrom, N.P.C., *Potential Role of Bone Morphogenetic Proteins in Fracture Healing.* Clinical Orthopaedics and Related Research, 1998. 355S: p. S274-S282.

40. Bostrom, M.P., *Expression of bone morphogenetic proteins in fracture healing.* Clin Orthop Relat Res, 1998(355 Suppl): p. S116-23.

41. Bostrom, M.P., et al., *Immunolocalization and expression of bone morphogenetic proteins 2 and 4 in fracture healing.* J Orthop Res, 1995. 13(3): p. 357-67.

42. Onishi, T., et al., *Distinct and overlapping patterns of localization of bone morphogenetic protein (BMP) family members and a BMP type II receptor during fracture healing in rats.* Bone, 1998. 22(6): p. 605-12.

43. Govender, S., et al., *Recombinant human bone morphogenetic protein-2 for treatment of open tibial fractures: a prospective, controlled, randomized study of four hundred and fifty patients.* J Bone Joint Surg Am, 2002. 84-A(12): p. 2123-34.

44. MacKenzie, E.J., et al., *Long-term persistence of disability following severe lower-limb trauma. Results of a seven-year follow-up.* J Bone Joint Surg Am, 2005. 87(8): p. 1801-9.

45. Borrelli, J., Jr., W.D. Prickett, and W.M. Ricci, *Treatment of nonunions and osseous defects with bone graft and calcium sulfate.* Clin Orthop Relat Res, 2003(411): p. 245-54.

46. Starr, A.J., *Fracture repair: successful advances, persistent problems, and the psychological burden of trauma.* J Bone Joint Surg Am, 2008. 90 Suppl 1: p. 132-7.

47. Laurencin, C.T. and Y. Khan (2006) *Bone Graft Substitute Materials*. http://emedicine.medscape.com/article/1230616-overview

48. Simon, C.G., Jr., et al., *Preliminary report on the biocompatibility of a moldable, resorbable, composite bone graft consisting of calcium phosphate cement and poly(lactide-co-glycolide) microspheres.* J Orthop Res, 2002. 20(3): p. 473-82.

49. Cypher, T.J. and J.P. Grossman, *Biological principles of bone graft healing.* J Foot Ankle Surg, 1996. 35(5): p. 413-7.

50. Praemer, A., S. Furner, and D.P. Rice, *Musculoskeletal conditions in the United States*. 1999, American Academy of Orthopaedic Surgeons: Rosemont, IL.

51. Giannoudis, P.V., H. Dinopoulos, and E. Tsiridis, *Bone substitutes: an update.* Injury, 2005. 36 Suppl 3: p. S20-7.

52. Younger, E.M. and M.W. Chapman, *Morbidity at bone graft donor sites.* J Orthop Trauma, 1989. 3(3): p. 192-5.

53. Arrington, E.D., et al., *Complications of iliac crest bone graft harvesting.* Clin Orthop Relat Res, 1996(329): p. 300-9.

54. Prolo, D.J. and J.J. Rodrigo, *Contemporary bone graft physiology and surgery.* Clin Orthop Relat Res, 1985(200): p. 322-42.

55. Berrey, B.H., Jr., et al., *Fractures of allografts. Frequency, treatment, and end-results.* J Bone Joint Surg Am, 1990. 72(6): p. 825-33.

56. Wheeler, D.L. and W.F. Enneking, *Allograft bone decreases in strength in vivo over time.* Clin Orthop Relat Res, 2005(435): p. 36-42.

57. Papakostidis, C., et al., *Efficacy of autologous iliac crest bone graft and bone morphogenetic proteins for posterolateral fusion of lumbar spine: a meta-analysis of the results.* Spine (Phila Pa 1976), 2008. 33(19): p. E680-92.

58. Friedlaender, G.E., et al., *Osteogenic protein-1 (bone morphogenetic protein-7) in the treatment of tibial nonunions.* J Bone Joint Surg Am, 2001. 83-A Suppl 1(Pt 2): p. S151-8.

59. Kanakaris, N.K., et al., *Application of BMP-7 to tibial non-unions: a 3-year multicenter experience.* Injury, 2008. 39 Suppl 2: p. S83-90.

60. Cahill, K.S., et al., *Prevalence, complications, and hospital charges associated with use of bone-morphogenetic proteins in spinal fusion procedures.* JAMA, 2009. 302(1): p. 58-66.

61. Benglis, D., M.Y. Wang, and A.D. Levi, *A comprehensive review of the safety profile of bone morphogenetic protein in spine surgery.* Neurosurgery, 2008. 62(5 Suppl 2): p. ONS423-31; discussion ONS431.

62. Dahabreh, Z., et al., *A cost analysis of treatment of tibial fracture nonunion by bone grafting or bone morphogenetic protein-7.* Int Orthop, 2008.

63. Garrison, K.R., et al., *Clinical effectiveness and cost-effectiveness of bone morphogenetic proteins in the non-healing of fractures and spinal fusion: a systematic review.* Health Technol Assess, 2007. 11(30): p. 1-150, iii-iv.

64. Rose, F.R. and R.O. Oreffo, *Bone tissue engineering: hope vs hype.* Biochem Biophys Res Commun, 2002. 292(1): p. 1-7.

65. Salgado, A.J., O.P. Coutinho, and R.L. Reis, *Bone tissue engineering: state of the art and future trends.* Macromol Biosci, 2004. 4(8): p. 743-65.

66. Langer, R. and J.P. Vacanti, *Tissue engineering.* Science, 1993. 260(5110): p. 920-6.

67. Tabata, Y., *Tissue regeneration based on growth factor release.* Tissue Eng, 2003. 9 Suppl 1: p. S5-15.

68. Parenteau, N., *Skin: the first tissue-engineered products.* Sci Am, 1999. 280(4): p. 83-4.

69. Gemmiti, C.V. and R.E. Guldberg, *Fluid flow increases type II collagen deposition and tensile mechanical properties in bioreactor-grown tissue-engineered cartilage.* Tissue Eng, 2006. 12(3): p. 469-79.

70. Lima, E.G., et al., *Functional tissue engineering of chondral and osteochondral constructs.* Biorheology, 2004. 41(3-4): p. 577-90.

71. Porter, B.D., et al., *Noninvasive image analysis of 3D construct mineralization in a perfusion bioreactor.* Biomaterials, 2007. 28(15): p. 2525-33.

72. Pelled, G., et al., *Direct Gene Therapy for Bone Regeneration: Gene Delivery, Animal Models and Outcome Measures.* Tissue Eng Part A, 2009.

73. Kempen, D.H., et al., *Effect of local sequential VEGF and BMP-2 delivery on ectopic and orthotopic bone regeneration.* Biomaterials, 2009. 30(14): p. 2816-25.

74. Oest, M.E., et al., *Quantitative assessment of scaffold and growth factor-mediated repair of critically sized bone defects.* J Orthop Res, 2007. 25(7): p. 941-50.

75. Nerem, R.M., *Tissue engineering: the hope, the hype, and the future.* Tissue Eng, 2006. 12(5): p. 1143-50.

76. Guldberg, R.E., *Spatiotemporal Delivery Strategies for Promoting Musculoskeletal Tissue Regeneration.* J Bone Miner Res, 2009.

77. Guldberg, R.E., et al., *Biologic augmentation of polymer scaffolds for bone repair.* J Musculoskelet Neuronal Interact, 2007. 7(4): p. 333-4.

78. Patterson, T.E., et al., *Cellular strategies for enhancement of fracture repair.* J Bone Joint Surg Am, 2008. 90 Suppl 1: p. 111-9.

79. Giannoudis, P.V., et al., *The diamond concept--open questions.* Injury, 2008. 39 Suppl 2: p. S5-8.

80. Gamradt, S.C. and J.R. Lieberman, *Genetic modification of stem cells to enhance bone repair.* Ann Biomed Eng, 2004. 32(1): p. 136-47.

81. Phillips, J.E., et al., *Mineralization capacity of Runx2/Cbfa1-genetically engineered fibroblasts is scaffold dependent.* Biomaterials, 2006. 27(32): p. 5535-45.

82. Petrie, T.A., et al., *Simple application of fibronectin-mimetic coating enhances osseointegration of titanium implants.* J Cell Mol Med, 2008.

83. Friess, W., et al., *Bone regeneration with recombinant human bone morphogenetic protein-2 (rhBMP-2) using absorbable collagen sponges (ACS): influence of processing on ACS characteristics and formulation.* Pharm Dev Technol, 1999. 4(3): p. 387-96.

84. Hosseinkhani, H., et al., *Osteogenic differentiation of mesenchymal stem cells in self-assembled peptide-amphiphile nanofibers.* Biomaterials, 2006. 27(22): p. 4079-86.

85. Lee, J.Y., et al., *Osteoblastic differentiation of human bone marrow stromal cells in self-assembled BMP-2 receptor-binding peptide-amphiphiles.* Biomaterials, 2009. 30(21): p. 3532-41.

86. Malafaya, P.B., G.A. Silva, and R.L. Reis, *Natural-origin polymers as carriers and scaffolds for biomolecules and cell delivery in tissue engineering applications.* Adv Drug Deliv Rev, 2007. 59(4-5): p. 207-33.

87. Hutmacher, D.W., et al., *Mechanical properties and cell cultural response of polycaprolactone scaffolds designed and fabricated via fused deposition modeling.* J Biomed Mater Res, 2001. 55(2): p. 203-16.

88. Lin, A.S., et al., *Microarchitectural and mechanical characterization of oriented porous polymer scaffolds.* Biomaterials, 2003. 24(3): p. 481-9.

89. Dean, D., et al., *Poly(propylene fumarate) and poly(DL-lactic-co-glycolic acid) as scaffold materials for solid and foam-coated composite tissue-engineered constructs for cranial reconstruction.* Tissue Eng, 2003. 9(3): p. 495-504.

90. Murugan, R. and S. Ramakrishna, *Nano-featured scaffolds for tissue engineering: a review of spinning methodologies.* Tissue Eng, 2006. 12(3): p. 435-47.

91. Chu, T.M., et al., *Segmental bone regeneration using a load-bearing biodegradable carrier of bone morphogenetic protein-2.* Biomaterials, 2007. 28(3): p. 459-67.

92. Meinig, R.P., *Polylactide membranes in the treatment of segmental diaphyseal defects: animal model experiments in the rabbit radius, sheep tibia, Yucatan minipig radius, and goat tibia.* Injury, 2002. 33 Suppl 2: p. B58-65.

93. Gugala, Z. and S. Gogolewski, *Healing of critical-size segmental bone defects in the sheep tibiae using bioresorbable polylactide membranes.* Injury, 2002. 33 Suppl 2: p. B71-6.

94. Giardino, R., et al., *Bioabsorbable scaffold for in situ bone regeneration.* Biomed Pharmacother, 2006. 60(8): p. 386-92.

95. Jung, U.W., et al., *Effects of a chitosan membrane coated with polylactic and polyglycolic acid on bone regeneration in a rat calvarial defect.* Biomed Mater, 2007. 2(3): p. S101-5.

96. Kim, K.H., et al., *Biological efficacy of silk fibroin nanofiber membranes for guided bone regeneration.* J Biotechnol, 2005. 120(3): p. 327-39.

97. Matthews, J.A., et al., *Electrospinning of collagen nanofibers.* Biomacromolecules, 2002. 3(2): p. 232-8.

98. Pham, Q.P., U. Sharma, and A.G. Mikos, *Electrospinning of polymeric nanofibers for tissue engineering applications: a review.* Tissue Eng, 2006. 12(5): p. 1197-211.

99. Lee, K.Y. and D.J. Mooney, *Hydrogels for tissue engineering.* Chem Rev, 2001. 101(7): p. 1869-79.

100. Lutolf, M.P., et al., *Synthetic matrix metalloproteinase-sensitive hydrogels for the conduction of tissue regeneration: engineering cell-invasion characteristics.* Proc Natl Acad Sci U S A, 2003. 100(9): p. 5413-8.

101. De Biase, P. and R. Capanna, *Clinical applications of BMPs.* Injury, 2005. 36 Suppl 3: p. S43-6.

102. Critchlow, M.A., Y.S. Bland, and D.E. Ashhurst, *The effect of exogenous transforming growth factor-beta 2 on healing fractures in the rabbit.* Bone, 1995. 16(5): p. 521-7.

103. Street, J., et al., *Vascular endothelial growth factor stimulates bone repair by promoting angiogenesis and bone turnover.* Proc Natl Acad Sci U S A, 2002. 99(15): p. 9656-61.

104. Schliephake, H., *Bone growth factors in maxillofacial skeletal reconstruction.* International Journal of Oral & Maxillofacial Surgery, 2002. 31(5): p. 469-484.

105. Simmons, C.A., et al., *Dual growth factor delivery and controlled scaffold degradation enhance in vivo bone formation by transplanted bone marrow stromal cells.* Bone, 2004. 35(2): p. 562-9.

106. Huang, Y.C., et al., *Combined angiogenic and osteogenic factor delivery enhances bone marrow stromal cell-driven bone regeneration.* J Bone Miner Res, 2005. 20(5): p. 848-57.

107. Oest, M.E., *Dual Osteogenic and Angiogenic Growth Factor Delivery as a Treatment For Segmental Bone Defects.* Ph.D. Thesis, Biomedical Engineering, Georgia Institute of Technology, 2007.

108. Muhonen, V., et al., *Fibronectin modulates osteoblast behavior on Nitinol.* J Biomed Mater Res A, 2009. 88(3): p. 787-96.

109. Bernhardt, R., et al., *Osteoconductive modifications of Ti-implants in a goat defect model: characterization of bone growth with SR muCT and histology.* Biomaterials, 2005. 26(16): p. 3009-19.

110. Lutolf, M.P. and J.A. Hubbell, *Synthetic biomaterials as instructive extracellular microenvironments for morphogenesis in tissue engineering.* Nat Biotechnol, 2005. 23(1): p. 47-55.

111. Hilbig, H., et al., *Implant surface coatings with bone sialoprotein, collagen, and fibronectin and their effects on cells derived from human maxillar bone.* Eur J Med Res, 2007. 12(1): p. 6-12.

112. Saito, A., et al., *Activation of osteo-progenitor cells by a novel synthetic peptide derived from the bone morphogenetic protein-2 knuckle epitope.* Biochim Biophys Acta, 2003. 1651(1-2): p. 60-7.

113. Saito, A., et al., *Repair of 20-mm long rabbit radial bone defects using BMP-derived peptide combined with an alpha-tricalcium phosphate scaffold.* J Biomed Mater Res A, 2006. 77(4): p. 700-6.

114. Saito, A., et al., *Prolonged ectopic calcification induced by BMP-2-derived synthetic peptide.* J Biomed Mater Res A, 2004. 70(1): p. 115-21.

115. Sakiyama-Elbert, S. and J. Hubbell, *FUNCTIONAL BIOMATERIALS: Design of Novel Biomaterials.* Annual Review of Materials Research, 2001. 31(1): p. 183-201.

116. Garcia, A.J. and C.D. Reyes, *Bio-adhesive surfaces to promote osteoblast differentiation and bone formation.* J Dent Res, 2005. 84(5): p. 407-13.

117. Mizuno, M., R. Fujisawa, and Y. Kuboki, *Type I collagen-induced osteoblastic differentiation of bone-marrow cells mediated by collagen-alpha2beta1 integrin interaction.* J Cell Physiol, 2000. 184(2): p. 207-13.

118. Mizuno, M. and Y. Kuboki, *Osteoblast-related gene expression of bone marrow cells during the osteoblastic differentiation induced by type I collagen.* J Biochem (Tokyo), 2001. 129(1): p. 133-8.

119. Xiao, G., et al., *Role of the alpha2-integrin in osteoblast-specific gene expression and activation of the Osf2 transcription factor.* J Biol Chem, 1998. 273(49): p. 32988-94.

120. Reyes, C.D. and A.J. Garcia, *Alpha2beta1 integrin-specific collagen-mimetic surfaces supporting osteoblastic differentiation.* J Biomed Mater Res A, 2004. 69(4): p. 591-600.

121. Reyes, C.D., et al., *Biomolecular surface coating to enhance orthopaedic tissue healing and integration.* Biomaterials, 2007. 28(21): p. 3228-35.

122. Bruder, S.P. and B.S. Fox, *Tissue engineering of bone. Cell based strategies.* Clin Orthop Relat Res, 1999(367 Suppl): p. S68-83.

123. Hunziker, E.B., *Articular cartilage repair: basic science and clinical progress. A review of the current status and prospects.* Osteoarthritis Cartilage, 2002. 10(6): p. 432-63.

124. Song, L., D. Baksh, and R.S. Tuan, *Mesenchymal stem cell-based cartilage tissue engineering: cells, scaffold and biology.* Cytotherapy, 2004. 6(6): p. 596-601.

125. Bruder, S.P., et al., *The effect of implants loaded with autologous mesenchymal stem cells on the healing of canine segmental bone defects.* J Bone Joint Surg Am, 1998. 80(7): p. 985-96.

126. Bruder, S.P., et al., *Bone regeneration by implantation of purified, culture-expanded human mesenchymal stem cells.* J Orthop Res, 1998. 16(2): p. 155-62.

127. Kadiyala, S., et al., *Culture expanded canine mesenchymal stem cells possess osteochondrogenic potential in vivo and in vitro.* Cell Transplant, 1997. 6(2): p. 125-34.

128. McCulloch, C.A., et al., *Osteogenic progenitor cells in rat bone marrow stromal populations exhibit self-renewal in culture.* Blood, 1991. 77(9): p. 1906-11.

129. Banfi, A., et al., *Replicative aging and gene expression in long-term cultures of human bone marrow stromal cells.* Tissue Eng, 2002. 8(6): p. 901-10.

130. Quarto, R., D. Thomas, and C.T. Liang, *Bone progenitor cell deficits and the age-associated decline in bone repair capacity.* Calcif Tissue Int, 1995. 56(2): p. 123-9.

131. D'Ippolito, G., et al., *Age-related osteogenic potential of mesenchymal stromal stem cells from human vertebral bone marrow.* J Bone Miner Res, 1999. 14(7): p. 1115-22.

132. De Coppi, P., et al., *Isolation of amniotic stem cell lines with potential for therapy.* Nat Biotechnol, 2007. 25(1): p. 100-6.

133. Peister, A., et al., *Osteogenic differentiation of amniotic fluid stem cells* in *53rd annual meeting of the Orthopaedic Research Society*. 2007: San Diego, CA.

134. Kolambkar, Y.M., et al., *Chondrogenic differentiation of amniotic fluid-derived stem cells.* J Mol Histol, 2007. 38(5): p. 405-13.

135. Gersbach, C.A., et al., *Runx2/Cbfa1-genetically engineered skeletal myoblasts mineralize collagen scaffolds in vitro.* Biotechnol Bioeng, 2004. 88(3): p. 369-78.

136. Ishaug-Riley, S.L., et al., *Three-dimensional culture of rat calvarial osteoblasts in porous biodegradable polymers.* Biomaterials, 1998. 19(15): p. 1405-12.

137. Byers, B.A., R.E. Guldberg, and A.J. Garcia, *Synergy between genetic and tissue engineering: Runx2 overexpression and in vitro construct development enhance in vivo mineralization.* Tissue Eng, 2004. 10(11-12): p. 1757-66.

138. Cartmell, S., et al., *Quantitative microcomputed tomography analysis of mineralization within three-dimensional scaffolds in vitro.* J Biomed Mater Res, 2004. 69A(1): p. 97-104.

139. Thorrez, L., et al., *Growth, differentiation, transplantation and survival of human skeletal myofibers on biodegradable scaffolds.* Biomaterials, 2008. 29(1): p. 75-84.

140. Jager, M., et al., *Bone healing and migration of cord blood-derived stem cells into a critical size femoral defect after xenotransplantation.* J Bone Miner Res, 2007. 22(8): p. 1224-33.

141. Zhang, X., et al., *Periosteal progenitor cell fate in segmental cortical bone graft transplantations: implications for functional tissue engineering.* J Bone Miner Res, 2005. 20(12): p. 2124-37.

142. Boontheekul, T. and D.J. Mooney, *Protein-based signaling systems in tissue engineering.* Curr Opin Biotechnol, 2003. 14(5): p. 559-65.

143. Chen, R.R. and D.J. Mooney, *Polymeric growth factor delivery strategies for tissue engineering.* Pharm Res, 2003. 20(8): p. 1103-12.

144. Paramore, C.G., et al., *The safety of OP-1 for lumbar fusion with decompression--a canine study.* Neurosurgery, 1999. 44(5): p. 1151-5; discussion 1155-6.

145. Li, R.H. and J.M. Wozney, *Delivering on the promise of bone morphogenetic proteins.* Trends Biotechnol, 2001. 19(7): p. 255-65.

146. Einhorn, T.A., et al., *A single percutaneous injection of recombinant human bone morphogenetic protein-2 accelerates fracture repair.* J Bone Joint Surg Am, 2003. 85-A(8): p. 1425-35.

147. Rose, F.R., Q. Hou, and R.O. Oreffo, *Delivery systems for bone growth factors - the new players in skeletal regeneration.* J Pharm Pharmacol, 2004. 56(4): p. 415-27.

148. Bessa, P.C., M. Casal, and R.L. Reis, *Bone morphogenetic proteins in tissue engineering: the road from laboratory to clinic, part II (BMP delivery).* J Tissue Eng Regen Med, 2008. 2(2-3): p. 81-96.

149. Schmidmaier, G., et al., *Carrier systems and application of growth factors in orthopaedics.* Injury, 2008. 39 Suppl 2: p. S37-43.

150. Issa, J.P., et al., *Sustained release carriers used to delivery bone morphogenetic proteins in the bone healing process.* Anat Histol Embryol, 2008. 37(3): p. 181-7.

151. Bulpitt, P. and D. Aeschlimann, *New strategy for chemical modification of hyaluronic acid: preparation of functionalized derivatives and their use in the formation of novel biocompatible hydrogels.* J Biomed Mater Res, 1999. 47(2): p. 152-69.

152. Park, D.J., et al., *Injectable bone using chitosan-alginate gel/mesenchymal stem cells/BMP-2 composites.* J Craniomaxillofac Surg, 2005. 33(1): p. 50-4.

153. Uludag, H., et al., *rhBMP-collagen sponges as osteoinductive devices: effects of in vitro sponge characteristics and protein pI on in vivo rhBMP pharmacokinetics.* Ann N Y Acad Sci, 1999. 875: p. 369-78.

154. Seeherman, H., et al., *rhBMP-2/calcium phosphate matrix accelerates osteotomy-site healing in a nonhuman primate model at multiple treatment times and concentrations.* J Bone Joint Surg Am, 2006. 88(1): p. 144-60.

155. Kato, M., et al., *Ectopic bone formation in mice associated with a lactic acid/dioxanone/ethylene glycol copolymer-tricalcium phosphate composite with added recombinant human bone morphogenetic protein-2.* Biomaterials, 2006. 27(21): p. 3927-33.

156. Mayer, M., et al., *Maxillary alveolar cleft repair in dogs using recombinant human bone morphogenetic protein-2 and a polymer carrier.* Plast Reconstr Surg, 1996. 98(2): p. 247-59.

157. Fisher, J.P., et al., *Thermoreversible hydrogel scaffolds for articular cartilage engineering.* J Biomed Mater Res A, 2004. 71(2): p. 268-74.

158. Lee, S., et al., *Polyketal microparticles: a new delivery vehicle for superoxide dismutase.* Bioconjug Chem, 2007. 18(1): p. 4-7.

159. Winn, S.R., H. Uludag, and J.O. Hollinger, *Carrier systems for bone morphogenetic proteins.* Clin Orthop Relat Res, 1999(367 Suppl): p. S95-106.

160. Uludag, H., et al., *Delivery systems for BMPs: factors contributing to protein retention at an application site.* J Bone Joint Surg Am, 2001. 83-A Suppl 1(Pt 2): p. S128-35.

161. Asher, D.M., *The transmissible spongiform encephalopathy agents: concerns and responses of United States regulatory agencies in maintaining the safety of biologics.* Dev Biol Stand, 1999. 100: p. 103-18.

162. Olsen, D., et al., *Recombinant collagen and gelatin for drug delivery.* Adv Drug Deliv Rev, 2003. 55(12): p. 1547-67.

163. Tada, H., et al., *Preshaped hydroxyapatite tricalcium-phosphate implant using three-dimensional computed tomography in the reconstruction of bone deformities of craniomaxillofacial region.* J Craniofac Surg, 2002. 13(2): p. 287-92.

164. Elisseeff, J., et al., *Advances in skeletal tissue engineering with hydrogels.* Orthod Craniofac Res, 2005. 8(3): p. 150-61.

165. Drury, J.L. and D.J. Mooney, *Hydrogels for tissue engineering: scaffold design variables and applications.* Biomaterials, 2003. 24(24): p. 4337-51.

166. Eckardt, H., et al., *Recombinant human bone morphogenetic protein 2 enhances bone healing in an experimental model of fractures at risk of non-union.* Injury, 2005. 36(4): p. 489-94.

167. Tabata, Y., et al., *Bone formation at a rabbit skull defect by autologous bone marrow cells combined with gelatin microspheres containing TGF-beta1.* J Biomater Sci Polym Ed, 2000. 11(8): p. 891-901.

168. Hong, L., et al., *Promoted bone healing at a rabbit skull gap between autologous bone fragment and the surrounding intact bone with biodegradable microspheres containing transforming growth factor-beta1.* Tissue Eng, 2000. 6(4): p. 331-40.

169. Rizzi, S.C., et al., *Recombinant protein-co-PEG networks as cell-adhesive and proteolytically degradable hydrogel matrixes. Part II: biofunctional characteristics.* Biomacromolecules, 2006. 7(11): p. 3019-29.

170. Wee, S. and W.R. Gombotz, *Protein release from alginate matrices.* Adv Drug Deliv Rev, 1998. 31(3): p. 267-285.

171. Augst, A.D., H.J. Kong, and D.J. Mooney, *Alginate hydrogels as biomaterials.* Macromol Biosci, 2006. 6(8): p. 623-33.

172. Lee, K.Y., et al., *Controlled growth factor release from synthetic extracellular matrices.* Nature, 2000. 408(6815): p. 998-1000.

173. Alsberg, E., et al., *Cell-interactive alginate hydrogels for bone tissue engineering.* J Dent Res, 2001. 80(11): p. 2025-9.

174. Alsberg, E., et al., *Regulating bone formation via controlled scaffold degradation.* J Dent Res, 2003. 82(11): p. 903-8.

175. Eickholz, P., et al., *Long-term results of guided tissue regeneration therapy with non-resorbable and bioabsorbable barriers. III. Class II furcations after 10 years.* J Periodontol, 2006. 77(1): p. 88-94.

176. Mengel, R., D. Schreiber, and L. Flores-de-Jacoby, *Bioabsorbable membrane and bioactive glass in the treatment of intrabony defects in patients with generalized aggressive periodontitis: results of a 5-year clinical and radiological study.* J Periodontol, 2006. 77(10): p. 1781-7.

177. Zucchelli, G., et al., *Enamel matrix proteins and guided tissue regeneration with titanium-reinforced expanded polytetrafluoroethylene membranes in the treatment of infrabony defects: a comparative controlled clinical trial.* J Periodontol, 2002. 73(1): p. 3-12.

178. Zybutz, M.D., et al., *Treatment of intrabony defects with resorbable materials, non-resorbable materials and flap debridement.* J Clin Periodontol, 2000. 27(3): p. 169-78.

179. Nasser, N.J., et al., *Guided bone regeneration in the treatment of segmental diaphyseal defects: a comparison between resorbable and non-resorbable membranes.* Injury, 2005. 36(12): p. 1460-6.

180. Nyman, R., et al., *Influence of bone marrow on membrane-guided bone regeneration of segmental long-bone defects in rabbits.* Scand J Plast Reconstr Surg Hand Surg, 2001. 35(3): p. 239-46.

181. Meinig, R.P., et al., *Bone regeneration with resorbable polymeric membranes: treatment of diaphyseal bone defects in the rabbit radius with poly(L-lactide) membrane. A pilot study.* J Orthop Trauma, 1996. 10(3): p. 178-90.

182. Pineda, L.M., et al., *Bone regeneration with resorbable polymeric membranes. III. Effect of poly(L-lactide) membrane pore size on the bone healing process in large defects.* J Biomed Mater Res, 1996. 31(3): p. 385-94.

183. Gerber, A. and S. Gogolewski, *Reconstruction of large segmental defects in the sheep tibia using polylactide membranes. A clinical and radiographic report.* Injury, 2002. 33 Suppl 2: p. B43-57.

184. Mosheiff, R., et al., *Quantification of guided regeneration of weight-bearing bones.* Orthopedics, 2003. 26(8): p. 789-94.

185. Leong, K.F., C.M. Cheah, and C.K. Chua, *Solid freeform fabrication of three-dimensional scaffolds for engineering replacement tissues and organs.* Biomaterials, 2003. 24(13): p. 2363-78.

186. Pham, Q.P., U. Sharma, and A.G. Mikos, *Electrospun poly(epsilon-caprolactone) microfiber and multilayer nanofiber/microfiber scaffolds: characterization of scaffolds and measurement of cellular infiltration.* Biomacromolecules, 2006. 7(10): p. 2796-805.

187. Barnes, C.P., et al., *Nanofiber technology: Designing the next generation of tissue engineering scaffolds.* Adv Drug Deliv Rev, 2007.

188. Tan, S.H., et al., *Systematic parameter study for ultra-fine fiber fabrication via electrospinning process.* Polymer, 2005. 46(16): p. 6128-6134.

189. Venugopal, J.R., Y. Zhang, and S. Ramakrishna, *In vitro culture of human dermal fibroblasts on electrospun polycaprolactone collagen nanofibrous membrane.* Artif Organs, 2006. 30(6): p. 440-6.

190. Kwon, I.K., S. Kidoaki, and T. Matsuda, *Electrospun nano- to microfiber fabrics made of biodegradable copolyesters: structural characteristics, mechanical properties and cell adhesion potential.* Biomaterials, 2005. 26(18): p. 3929-39.

191. Xin, X., M. Hussain, and J.J. Mao, *Continuing differentiation of human mesenchymal stem cells and induced chondrogenic and osteogenic lineages in electrospun PLGA nanofiber scaffold.* Biomaterials, 2007. 28(2): p. 316-25.

192. Badami, A.S., et al., *Effect of fiber diameter on spreading, proliferation, and differentiation of osteoblastic cells on electrospun poly(lactic acid) substrates.* Biomaterials, 2006. 27(4): p. 596-606.

193. Piskin, E., et al., *In vivo performance of simvastatin-loaded electrospun spiral-wound polycaprolactone scaffolds in reconstruction of cranial bone defects in the rat model.* J Biomed Mater Res A, 2009. 90(4): p. 1137-51.

194. Min, B.M., et al., *Electrospinning of silk fibroin nanofibers and its effect on the adhesion and spreading of normal human keratinocytes and fibroblasts in vitro.* Biomaterials, 2004. 25(7-8): p. 1289-97.

195. McManus, M.C., et al., *Electrospun fibrinogen: feasibility as a tissue engineering scaffold in a rat cell culture model.* J Biomed Mater Res A, 2007. 81(2): p. 299-309.

196. Zhang, Y., et al., *Electrospinning of gelatin fibers and gelatin/PCL composite fibrous scaffolds.* J Biomed Mater Res B Appl Biomater, 2005. 72(1): p. 156-65.

197. Buttafoco, L., et al., *Electrospinning of collagen and elastin for tissue engineering applications.* Biomaterials, 2006. 27(5): p. 724-34.

198. Schiffman, J.D. and C.L. Schauer, *One-step electrospinning of cross-linked chitosan fibers.* Biomacromolecules, 2007. 8(9): p. 2665-7.

199. Barnes, C.P., et al., *Cross-linking electrospun type II collagen tissue engineering scaffolds with carbodiimide in ethanol.* Tissue Eng, 2007. 13(7): p. 1593-605.

200. Chiu, J.B., et al., *Functionalization of poly(L-lactide) nanofibrous scaffolds with bioactive collagen molecules.* J Biomed Mater Res A, 2007. 83(4): p. 1117-27.

201. He, W., et al., *Fabrication of collagen-coated biodegradable polymer nanofiber mesh and its potential for endothelial cells growth.* Biomaterials, 2005. 26(36): p. 7606-15.

202. Doshi, J. and D. Reneker, *Electrospinning process and applications of electrospun fibers.* Journal of Electrostatics, 1995. 35(2): p. 151-160.

203. Fong, H., I. Chun, and D. Reneker, *Beaded nanofibers formed during electrospinning.* Polymer, 1999. 40: p. 4585-4592.

204. Gupta, P., et al., *Electrospinning of linear homopolymers of poly (methyl methacrylate): exploring relationships between fiber formation, viscosity, molecular weight and concentration in a good solvent.* Polymer, 2005. 46(13): p. 4799-4810.

205. Fong, H. and D. Reneker, *Electrospinning and the formation of nanofibers*, in *Structure Formation in Polymeric Fibers*, D.R. Salem, Editor. 2001, Carl Hanser Verlag: Munich, Germany.

206. He, W., et al., *Biodegradable polymer nanofiber mesh to maintain functions of endothelial cells.* Tissue Eng, 2006. 12(9): p. 2457-66.

207. Ryu, Y.J., et al., *Transport properties of electrospun nylon 6 nonwoven mats.* European Polymer Journal, 2003. 39(9): p. 1883-1889.

208. Baker, B.M. and R.L. Mauck, *The effect of nanofiber alignment on the maturation of engineered meniscus constructs.* Biomaterials, 2007. 28(11): p. 1967-77.

209. Siddiqui, M.M. and A. Atala, *Amniotic fluid-derived pluripotential cells*, in *Handbook of Stem Cells*, G.J. Lanza R, Hogan B, Editor. 2004, Academic Press: Philadelphia. p. 175-179.

210. Delo, D.M., et al., *Amniotic fluid and placental stem cells.* Methods Enzymol, 2006. 419: p. 426-38.

211. Peister, A., et al., *Osteogenic differentiation of amniotic fluid stem cells.* Biomed Mater Eng, 2008. 18(4-5): p. 241-6.

212. Peister, A., et al., *Amniotic Fluid Stem Cells Produce Robust Mineral Deposits on Biodegradable Scaffolds.* Tissue Eng Part A, 2009.

213. Li, W.J., et al., *Multilineage differentiation of human mesenchymal stem cells in a three-dimensional nanofibrous scaffold.* Biomaterials, 2005. 26(25): p. 5158-66.

214. Yoshimoto, H., et al., *A biodegradable nanofiber scaffold by electrospinning and its potential for bone tissue engineering.* Biomaterials, 2003. 24(12): p. 2077-82.

215. Klinkhammer, K., et al., *Deposition of electrospun fibers on reactive substrates for in vitro investigations.* Tissue Eng Part C Methods, 2009. 15(1): p. 77-85.

216. Sekiya, I., et al., *Expansion of human adult stem cells from bone marrow stroma: conditions that maximize the yields of early progenitors and evaluate their quality.* Stem Cells, 2002. 20(6): p. 530-41.

217. Martin, J.Y., et al., *Proliferation, differentiation, and protein synthesis of human osteoblast-like cells (MG63) cultured on previously used titanium surfaces.* Clin Oral Implants Res, 1996. 7(1): p. 27-37.

218. Leary, N.O., A. Pembroke, and P.F. Duggan, *Single stable reagent (Arsenazo III) for optically robust measurement of calcium in serum and plasma.* Clin Chem, 1992. 38(6): p. 904-8.

219. Uchimura, E., et al., *In-situ visualization and quantification of mineralization of cultured osteogenetic cells.* Calcif Tissue Int, 2003. 73(6): p. 575-83.

220. Hale, L.V., Y.F. Ma, and R.F. Santerre, *Semi-quantitative fluorescence analysis of calcein binding as a measurement of in vitro mineralization.* Calcif Tissue Int, 2000. 67(1): p. 80-4.

221. Kutner, M.H., et al., *Applied linear statistical models*. 5th ed. 2005, New York, NY: McGraw-Hill.

222. Box, G.E.P. and D.R. Cox, *An analysis of transformations.* J Royal Statistical Society B, 1964. 26: p. 211-243.

223. Wu, C.F.J. and M. Hamada, *Experiments: Planning, analysis, and parameter design optimization*. 1st ed. 2000, New York, NY: Wiley-Interscience.

224. Seibel, M.J., *Molecular markers of bone turnover: biochemical, technical and analytical aspects.* Osteoporos Int, 2000. 11 Suppl 6: p. S18-29.

225. Verma, D., K. Katti, and D. Katti, *Experimental investigation of interfaces in hydroxyapatite/polyacrylic acid/polycaprolactone composites using photoacoustic FTIR spectroscopy.* J Biomed Mater Res A, 2006. 77(1): p. 59-66.

226. Venugopal, J., et al., *Electrospun-modified nanofibrous scaffolds for the mineralization of osteoblast cells.* J Biomed Mater Res A, 2008. 85(2): p. 408-17.

227. Shin, M., H. Yoshimoto, and J.P. Vacanti, *In vivo bone tissue engineering using mesenchymal stem cells on a novel electrospun nanofibrous scaffold.* Tissue Eng, 2004. 10(1-2): p. 33-41.

228. Gersbach, C.A., et al., *Inducible regulation of Runx2-stimulated osteogenesis.* Gene Ther, 2006. 13(11): p. 873-82.

229. Abdallah, B.M. and M. Kassem, *The use of mesenchymal (skeletal) stem cells for treatment of degenerative diseases: current status and future perspectives.* J Cell Physiol, 2009. 218(1): p. 9-12.

230. Quarto, R., et al., *Repair of large bone defects with the use of autologous bone marrow stromal cells.* N Engl J Med, 2001. 344(5): p. 385-6.

231. Shi, S., et al., *Bone formation by human postnatal bone marrow stromal stem cells is enhanced by telomerase expression.* Nat Biotechnol, 2002. 20(6): p. 587-91.

232. Lian, J.B. and G.S. Stein, *Development of the osteoblast phenotype: molecular mechanisms mediating osteoblast growth and differentiation.* Iowa Orthop J, 1995. 15: p. 118-40.

233. Aubin, J.E., *Regulation of osteoblast formation and function.* Rev Endocr Metab Disord, 2001. 2(1): p. 81-94.

234. Hinnebusch, B.F., et al., *Enterocyte differentiation marker intestinal alkaline phosphatase is a target gene of the gut-enriched Kruppel-like factor.* Am J Physiol Gastrointest Liver Physiol, 2004. 286(1): p. G23-30.

235. Matsumoto, H., et al., *Biosynthesis of alkaline phosphatase during differentiation of the human colon cancer cell line Caco-2.* Gastroenterology, 1990. 98(5 Pt 1): p. 1199-207.

236. Woo, K.M., et al., *Nano-fibrous scaffolding promotes osteoblast differentiation and biomineralization.* Biomaterials, 2007. 28(2): p. 335-43.

237. Smith, L.A., et al., *Enhancing osteogenic differentiation of mouse embryonic stem cells by nanofibers.* Tissue Eng Part A, 2009. 15(7): p. 1855-64.

238. Peppas, N.A. and R. Langer, *New challenges in biomaterials.* Science, 1994. 263(5154): p. 1715-20.

239. Griffin, T.J., W.S. Cheung, and H. Hirayama, *Hard and soft tissue augmentation in implant therapy using acellular dermal matrix.* Int J Periodontics Restorative Dent, 2004. 24(4): p. 352-61.

240. Badylak, S.F., *The extracellular matrix as a scaffold for tissue reconstruction.* Semin Cell Dev Biol, 2002. 13(5): p. 377-83.

241. Swiontkowski, M.F., et al., *Recombinant human bone morphogenetic protein-2 in open tibial fractures. A subgroup analysis of data combined from two prospective randomized studies.* J Bone Joint Surg Am, 2006. 88(6): p. 1258-65.

242. Athanasiou, K.A., G.G. Niederauer, and C.M. Agrawal, *Sterilization, toxicity, biocompatibility and clinical applications of polylactic acid/polyglycolic acid copolymers.* Biomaterials, 1996. 17(2): p. 93-102.

243. Li, W.J., et al., *Fabrication and characterization of six electrospun poly(alpha-hydroxy ester)-based fibrous scaffolds for tissue engineering applications.* Acta Biomater, 2006. 2(4): p. 377-85.

244. Bellamkonda, R., J.P. Ranieri, and P. Aebischer, *Laminin oligopeptide derivatized agarose gels allow three-dimensional neurite extension in vitro.* J Neurosci Res, 1995. 41(4): p. 501-9.

245. Pierschbacher, M.D. and E. Ruoslahti, *Cell attachment activity of fibronectin can be duplicated by small synthetic fragments of the molecule.* Nature, 1984. 309(5963): p. 30-3.

246. Kao, W.J., et al., *Fibronectin modulates macrophage adhesion and FBGC formation: the role of RGD, PHSRN, and PRRARV domains.* J Biomed Mater Res, 2001. 55(1): p. 79-88.

247. Petrie, T.A., et al., *Integrin specificity and enhanced cellular activities associated with surfaces presenting a recombinant fibronectin fragment compared to RGD supports.* Biomaterials, 2006. 27(31): p. 5459-70.

248. Massia, S.P., S.S. Rao, and J.A. Hubbell, *Covalently immobilized laminin peptide Tyr-Ile-Gly-Ser-Arg (YIGSR) supports cell spreading and co-localization of the 67-kilodalton laminin receptor with alpha-actinin and vinculin.* J Biol Chem, 1993. 268(11): p. 8053-9.

249. Knight, C.G., et al., *The collagen-binding A-domains of integrins alpha(1)beta(1) and alpha(2)beta(1) recognize the same specific amino acid sequence, GFOGER, in native (triple-helical) collagens.* J Biol Chem, 2000. 275(1): p. 35-40.

250. Knight, C.G., et al., *Identification in collagen type I of an integrin alpha2 beta1-binding site containing an essential GER sequence.* J Biol Chem, 1998. 273(50): p. 33287-94.

251. Reyes, C.D. and A.J. Garcia, *Engineering integrin-specific surfaces with a triple-helical collagen-mimetic peptide.* J Biomed Mater Res A, 2003. 65(4): p. 511-23.

252. Carlsson, L., et al., *Removal torques for polished and rough titanium implants.* Int J Oral Maxillofac Implants, 1988. 3(1): p. 21-4.

253. Martin, J.Y., et al., *Effect of titanium surface roughness on proliferation, differentiation, and protein synthesis of human osteoblast-like cells (MG63).* J Biomed Mater Res, 1995. 29(3): p. 389-401.

254. Buser, D., et al., *Influence of surface characteristics on bone integration of titanium implants. A histomorphometric study in miniature pigs.* J Biomed Mater Res, 1991. 25(7): p. 889-902.

255. Lincks, J., et al., *Response of MG63 osteoblast-like cells to titanium and titanium alloy is dependent on surface roughness and composition.* Biomaterials, 1998. 19(23): p. 2219-32.

256. Zhong, S., et al., *An aligned nanofibrous collagen scaffold by electrospinning and its effects on in vitro fibroblast culture.* J Biomed Mater Res A, 2006. 79(3): p. 456-63.

257. Yang, F., et al., *Electrospinning of nano/micro scale poly(L-lactic acid) aligned fibers and their potential in neural tissue engineering.* Biomaterials, 2005. 26(15): p. 2603-10.

258. Kim, Y.T., et al., *The role of aligned polymer fiber-based constructs in the bridging of long peripheral nerve gaps.* Biomaterials, 2008. 29(21): p. 3117-27.

259. Corey, J.M., et al., *Aligned electrospun nanofibers specify the direction of dorsal root ganglia neurite growth.* J Biomed Mater Res A, 2007. 83(3): p. 636-45.

260. Tomasz, M., *Mitomycin C: small, fast and deadly (but very selective).* Chem Biol, 1995. 2(9): p. 575-9.

261. Kark, L.R., J.M. Karp, and J.E. Davies, *Platelet releasate increases the proliferation and migration of bone marrow-derived cells cultured under osteogenic conditions.* Clin Oral Implants Res, 2006. 17(3): p. 321-7.

262. Reyes, C.D. and A.J. Garcia, *A centrifugation cell adhesion assay for high-throughput screening of biomaterial surfaces.* J Biomed Mater Res A, 2003. 67(1): p. 328-33.

263. Morton, L.F., et al., *Conformation-dependent platelet adhesion to collagen involving integrin alpha 2 beta 1-mediated and other mechanisms: multiple alpha 2 beta 1-recognition sites in collagen type I.* Biochem J, 1994. 299 (Pt 3): p. 791-7.

264. Shang, Y.C., et al., *Wnt3a signaling promotes proliferation, myogenic differentiation, and migration of rat bone marrow mesenchymal stem cells.* Acta Pharmacol Sin, 2007. 28(11): p. 1761-74.

265. Patel, S., et al., *Bioactive nanofibers: synergistic effects of nanotopography and chemical signaling on cell guidance.* Nano Lett, 2007. 7(7): p. 2122-8.

266. Bashur, C.A., L.A. Dahlgren, and A.S. Goldstein, *Effect of fiber diameter and orientation on fibroblast morphology and proliferation on electrospun poly(D,L-lactic-co-glycolic acid) meshes.* Biomaterials, 2006. 27(33): p. 5681-8.

267. McCarroll, J.A., et al., *Pancreatic stellate cell migration: role of the phosphatidylinositol 3-kinase(PI3-kinase) pathway.* Biochem Pharmacol, 2004. 67(6): p. 1215-25.

268. Heino, J., *The collagen receptor integrins have distinct ligand recognition and signaling functions.* Matrix Biol, 2000. 19(4): p. 319-23.

269. Kim, H.K., et al., *Antimigratory effect of TK1-2 is mediated in part by interfering with integrin alpha2beta1.* Mol Cancer Ther, 2008. 7(7): p. 2133-41.

270. Ferdous, Z., et al., *A role for decorin in controlling proliferation, adhesion, and migration of murine embryonic fibroblasts.* J Biomed Mater Res A, 2009.

271. Michael, K.E., et al., *Focal adhesion kinase modulates cell adhesion strengthening via integrin activation.* Mol Biol Cell, 2009. 20(9): p. 2508-19.

272. Clark, E.A. and J.S. Brugge, *Integrins and signal transduction pathways: the road taken.* Science, 1995. 268(5208): p. 233-9.

273. Senger, D.R., et al., *The alpha(1)beta(1) and alpha(2)beta(1) integrins provide critical support for vascular endothelial growth factor signaling, endothelial cell migration, and tumor angiogenesis.* Am J Pathol, 2002. 160(1): p. 195-204.

274. Takeuchi, Y., et al., *Differentiation and transforming growth factor-beta receptor down-regulation by collagen-alpha2beta1 integrin interaction is mediated by focal adhesion kinase and its downstream signals in murine osteoblastic cells.* J Biol Chem, 1997. 272(46): p. 29309-16.

275. Byers, B.A., et al., *Cell-type-dependent up-regulation of in vitro mineralization after overexpression of the osteoblast-specific transcription factor Runx2/Cbfal.* J Bone Miner Res, 2002. 17(11): p. 1931-44.

276. Xiao, G., et al., *MAPK pathways activate and phosphorylate the osteoblast-specific transcription factor, Cbfa1.* J Biol Chem, 2000. 275(6): p. 4453-9.

277. Wojtowicz, A.M., et al. *Collagen-mimetic peptide coating of biomaterial scaffolds for bone defect repair*. in *Annual Meeting of the Society for Biomaterials*. 2008. Atlanta, GA.

278. Rai, B., et al., *Combination of platelet-rich plasma with polycaprolactone-tricalcium phosphate scaffolds for segmental bone defect repair.* J Biomed Mater Res A, 2007.

279. Kim, H.W., H.H. Lee, and J.C. Knowles, *Electrospinning biomedical nanocomposite fibers of hydroxyapatite/poly(lactic acid) for bone regeneration.* J Biomed Mater Res A, 2006. 79(3): p. 643-9.

280. Kolambkar, Y.M., et al. *Osteoprogenitor cell proliferation and differentiation on electrospun nanofibers*. in *TERMIS NA Annual Conference and Exposition*. 2007. Toronto, Ontario.

281. Rowley, J.A., G. Madlambayan, and D.J. Mooney, *Alginate hydrogels as synthetic extracellular matrix materials.* Biomaterials, 1999. 20(1): p. 45-53.

282. Sanderson, C. and K. Bachus, *STAINING TECHNIQUE TO DIFFERENTIATE MINERALIZED AND DEMINERALIZED BONE IN GROUND SECTION.* Journal of histotechnology, 1997. 20(2): p. 119-122.

283. Duvall, C.L., et al., *Quantitative microcomputed tomography analysis of collateral vessel development after ischemic injury.* Am J Physiol Heart Circ Physiol, 2004. 287(1): p. H302-10.

284. Meinig, R.P., et al., *Regeneration of diaphyseal bone defects using resorbable poly(L/DL-lactide) and poly(D-lactide) membranes in the Yucatan pig model.* J Orthop Trauma, 1997. 11(8): p. 551-8.

285. Peters, M.C., et al., *Release from alginate enhances the biological activity of vascular endothelial growth factor.* J Biomater Sci Polym Ed, 1998. 9(12): p. 1267-78.

286. Silva, E.A. and D.J. Mooney, *Spatiotemporal control of vascular endothelial growth factor delivery from injectable hydrogels enhances angiogenesis.* J Thromb Haemost, 2007. 5(3): p. 590-8.

287. Duvall, C.L., et al., *Impaired angiogenesis, early callus formation, and late stage remodeling in fracture healing of osteopontin-deficient mice.* J Bone Miner Res, 2007. 22(2): p. 286-97.

288. Guldberg, R.E., et al., *Analyzing bone, blood vessels, and biomaterials with microcomputed tomography.* IEEE Eng Med Biol Mag, 2003. 22(5): p. 77-83.

289. Johnson, M.R., et al., *Sustained release of BMP-2 in a lipid-based microtube vehicle.* Acta Biomater, 2009. 5(1): p. 23-8.

290. Kokubo, S., et al., *Bone regeneration by recombinant human bone morphogenetic protein-2 and a novel biodegradable carrier in a rabbit ulnar defect model.* Biomaterials, 2003. 24(9): p. 1643-51.

291. Prabaharan, M. and J.F. Mano, *Chitosan-based particles as controlled drug delivery systems.* Drug Deliv, 2005. 12(1): p. 41-57.

292. Saito, N., et al., *Biodegradable poly-D,L-lactic acid-polyethylene glycol block copolymers as a BMP delivery system for inducing bone.* J Bone Joint Surg Am, 2001. 83-A Suppl 1(Pt 2): p. S92-8.

293. Yamamoto, M., Y. Takahashi, and Y. Tabata, *Enhanced bone regeneration at a segmental bone defect by controlled release of bone morphogenetic protein-2 from a biodegradable hydrogel.* Tissue Eng, 2006. 12(5): p. 1305-11.

294. Lieberman, J.R., et al., *The effect of regional gene therapy with bone morphogenetic protein-2-producing bone-marrow cells on the repair of segmental femoral defects in rats.* J Bone Joint Surg Am, 1999. 81(7): p. 905-17.

295. Yasko, A.W., et al., *The healing of segmental bone defects, induced by recombinant human bone morphogenetic protein (rhBMP-2). A radiographic, histological, and biomechanical study in rats.* J Bone Joint Surg Am, 1992. 74(5): p. 659-70.

296. Wozney, J.M. and V. Rosen, *Bone morphogenetic protein and bone morphogenetic protein gene family in bone formation and repair.* Clin Orthop Relat Res, 1998(346): p. 26-37.

297. Winnier, G., et al., *Bone morphogenetic protein-4 is required for mesoderm formation and patterning in the mouse.* Genes Dev, 1995. 9(17): p. 2105-16.

298. Lutolf, M.P., et al., *Repair of bone defects using synthetic mimetics of collagenous extracellular matrices.* Nat Biotechnol, 2003. 21(5): p. 513-8.

299. Odgaard, A. and H.J. Gundersen, *Quantification of connectivity in cancellous bone, with special emphasis on 3-D reconstructions.* Bone, 1993. 14(2): p. 173-82.

300. Lindsey, R.W., et al., *The efficacy of cylindrical titanium mesh cage for the reconstruction of a critical-size canine segmental femoral diaphyseal defect.* J Orthop Res, 2006. 24(7): p. 1438-53.

301. Geiger, M., R.H. Li, and W. Friess, *Collagen sponges for bone regeneration with rhBMP-2.* Adv Drug Deliv Rev, 2003. 55(12): p. 1613-29.

302. Hollinger, J.O., et al., *Recombinant human bone morphogenetic protein-2 and collagen for bone regeneration.* J Biomed Mater Res, 1998. 43(4): p. 356-64.

303. Zabka, A.G., et al., *Histomorphometric description of allograft bone remodeling and union in a canine segmental femoral defect model: a comparison of rhBMP-2, cancellous bone graft, and absorbable collagen sponge.* J Orthop Res, 2001. 19(2): p. 318-27.

304. Pluhar, G.E., et al., *The effect of recombinant human bone morphogenetic protein-2 on femoral reconstruction with an intercalary allograft in a dog model.* J Orthop Res, 2001. 19(2): p. 308-17.

305. Cuomo, A.V., et al., *Mesenchymal stem cell concentration and bone repair: potential pitfalls from bench to bedside.* J Bone Joint Surg Am, 2009. 91(5): p. 1073-83.

306. Chen, X., et al., *Union of a chronically infected internally stabilized segmental defect in the rat femur after debridement and application of rhBMP-2 and systemic antibiotic.* J Orthop Trauma, 2007. 21(10): p. 693-700.

307. Kleinman, H.K. and G.R. Martin, *Matrigel: basement membrane matrix with biological activity.* Semin Cancer Biol, 2005. 15(5): p. 378-86.

308. Boerckel, J.D., et al., *In vivo model for evaluating the effects of mechanical stimulation on tissue-engineered bone repair.* J Biomech Eng, 2009. 131(8): p. 084502.

309. Betz, O.B., et al., *Delayed administration of adenoviral BMP-2 vector improves the formation of bone in osseous defects.* Gene Ther, 2007. 14(13): p. 1039-44.

VITA

YASH M. KOLAMBKAR

Yash Kolambkar was born on July 10th 1979 to parents Sujata and Manohar Kolambkar, three years after the birth of their first son, Navin. He was born and brought up in the historic and dusty town of Aurangabad in the state of Maharashtra in India. He completed all of his primary and secondary education in Holy Cross English School, where he met his future wife Ayona in 8th grade. He excelled in both academics and extracurricular activities, and secured a place in the district-level merit list in the 10th grade board exams. During his final year in school, Yash was selected to be the Chief Sergeant Major of the 51st Maharashtra Battalion of the National Cadet Corps, a position he took a little too seriously, as he is still constantly reminded by his friends. He also captained his high school in cricket and excelled in cross-country running. He then attended Devgiri College for his higher secondary education, lost a little bit of focus, but did reasonably well in the end. In 1997, Yash moved to the bustling city of Pune to pursue a Bachelor's Degree in Mechanical Engineering at the Vishwakarma Institute of Technology (VIT). It was during this time that he enjoyed the proudest moment of his unfulfilled sports career – winning the Intra-Engineering Football Championship with VIT. Yash graduated in 2001 with a First Class with Distinction, and received a job offer from the software company, Wipro. This, however, coincided with the dotcom bust period, and he was promptly told that there was no work to be done. This turned out to a boon, as he decided to attend graduate school at the University of Cincinnati, Ohio (UC) in 2002. Yash received a M.S. in Mechanical Engineering in 2004, but for some reason felt that he had not received enough education. He had, however, realized that he did not want to work on topics that were being researched for the past 100 years. While at UC, he was exposed to the emerging field of Tissue Engineering, and decided to switch fields and pursue a Ph.D. in Biomedical Engineering at Georgia Tech. During his five 5 years in Atlanta, Yash learnt to pipette, recognize happy cells, and even do animal surgery. He ran the Peachtree Road Race twice, and assembled a talented intramural soccer team, which twice reached the finals of the graduate league. In 2005, Yash got married to his childhood sweetheart, Ayona, and they had a beautiful baby daughter, Avika, in 2009.